Shane Murphy

A dynamic and kinematic investigation of early rupture waves and their seismic radiation

Dottorato di Ricerca in Rischio Seismico

XX Ciclo

30 November 2007

Tutore: Dr. Stefan Nielsen

Coordinatore: Prof. Paolo Gasparini

Contents

Notation

Symbol	Meaning
A	average attenuation
α	primary wave velocity
$A_{i,j}$	displacement matrix
β	shear wave velocity
c_{ijkl}	4^{th} order tensor of constants relating stress to strain
C, α_a, α_b	geometrical constant that define fault size
C_w	fault width wavenumber
D_i	velocity derivative squared
D	amplitude of particle motion
D_c	critical slip distance
D_t	discrete time derivative
D_x , D_y, D_z	discrete spatial dervatives
$\dot{\mathbf{D}}$	discrete sliprate
δ_{ij}	Kronecker delta
δ	fault dip
$\Delta\sigma_d$	dynamic stress drop
$\Delta\sigma_s$	static stress drop
Δ	epicentral distance to station
Δ_r	regional correction for magnitude estimation
Δ_s	site correction for magnitude estimation
Δu	slip on fault plane
$\Delta\dot{u}$	slip rate
$\overline{\Delta u}$	average slip over whole fault plane
$\overline{\Delta\sigma}$	average stress drop
$\overline{\Delta\dot{u}}$	average slip rate

Continued on next page

Symbol	Meaning
$\Delta\sigma_L(k)$	stress drop spectra for a fault of length L
Δt	finite difference time step
$\Delta x, \Delta y, \Delta z,$	finite difference spatial steps
EEW	Earthquake Early Warning
e_{ij}	strain tensor
f	correction factor for magnitude estimation
$\mathbf{f}$	applied body force vector
F	fault traction
G_e	elastostatic energy
$H()$	heaviside function
h	finite difference step size
I_{mm}	Modified Mercalli Scale
$I(t)$	isochrone at time t
Λ	length scale function of actively slipping area
λ	Lame Constant
L_c	critical crack length
L	fault length
μ	shear modulus
μ_o, A, B	rate friction law parameters
μ_s	static coefficient of friction
μ_d	dynamic coeffiecient of friction
M	magnitude
M_{sat}	magnitude at which saturation is observed
M_s	surface wave magnitude
M_L	local magnitude
m_b	body wave magnitude
M_w	moment magnitude

Continued on next page

Symbol	Meaning
M_o	seismic moment
$\mathbf{n}$	normal vector
ω_{ij}	rigid body rotation tensor
ω	frequency
PGD	Peak Ground Displacement
PGV	Peak Ground Velocity
PGA	Peak Ground Acceleration
r	source - receiver distance
$\mathbf{R^c}$	radiation coefficent
$\overline{R_L}$	average rupture length
σ_y	yield stress of media
σ_{ext}	pre-stress surrounding L_c
$\mathbf{\Sigma}$	discrete stress tensor
σ_{ij}	2^{nd} order stress tensor
S	arbitrary surface
$S(t)$	fault surface at time t
S_ξ	fault surface
τ_p	predominant frequency
τ_p^{max}	largest predominant frequency
$\mathbf{T}$	Traction vector
T_D	rise time
T_R	apparent rupture duration
T	period of the signal being examined
T_{obs}	observational time window
θ	state variable
τ	time on fault plane
$u(\mathbf{x}, t)$	displacment at postion $\mathbf{x} = (x, y, z)$ and time t

Continued on next page

Symbol	Meaning
$u_{i,j}$	partial derivative of u_i in relation to the spatial component x_j
$\dot{u}$	particle velocity (i.e. the sliprate)
$\ddot{u}$	particle acceleration
u^+	displacement just above the fault plane
u^-	displacement just below the fault plane
v_h	healing velocity
v_i	i^{th} component of slip rate
v_r	rupture velocity
V_c	characteristic rate weakening parameter
V	arbitrary volume
$\mathbf{V}$	discrete particle velocity vector
W	fault width
X_i	smoothened ground velocity
$\mathbf{x_R}$	receiver postion
$\mathbf{x_H}$	hypocetre postion
$\mathbf{x_S}$	source postion
ξ	position on fault plane

Chapter 1

Introduction

Foreword

The present thesis, though theoretical in essence, was motivated by a series of seismological observations which offers new methods for fast earthquake magnitude estimation. Such techniques are now being incorporated into Early Warning Systems. These systems are pertinent to the reduction of seismic hazard by providing authorities with the ability to respond rapidly, and quite possibily predictively, to transpiring earthquakes.

When talking of seismic risk mitigation and early warning, topics such as prediciton, prevention and potential hazard come to mind, which differ in several subtle, but important ways. Thus it is benefical to clarify these concepts at the start of this dissertation by means of a few definitions. Upon providing the context of Early Warning in relation to the general field of seismology, it will be all the more straightforward to introduce the motivation and framework behind the present study.

1.1 Seismic Risk and Early Warning Systems

Whilst the prediction of an earthquakes size, location and timing is one of the goals of earthquake seismology, it is, at present too unreliable to be of practical use. The benefits of being able to predict an earthquake were highlighted in the 1975 Haicheng prediction, where, following predefined precursory events (e.g. fore-shocks sequences, geodetic distortion, etc) a prediction of an earthquake was issued (Wang et al. [2006]). The Chinese authorities ordered an evacuation of people from the area thus saving many lives from the subsequent $7.3M_s$ earthquake. The success of such a prediction was put in perspective when a year later an unpredicted $7.5M_s$ Tangshan earthquake occurred in the city of Tangshan (near Beijing) killing 250,000 (Bolt [1993]). Unfortunately the Haicheng earthquake is the only scientifically predicted earthquake. More recent attempts by the USGS to predict an earthquake on the San Andreas Fault with it's 1985 Parkfield Prediction (Kerr [1985]). This prediction failed when the prescribed section of the San Andreas fault, which had ruptured periodically every 12 years previously, failed to do so in 1988 (Kerr [1992a], Kerr [1992b]).

Whilst earthquake prediction currently remains elusive, there are two other forms of risk reduction being used: probabilistic seismic hazard assessment and early warning of impending earthquakes. Reiter [1991] describes *seismic hazard analysis* as the assessment of the potential for for dangerous, earthquake-related natural phenomena (for e.g. ground shaking, fault rupture or soil liquefaction). It is this concept that is used in producing probabilistic seismic hazard maps. By calculating the probability of different sized earthquake occuring at diffferent locations as well as accounting for wave attenuation, probabilistic seismic hazard maps can be created for regions (for examples see Slejko et al. [1998], Giardini et al. [1999]). Such maps can then be used by the local authorities/ governments in long term re-

duction seismic hazard (for example, updating emergency plans and building codes).

Early warning on the other hand is based on the rapid interpretation of initial ground motion from a rupturing earthquake. For example, several authors (Ellsworth and Beroza [1995], Beroza and Ellsworth [1996], Iio [1995]) have advocated a link between the initial part of the radiated p-wave and the impending earthquakes' final size, implying a deterministic underlying nature to earthquakes.

Iio [1995] postulated that, based on the initial curvature of the p-phase, the longer and slower the initial phases are the larger the resulting earthquake shall be. This has been countered by Mori and Kanamori [1996] who believe the initial p-phase curvature they observe in there investigation of the Ridgecrest earthquake sequence is due to elastic attenuation. Additionally, Lewis and Ben-Zion [2007] examination of the earthquake clusters on the Anatolian Fault could not find a meaningful scaling trend between Iio's signal and the preceding earthquakes magnitude.

Ellsworth and Beroza [1995] and Beroza and Ellsworth [1996] on the other hand postulated that small precursory phases to the p-wave could be due to an aseismic pre-slip phase in an earthquakes nucleation. They are argue that this pre-slip area (denoted by small amplitudes that precede the main P arrival) predetermines an earthquakes final size. However, such amplitudes are influenced by spurious FIR effects (anti-alias filtering that automatically precedes signal digitisation, during the acquisition process of a seismic station). After thorough signal processing it was shown that FIR artifacts had similar moment scaling properties to that of pre-nucleation phases (Scherbaum and Bouin [1997]). Other studies of the pre-slip phases have produced contradictory results to that of the pre-slip phase with Kilb and Gomberg [1999] noting that initial phases do not scale with earthquake size and Lewis and Ben-Zion [2007] finding such signals present in less than 20% seismograms

after careful removal of FIR effects.

Indeed, Sato and Kanamori [1999] showed with the use of a crack model based on the Griffith's fracture criterion that variations in fracture toughness near the fault tip produce large variations in the waveforms produced during the start of rupture, questioning the possibility that initial waveforms can scale with final earthquake size.

Whilst earthquake prediction in the long term or very short term is not yet possible, with the advances in technology a warning about an earthquake as it happens is now feasible. Such practice is referred to as "early warning" (i.e. EW). A system based on EW uses the first few seconds of recorded ground motion (which do not cause structural damage) at one or a number of seismic stations near a fault to predict/determine the size of the impending slower, more disruptive seismic waves for the same location or region in general. This warning provides authorities with a reaction time window of a few hours to a to a few seconds (depending location of the target site). Thus the seismic risk for a given area can be greatly reduced. Indeed Bill Clinton in an address at the Third International Conference on Early Warning stated "Early warning systems are the key to effective risk reduction. They do save lives and livelihoods".

1.2 Earthquake Early Warning Systems

The creation of a system that could generate a warning due to the imminent arrival of destructive surface waves from a distant earthquake was first proposed by J. D. Cooper in 1868 (Nakamura and Saita [2007]). His article in the San Francisco Daily Evening Bulletin suggested deployment of a large array of electrical powerlines radiating out from San Francisco which would sound a warning bell in the city in the event of an earthquake occurring in the outlier areas of the systems.

The first functioning system however, was not deployed until 1982, (a precusor to UrEDAS - Urgent Earthquake Decticion and Alarm System) in Japan for the rail system there (Nakamura and Saita [2007]). Since then, early warning systems have been or are in the process of being deployed in many different countries (e.g. Mexico, Japan, Taiwan – Normile [2004]). These early systems offer a rudimentary warning when a particular ground motion is obtained at a seismic station for a specific structure nearby (e.g. nuclear power plant Wieland et al. [2000] or high speed rail network Nakamura and Saita [2007]). Such systems are referred to as "on-site" EEW (early earthquake warning) systems as their warnings are limited to only to the location of the seismic station.

With time, more complex EEW systems have evolved whereby warning of regions can now be issued (e.g. Ealarm, Wurman et al. [2007]; Virtual Seismologist, Cua and Heaton [2007]; ISNet, Weber et al. [2007]; etc). These regional systems use seismic arrays positioned in seismogenic areas to locate and estimate an earthquakes size before issuing an earthquake warning. These systems also generate maps of interpolated and extrapolated peak ground motion for the general region (i.e. a ShakeMap) minutes after an earthquake has occurred. Such maps can then be used by emergency services in deciding on what areas of an urban requires most help.

Some EEW systems employ a hybrid approach to warning whereby areas near an earthquake receive "on-site" warnings from seismic stations in the area, whilst seismic network provides a more accurate warning to outlying urban areas (Wu and Kanamori [2005]).

Such rapid collection and analysis of seismic data which is of use for emergency services was termed *real time* seismology by Kanamori [2005]. By sub-dividing this definition further into *near-real time* and *real time* we hope to clarify analysis preformed on seismic data collected when, in the first instance the event has stopped and the latter the earthquake is ongoing.

Therefore *near-real time* analysis takes longer but is more accurate whilst *real time* is quicker and so provides more time to respond to an impending event but is less accurate. Both sets of results however are beneficial to emergency response units in the event of an earthquake.

In terms of generating a warning for the risk caused by an occurring/just finished earthquake, the *modus operandi* of a EEW system can be subdivided into three parts: hypocentre location, size (i.e. magnitude) estimation, and finally ShakeMap generation.

With a seismic station being triggered by the p-wave from an ensuing earthquake, the earthquakes hypocentre is first determined. This is calculated based on the different p- wave arrival times for different stations in the seismic network. At the onset of an earthquake, when only one or two stations have detected the initial p.wave, the non-detection of a signal at at nearby stations is used to further constrain the possible hypocentre location (Rydelek and Pujol [2004], Horiuchi et al. [2005] and Satriano et al. [2007]). Alternatively a p-wave's amplitude can also be used as is the case with the Virtual Seismologist (Cua and Heaton [2007]). In both cases, as the location of the hypocentre is determined in real-time, it is constantly being refined with increasing time as more stations record p-wave arrivals.

After timing the arrival of the p-wave, the size of the earthquake is estimated. The standard magnitude scale is used for this, a parameter discussed in more detail in section 1.3. For a real-time magnitude estimated either the predominant frequency (Nakamura and Saita [2007], Allen and Kanamori [2003]) or the peak ground displacement (Wu and Zhao [2006], Zollo et al. [2006]) is calculated for the first few seconds of the p- and/or s-wave signal. In the case of regional EEW systems the average value is taken which in turn scales with the magnitude. It is this scaling relationship which shall be the topic of discussion of this report. For "on-site" EEW systems the individual station readings are used as predictions for forth coming large

amplitude surface waves (Nakamura and Saita [2007], Wu and Kanamori [2005]). Some EEW systems employ a hybrid magnitude estimation where both the peak ground displacement and the predominant frequency are used together (Wurman et al. [2007] and Tsang et al. [2007]).

The amount of damage an area suffers from an earthquake is quantified using the modified Mercalli Scale (I_{mm}). Wald et al. [1999b] derived a regressional relationship between the modified Mercalli Sale and ground motion (i.e. peak ground velocity –PGV, and peak ground acceleration –PGA). Therefore shaking recorded at stations in seismic networks can be used to create maps defining the spatial distribution of damage from an earthquake. Such maps are called ShakeMaps and involve interpolating and extrapolating ground motion intensity between seismic stations whilst accounting for frequency, geological formations and site effects in the process (Wald et al. [1999a] and Wald et al. [1999b]). EEW systems can generate ShakeMaps in 1 minute (liang Teng et al. [1997]), 3 - 5 minutes (Wald et al. [1999a]) and 30 minutes (Dreger and Kaverina [2000]) after an earthquake has occurred, thus producing maps highlighting areas with a high potential for damage rapidly.

In summary, EEW systems rely on the fastest possible estimates of the earthquake size and location through some automated interpretation of motion at receivers in a network. Ultimately, fast earthquake size estimation relies on state of the art seismological tools, based on the kinematics of wave propagation and source dynamics theory. In particular, since a few seconds may be of vital importance, what is the minimum signal duration needed in order to provide a reliable magnitude estimate? Which parameter is most relevant in the signal?

1.3 Magnitude Estimation

A vital component of EEW systems is the determination of the size of the impending earthquake; as it is this parameter which decides whether a warning is to be issued or not. Whilst the rapid estimation of an earthquakes size is sought by EEW systems this must be balanced with a reasonable accuracy as false or missed alarms shall affect the reliability of such systems (Grasso et al. [2007] , Iervolino et al. [2007]).

In itself, the topic of accurately quantifying the size of an earthquake has been a central topic of seismological investigation. Given the complexity of earthquake physics the definition of a single parameter that represents the size of an earthquake has been difficult. Richter [1935] was the first to attempt to try and define such a parameter. By taking the amplitude of a short period wave generated by the earthquake (i.e. few Hz to 0.1Hz– based on the Wood Anderson instruments available at the time) and correcting for wave attenuation, Richter called this value the local magnitude (i.e. M_L). The definition of this local magnitude is defined below:

$$M_L = \log(Amp) + f(\Delta) \tag{1.1}$$

where Amp is the amplitude of the wave and $f(\Delta)$ is the empirically derived correction factor accounting for a distance Δ from the source epicentre. However, the fact that the scaling is based on a specific instrument lead to draw backs as the Wood Anderson seismogram had a very limited range in the relatively high frequency. Whilst this is not a problem for stations near the fault, at large distances high frequencies suffer substantial attenuation, thus biasing the estimates.

For this reason magnitude scales based on different wave types was established based on distance from the source-receiver distance (i.e. the body wave magnitude, m_b, for regional distances and the surface-wave magnitude, M_s, for distances greater than 600km Lay and Wallace [1995]). A general

magnitude scaling based on signal amplitude can be defined as (Lay and Wallace [1995]) :

$$M = \log(\frac{Amp}{T}) + f(\Delta, h) + \Delta_s + \Delta_r \tag{1.2}$$

where T is the period of the amplitude (Amp) being measured, $f(\Delta, h)$ which is the correction for depth and epicentral distance, finally Δ_s and Δ_r are the site and source region corrections respectively.

Unfortunately a major problem with using amplitudes of different frequencies to estimate the size of an earthquake is that all such magnitude scales saturate for very large earthquakes. Therefore, for very large earthquakes (i.e. $M_s > 7.5$ Kanamori and Rivera [2004]) the measured amplitude remains constant making it impossible to differentiate between these very large events. This point of saturation is dependent on the frequency of the wave being used for the scaling with the longer period waves saturating at higher magnitudes than shorter ones (for e.g. M_L saturates before M_S – Geller [1976]). The problem of saturation can be traced to the fact that we are measuring an earthquake's size based on its radiation and not on its source features.

Aki [1966] defined the*moment* of an earthquake, M_o as:

$$M_o = \mu \, \overline{\Delta u} \, A \tag{1.3}$$

With μ is the shear modulus, $\overline{\Delta u}$ is the average slip on the fault and A is the area that has slipped. A major advantage of magnitudes based on M_o is that it is directly relates to source features and it does not saturate.

Kanamori [1977] later linked this energy estimate to magnitude thus creating the *moment magnitude* scale:

$$M_w = \frac{2}{3} \log_{10}(M_o) - 6.07 \tag{1.4}$$

where M_o is the moment in Newton meters. As this scale is based on the moment it too will not saturate for very large magnitudes. For this reason,

the moment magnitude has become the default means for scaling an earthquakes size and shall be used as the magnitude scale based on which we shall compare the *real time* estimations.

When an earthquakes radiation is used to establish its size (i.e. magnitude) in EEW systems, there is a trade off between the accuracy of the estimate and the time required to make such a calculation. We shall split magnitude estimation into three categories *post event*, *near-real time* and *real time* which is relative to the time requirement needed to make a magnitude estimate.

Post Event Magnitude Estimation

Post event estimation takes place after the earthquake has occurred, usually taking an hour or more to produce (Ekstrom [1994] and Dziewonski et al. [1981]). Such estimations require the largest amount of time but are also the most accurate over a wide magnitude range. By examining surface waves teleseismically, the earthquakes' magnitude is determined based on the waveforms amplitude and duration (Tsuboi [2000]). This form of estimation is useful for tsunami warnings where mega thrust events can cause large scale damage on coastlines thousands of kilometres away. An example of such an event being the 2004 Great Sumatra-Andaman earthquake with a magnitude range of $9 - 9.3 M_w$ whose tsunami arrived 90 minutes later in Sri Lanka Geist et al. [2007] causing over 35,000 deaths. Therefore, for such large events a more precise magnitude estimate is require over a range where many estimation techniques saturate. However as we are interested in magnitude estimation with target sites at much closer distances this technique is not of interest to us.

Near-Real Time Magnitude Estimation

For near-real time magnitude estimates, the magnitude is calculated based on the whole signal of the body wave signal (i.e. either p- or s-wave) has been recorded at a given station(s). Examples of near-real time magnitudes would be the local magnitude scale M_L, which was described earlier. The body wave magnitude (m_b) is another example, in this case the amplitude of p-waves with a period of 1 second are used (Lay and Wallace [1995]). In both cases, the magnitude scales start to suffer from saturation effects at magnitude greater than 6 (Lay and Wallace [1995]).

Real Time Magnitude Estimation

In real time magnitude estimation only the first few seconds of the body waves (i.e. either the p- or s-waves) particle motion is considered. Using Nakamura's predominant period (Nakamura [1988]) Allen and Kanamori [2003] and Olson and Allen [2005] observed a scaling with the magnitude over a large range with diverse datasets (Allen and Kanamori [2003] used catalogue containing earthquakes that occurred in southern California whilst Olson and Allen [2005] used a more comprehensive dataset with events from southern California, Japan, Taiwan and Alaska) using 4 seconds of recorded ground motion. The predominant frequency which Olson and Allen [2005] refers to as τ_p is calculated using the following formulae:

$$\tau_p^i = \alpha \, 2\pi \sqrt{X_i / D_i} \tag{1.5}$$

with

$$X_i = \alpha X_{i-1} + x_i^2 \tag{1.6}$$

$$D_i = \alpha D_{i-1} + (dx/dt)_i^2 \tag{1.7}$$

where X is the smoothened ground velocity and D velocity derivative squared. α is an exponential dampening factor which has a range between

0 and 1. Wu and Kanamori [2005] used a similar technique whereby the dominant frequency is determined using ground displacement:

$$r = \frac{\int_0^{\tau_o} \dot{u}^2(t)\, dt}{\int_0^{\tau_o} u^2(t)\, dt} \tag{1.8}$$

$$\tau_c = \frac{2\,\pi}{\sqrt{r}} \tag{1.9}$$

In this case τ_o is set to 3 seconds, meaning that the predominant period is calculated in 3 seconds rather than standard 4.

In both cases the maximum predominant period (i.e.τ_p^{max}) is calculated at each seismic station. The average τ_p^{max} is then calculated across all the stations for a given event. It is this average τ_p^{max} that scales linearly with magnitude (an example of which is figure 1.1). In the case of Olson and Allen [2005] this regressional best fit equation is defined as:

$$\log(\tau_p^{max}) = 0.14M - 0.83 \tag{1.10}$$

where M is the magnitude. Wu and Zhao [2006] and Zollo et al. [2006] derived an analogous dependency to that observed using the Nakamura method this time using the peak amplitude displacement (PGD). As with the dominant frequency period, an average value must be taken over data from different seismic stations in order to ascertain a linear relationship with magnitude (see figure 1.2). Using the peak displacement (PGD, the authors argued that the necessary signal time to compute a reliable estimate of magnitude can be reduced to 3 seconds Wu and Zhao [2006] or even 2 seconds Zollo et al. [2006].

Wu and Zhao [2006] and Zollo et al. [2006] fit a best fit line using a similar approach to that of Allen and Kanamori [2003] and Olson and Allen [2005]. However as amplitude is effected by attenuation a correction is made for source to receiver distance. The best fit line is defined as:

$$\log_{10}(PGD) = A + B\,M + \log_{10}(r) \tag{1.11}$$

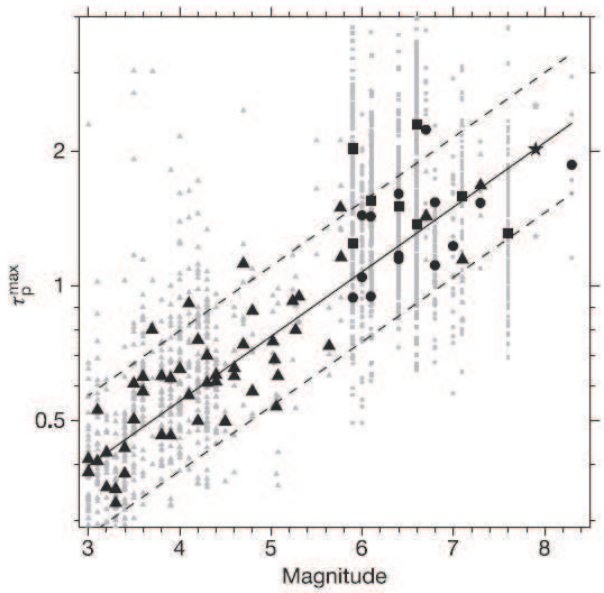

Figure 1.1: The scaling of τ_p^{max} with magnitude. Grey symbols represent the τ_p^{max} value recorded at each station over time period of 4 seconds after the p-arrival. Each symbol represents a different catalogue locations – i.e. circles denote Japan, triangles Southern California, squares Taiwan and stars Alaska. Black symbols represent the average value for each event, with the solid black line defining the linear best-fit. The average absolute standard deviation for the average τ_p^{max} to the best fit line is 0.52 magnitude units, the dashed line represents plus and minus two times this value.Figure taken from Olson and Allen [2005]

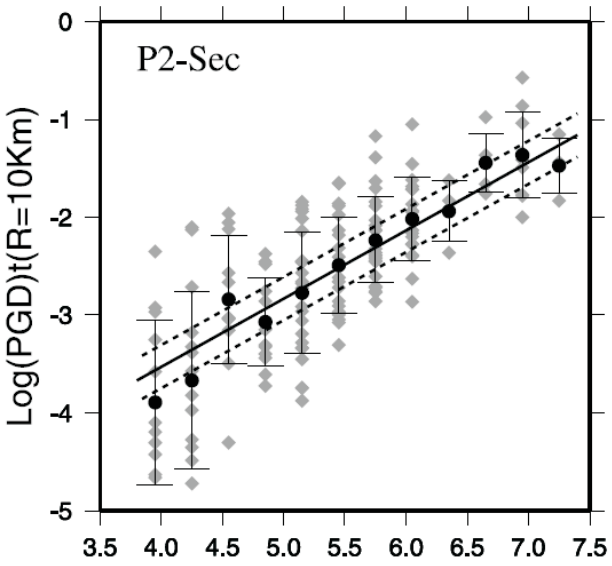

Figure 1.2: Scaling relationship between low band passed filtered peak ground displacement (PGD) and moment magnitude.The grey diamonds represent the PGD recorded 2 seconds after the p-arrival at each individual station. All PGD values have been corrected for a source-receiver distance of 10km. The black circles represent the average PGD for each magnitude bin. The solid black line represents the linear best fit for the average PGD values with the dashed lines representing one unit of weighted standard error This catalogue consists of earthquake data from the European strong motion database. Figure taken from Zollo et al. [2006]

where the variables A, B and C are defined by the fit through the observational data, with r defining the station to source distance.

In the context of EEW systems, it is the linear regression equations (i.e. equations 1.10 and 1.11) which are used in real time magnitude estimation. By inputting the average τ_p^{max} and/or Pd values recorded across a seismic network into either/or equations 1.10 and 1.11 a rapid estimate of the magnitude can be made. The first appraisal can me made 1 second after the first station is triggered and can be updated every second there after (Allen [2007]).

Whilst there is a large scatter between individual readings (see grey dots in figures 1.1 and 1.2) Wurman et al. [2007] applied a hybrid technique using a combination of both τ_p and PGD in Northern California to get magnitude estimates to within a unit range 0.5 of the actual local magnitude solution. However it is questionable whether these scaling relationships are valid for large magnitudes. Wu and Kanamori [2005] noted cautiously that the number of data points for very large magnitudes was sparse in their sparse making the continuation of the τ_c scaling for very large magnitudes inconclusive. Indeed Rydelek and Horiuchi [2006] did not detect a scaling suing the τ_p method for a Japanese catalogues with a magnitude range of 6-8M. On testing the Pd method on Japanese and Taiwanese datasets Rydelek et al. [2007] Wu and Zhao [2006] and Zollo et al. [2007] noted a threshold magnitude after which the PGD saturates. The magnitude at which this saturation occurs at varies between the different authors as well as with the observation time window afforded to stations and the wave type (see tables 1.2 and 1.1). On comparing the Nakamura technique to the Pd method using earthquake clusters generated along the North Anatolian fault Lewis and Ben-Zion [2007] found that both techniques produced meaningful scaling. However the magnitude range of the events present in their catalogue was limited (i.e. 0-4M) therefore they were unable to test Rydelek's hypothesis that real time magnitude

Table 1.1: Scaling parameters taken from literature for τ_p estimates. "Wave" refers to the wave type (i.e. either p- or s-wave), T_{obs} is the amount of seconds after the initial p-/s-wave arrival used in calculating τ_P. "Slope" and "y-intercept" are the parameters of the best fit line for linear scaling and M_{range} is the magnitude range of the observation catalogue. ** denotes a magnitude range for which no scaling was observed. NA denotes when no values were given in the article.

Wave	T_{obs}(s)	Slope	Y-Intercept	M_{range}	Source
P	4	0.16	-1.13	3-5	Allen and Kanamori [2003]
P	4	0.14	0.84	4.5-7.3	Allen and Kanamori [2003]
P	4	0.14	-0.83	3-8.3	Olson and Allen [2005]
P	3	0.221	-1.113	5-7.6	Wu and Kanamori [2005]
P	3	0.324	-1.716	4-7.6	Wu et al. [2006]
P	4	NA	NA	6-8**	Rydelek and Horiuchi [2006]

estimations are not valid for large earthquakes.

1.4 Explanations for Real time magnitude estimation

The aim of this report is to try to determine a possible physical mechanism that could explain this general scaling we see between the first few second of particle motion and an an earthquakes final magnitude.

For small magnitudes, source duration is short and it may be assumed that only 2 seconds of signal contains information on the whole rupture history of the fault. Thus it seems reasonable that scaling can be obtained from

Table 1.2: Scaling parameters taken from literature for τ_p estimates. "Wave" refers to the wave type (i.e. either p- or s-wave), T_{obs} is the amount of seconds after the initial p-/s-wave arrival used in calculating τ_P. "Slope" and "y-intercept" are the parameters of the best fit line for linear scaling and M_{range} is the magnitude range for which a scaling was observable. However, magnitude ranges with * denote catalogues where the authors specify that saturation defines the upper limit of the magnitude scaling range (as opposed to the other cases where M_{range} is defined by the catalogue size). NA highlights when a value was given.r denotes epicentre to station distance.

Wave	T_{obs}(s)	Slope	Y-Intercept	M_{range}	Source
P	3	0.722	-3.81-1.44 log(r)	4-6.5*	Wu et al. [2006]
P	3	0.63	-3.088-1.322 log(r)	4-6.5*	Wu and Zhao [2006]
P	2	0.7	-6.31	4-7.4	Zollo et al. [2006]
S	1	0.68	-5.72	4-7.4	Zollo et al. [2006]
S	2	0.71	-5.77	4-7.4	Zollo et al. [2006]
P	2	1.06	NA	3.5-5.5*	Rydelek et al. [2007]
P	2	0.93	NA	3.5-5.5*	Rydelek et al. [2007]
P	2	0.7489	-6.929	4-6.5*	Zollo et al. [2007]
P	4	0.7024	-6.646	4-7.4	Zollo et al. [2007]
S	2	0.7132	-6.027	4-7.4	Zollo et al. [2007]
S	4	0.807	-6.344	4-7.4	Zollo et al. [2007]

such a reduced initial transient. However, scaling is surprising for bigger events, since a large ($> 7M$) magnitude earthquake source is typically active for at least tens of seconds, and the final size is known only once rupture has stopped. At first sight, this may imply that earthquake size is somehow determined in advance and that such size is detectable in the early phases of rupture. This is reminiscent of Ellsworth and Beroza [1995], Beroza and Ellsworth [1996] and Iio [1995] original idea that features of rupture nucleation are indicative of an earthquakes final size which was discussed in Section 1.1.

Here we do not address the precursory phases but rather the first seconds of the seismogram. This we assume corresponds to the radiation from a fully dynamically propagating rupture in the initial stages, which we refer to as the breakout process, as opposed to the quasi-static nucleation process. Therefore one possible explanation for this large scaling range maybe due to the fact that earthquakes, in the first few seconds of dynamic rupture already have some intrinsic concept on their final size. Another possible hypothesis is that the scaling range is an ingrained feature caused by radiation from a moving source (i.e. a kinematic feature of rupture). Both of these ideas we shall now discuss in more detail.

1.4.1 Deterministic Effect

To some extent, it is debatable whether a deterministic or cascade model best portrays the evolution of an earthquake.

A deterministic earthquake model, assumes that a rupturing fault knows its final size within the first few seconds of rupture initiating. Deterministic fracture evolution could account for the possible scaling that is seen by the early warning techniques and has been proposed as such by Olson and Allen [2005], Nielsen [2007] and Zollo et al. [2006]. Nielsen [2007] noted that energy

flow, G_e, available for fracture propagation in an earthquake can be defined as:

$$G_e = \psi\{\frac{v_r}{\alpha}, \frac{v_r}{\beta}, \frac{v_h}{\beta}\}\pi \frac{\Delta\sigma_d^2}{\mu}\Lambda \tag{1.12}$$

where ψ is a function that is dependent on the the rupture velocity (v_r) and healing velocity (v_h).α is the p-wave velocity and β wave velocity with μ being the shear modulus, $\Delta\sigma_d$ the dynamic stress drop and Λ a length scale function of the actively slipping area on the fault. Nielsen [2007], Olson and Allen [2005] and Zollo et al. [2006] argue that an earthquake with a large G_e influx at the initiation of rupture has a high probability of rupturing further than an earthquake whose G_e is small at initiation. Therefore certain parameters which pertain to the elastostatic energy could have a deterministic influence over final rupture size albeit a probabilistic one. Nielsen [2007] argues that as the dynamic stress drop and rupture length scale (i.e. $\Delta\sigma_d$ and Λ in equation 1.12) indirectly influence far field displacement through the moment rate. There is currently a debate over which elastostatic parameter could be deterministic. Zollo and Lancieri [2007] argued that the slip rate due to a varying stress drop, could be a deterministic parameter citing cases where stress drop variations have been observed (i.e. Kanamori and Rivera [2004],Abercrombie [1995] and Beeler et al. [2003]). Nielsen [2007] on the other hand feel that the longer predominant periods seen for larger earthquakes is due to large actively slipping areas and hence the rise time (i.e. Λ in equation 1.12) could be influential in deciding a rupture's final size. Hillers et al. [2007], by means of numerical modelling observed a scaling between the magnitude and frictional parameters of rupture. This scaling however breaks down for high magnitudes (M_L¿7).

A cascade model, on the other hand assumes that rupture continuity is determined by the local conditions on the fault and therefore that magnitude size is independent of the initial nucleation. For example, geological studies (Wesnousky [2006]) show that earthquakes generally stop at geometrical bar-

riers on the fault, thus arguing in favour of the role of local conditions and not that of the rupture initiation in determining final rupture size. Proponents of this model state the problems seen in the pre-nucleation techniques (see section 1.1) and the complex nature of dynamic rupture. For example Steacy and McCloskey [1998] argued that final earthquake size is heavily dependent on complex interaction of dynamic rupture and pre-stress distribution (a feature which is defined by previous earthquakes).

At present neither hypothesis has been ruled out conclusively. The extent of the problem was highlighted by Lewis and Ben-Zion [2007] who could defined three creditable models for earthquakes rupture – two of which were cascade in nature (i.e. a smooth fault surface with homogeneous properties, and disordered fault with large hetereogeneities) and one in part deterministic (a smooth fault with a heterogeneous frictional properties).

1.4.2 Kinematic Effect

However the relationship between far field particle motion and elastodynamic energy on the fault is not an injective one. Particle motion at seismic stations are also dependant on the observable slipping area on the fault. This means that one second on a seismogram represents a varying amount of the rupture time on the fault depending on station location relative to rupture direction. For example, stations situated in the direction of rupture record a longer source time function in a more concentrated time. Meanwhile stations resident in the opposite direction to rupture propagation would record much less of the source time function in an identical time window.

Having established two possible explanations for the connection between magnitude and the first few seconds of particle motion we shall spend the rest of this paper investigating both possibilities. Firstly we shall look at dynamic modelling to ascertain the claim on whether it is possible that the

fracture evolution is deterministic, and to what extent. Afterwards we shall investigate, by means of isochrone back-projection, whether early magnitude estimation can be explained by casual scaling.

1.5 Summary

In summary, from an observational point of view, there does appear to be some general trend between features seen in the first few seconds after the initial arrival of a P-wave or S-wave and an earthquakes magnitude. However, given the large dispersion in the data and the fact that one of the techniques have been shown not to agree with all data sets proves that the reliability of this technique is variable for larger magnitude ranges. In addition, the scaling for large events poses questions of source mechanics, kinematics and causative relations which require investigation. Up to which threshold does the scaling remain valid under simple kinematic considerations? Are there more deterministic features than traditionally accepted in the earthquake source? If yes, what mechanical model could be compatible with those features? Such are the questions that we address in the present study. Having established two possible explanations for the connection between magnitude and the first few seconds of particle motion we shall spend the rest of this paper investigating both possibilities. Firstly we shall look at dynamic modelling in chapter 2 to ascertain the claim on whether it is possible that the fracture evolution is deterministic. In chapter 3 we shall investigate, by means of isochrone back-projection, whether early magnitude estimation can be explained by casual scaling.

Chapter 2

Dynamic Modelling

2.1 Elastodynamics

Dynamic rupture in an isotropic medium is governed by two sets of equations: the constitutive equation and the equation of motion. These equations control the change in stress and particle motion in a medium and are described in more detail below.

The dynamic rupture model that we shall use is solved by a 3D finite difference method whereby the stress and velocity for a given point are calculated on offset nodes in a staggered grid formation for a planar fault Madariaga [1976].

2.1.1 Strain Tensor

In seismology, a Lagrangian coordinate system is the preferred means of describing a dynamic system. Particle displacement. $\mathbf{u}$, is defined relative to its position at a reference time. Thereby displacement can be defined as:

$$\mathbf{u} = u(\mathbf{x}, t)$$

where $\mathbf{x}$ is the position of the particle at time t.

By examining the distortion of medium due to a displacement we shall now define a strain tensor. By taking two particles in the medium, $\mathbf{x}$ and $\mathbf{x}+\delta\mathbf{x}$ both of which are subjected to a displacement, thus the new position of our particles is now $\mathbf{x}+\mathbf{u}(\mathbf{x})$ and $\mathbf{x}+\delta\mathbf{x}+\mathbf{u}(\mathbf{x}+\delta\mathbf{x})$ respectively. The difference between the two points (i.e. $\delta\mathbf{x}+\delta\mathbf{u}$) can be defined in terms of the original position of the points as:

$$\delta\mathbf{x}+\delta\mathbf{u}=\mathbf{x}+\delta\mathbf{x}+\mathbf{u}(\mathbf{x}+\delta\mathbf{x})-(\mathbf{x}+\mathbf{u}(\mathbf{x})) \tag{2.1}$$

By assuming that $\delta\mathbf{x}$ is small and therefore $|\delta\mathbf{x}|^2$ is insignificant. Equation 2.1 can now be simplified by Taylor expansion such that the relative displacement between the two media elements due to displacement $\mathbf{u}$ is:

$$\delta u_i = u_{i,j}\delta x_j \tag{2.2}$$

where u_i is the i^{th} component of displacement and $u_{i,j}$ is the infinitesimal displacement gradient derivative of i^{th} component of $\mathbf{u}$. However, the relative displacement contains both elements of distortion and rigid body rotation, i.e.:

$$\delta u_i = (e_{ij}+\omega_{ij})\delta x_j \tag{2.3}$$

where e_{ij} is the strain tensor and ω_{ij} is the rigid body rotation one. By adding and subtracting u_{ji} from equation 2.4 we shall separate the strain and the rotation:

$$\delta u_i = \frac{1}{2}\{(u_{ij}+u_{ji})+(u_{ij}-u_{ji})\}\delta x_j \tag{2.4}$$

Therefore the strain tensor is defined as: or, $e_{i,j}$, can be written as:

$$e_{ij} = \frac{1}{2}(u_{i,j}+u_{j,i}) \tag{2.5}$$

2.1.2 Equation of Motion

We can write the equation for the acceleration of a group of particles in volume V with a surface S in terms of the forces acting on those particles in a continuum as follows:

$$\int_V \rho\, \ddot{\mathbf{u}}\, dV = \int_V \mathbf{f}\, dV + \int_S \mathbf{T}(\mathbf{n})\, dS \tag{2.6}$$

$\mathbf{f}$ is an applied body force to the media, ρ is the density, $\mathbf{u}$ is the displacement the particles. It is assumed that the mass of the particles remains constant in time (i.e. mass conservation). $\ddot{\mathbf{u}}$ is the acceleration of the particle. $\mathbf{T}$ is the traction vector applied to surface S which is defined as the force acting per unit surface S, i.e.

$$\mathbf{T}(\mathbf{n}) = \lim_{dS \to 0} \frac{\delta \mathbf{F}}{\delta S} \tag{2.7}$$

The traction tensor can also be rewritten in terms of the second order stress tensor σ_{ij}:

$$T_i = \sigma_{ji}\, n_j \tag{2.8}$$

where T_i is the traction vector of surface i.

As the traction tensor obeys Newton's third law of motion (and is continuous across a fault boundary) we can say:

$$\mathbf{T}(-\mathbf{n}) = -\mathbf{T}(\mathbf{n}) \tag{2.9}$$

where $\mathbf{n}$ is the normal vector to the surface S. Substituting equation 2.8 and applying the Divergence Theorem to the surface integral in equation 2.6 we get the equation of motion:

$$\rho\, \ddot{u}_i = f_i + \sigma_{ji,j} \tag{2.10}$$

where the vectors have now been replaced by there components (i.e. $\mathbf{u}$ has been changed to the i^{th} component of $\mathbf{u}$). $\sigma_{ji,j}$ is the rate of change of the stress tenor in relation to the j^{th} component as is related to the rheology of the media.

2.1.3 Hookes Law

We shall now define the nature of the interaction between stress and strain on the fault so that the equation of motion (equation 2.10) can be re-written in terms of displacement.

The generalised Hooke's law shall be used as our constitutive equation whereby stress is proportional to list of linear components in the strain tensor:

$$\sigma_{ij} = c_{ijkl}\, e_{kl} \tag{2.11}$$

where σ_{ij} is the stress tensor, e_{kl} is the strain tensor and c_{ijkl} is a 4th order tensor of constants.

Assuming that the medium is isotropic, Jeffreys and Jeffreys [1972] showed that $\mathbf{c}$ has the form:

$$c_{ijkl} = \lambda\, \delta_{ij}\delta_{kl} + \mu\, (\delta_{ik}\delta_{jl} + \delta_{il}\delta_{jk}) \tag{2.12}$$

where δ_{ij} is a Kronecker delta, λ and μ are Lame constants. Therefore Hooke's Law (equation 2.11) can be rewritten as:

$$\sigma_{ij} = \lambda\, \delta_{ij}\, e_{kk} + 2\mu\, e_{ij} \tag{2.13}$$

with σ_{ij} representing the stress on the i^{th} plane in the j^{th} direction.

2.1.4 Elastodynamic Equation

Combining equations 2.13 and 2.5, the equation of motion (equation 2.10) can now be rewritten in terms of the displacement exclusively:

$$\rho\, \ddot{u}_i = f_i + \{\lambda\, \delta_{ij}\, u_{k,k} + \mu\, (u_{i,j} + u_{j,i})\}_{,j} \tag{2.14}$$

Therefore we can now calculate the displacement for a given particle (i.e. $\mathbf{u}$) for a given position and time in a medium due to the application of a body

force (i.e. $\mathbf{f}$). Therefore we can solve the displacement (i.e. $\mathbf{u}$) for a given particle in terms of one second order hyperbolic equation (equation 2.14).

In the case of the dynamic modelling presented in this report, the body force is set to zero (i.e. $\mathbf{f} = 0$).

2.1.5 Rupture Boundary Conditions

Once the stress on the fault reaches the yield stress, the fault begins to slip (i.e. just behind the fracture tip slip between the sides of the fault occur). This slip is a discontinuity in the particle displacement either side of the fault defined which (Madariaga and Olsen [2002]) defined as:

$$\delta(\mathbf{x}, t) = ||u^+(\mathbf{x}, t) - u^-(\mathbf{x}, t)|| \tag{2.15}$$

where δ is the slip at point $\mathbf{x}$ on the fault and time t. $u^+(\mathbf{x}, t)$ and $u^-(\mathbf{x}, t)$ are the displacements either side of the fault. For this chapter, as we shall be using a homogeneous media, we shall assume that the model is symmetric with respect to the fault plane.

Rupture can be initiated for a small patch in the model by:
(a) decreasing the yield stress
(b) setting the pre-stress higher than the yield stress
(c) forcing slip to occur.
In this chapter rupture shall be initiated using method (b).

This slip (defined by equation 2.15), by means of the elastodynamic equation (equation 2.14), changes the traction on the fault, which can be represented as:

$$\Delta\mathbf{T} = G(\mathbf{D})$$

where $\Delta\mathbf{T}$ is the change in the traction vector on fault surface, while $G(\mathbf{D})$ is some function of slip on the fault. As the slip rate increases for a given point on the fault the traction decreases at the same point, the relationship between the two (i.e. stress and slip rate) is governed by the friction law.

2.1.6 Friction Laws

One single rupture criterion consists in assuming that rupture occurs when the local stress (σ) is greater the strength or yield stress of the medium (σ_y). When this condition is met stress on the surface is governed by a friction law. The friction law can be in terms of fault traction (F) as:

$$F = \mu(\Delta u, \Delta \dot{u}, \theta)\sigma_n \tag{2.16}$$

where σ_n is the normal stress to the fault. $\mu(\Delta u, \Delta \dot{u}, \theta)$ is the coefficient of friction which can be dependent on the slip, Δu the slip rate $\Delta \dot{u}$ and one or more state variables θ. Owing to particular properties of the fault surface and the medium (e.g. cohesion, micro-contacts on the fault, pore fluid pressure, presence of melted rock etc.), the coefficient of friction is assumed to evolve with slip. Two types of friction laws were used in our dynamic models the first a Rate and Slip Weakening (RSW) law proposed by Nielsen and Olsen [2000], the second a variation of the Rate and State (RS) friction law which was defined by Nielsen and Carlson [2000]. The components of which shall now be discussed.

Rate and Slip Weakening

Ida [1972] initially defined a relationship between the evolution of the fault cohesion with slip. Whilst Ida defined a number of different types of possible functions the most popular is defined in relation to the friction which decreases linearly Madariaga and Olsen [2002]:

$$\mu(\Delta u) = \begin{cases} \mu_s - \frac{\mu_s - \mu_d}{D_c}\Delta u & \Delta u < D_c \\ \mu_d & \Delta u \geq D_c \end{cases} \tag{2.17}$$

where Δu is the slip, μ_s and μ_d is the static and dynamic coefficient of friction respectively. D_c is the critical slip distance over which the coefficient

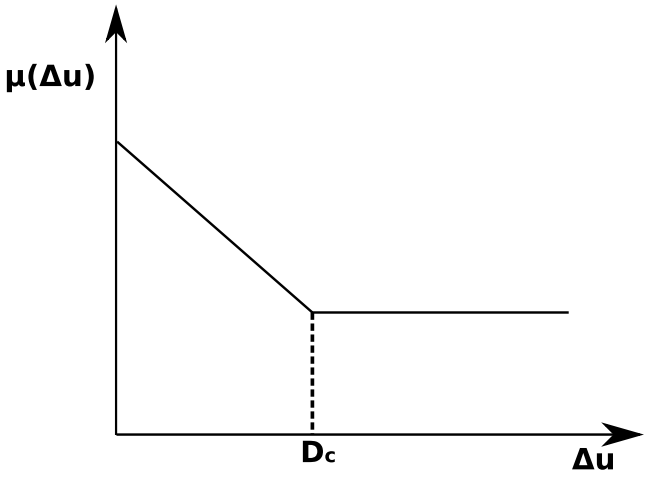

Figure 2.1: A schematic of the variation of the coefficient of friction with increasing slip for one given point. Δu_c is the critical slip distance

of friction μ decreases to a lower dynamic level (see figure 2.1). This type of friction law creates a crack-like a type of fracture whose healing phases (i.e. decrease in slip) is created only by the interaction of the rupture front with a stopping barrier.

Another widely used constitutive law is the rate friction law, proposed by Dieterich [1979] where the coefficient of friction decreases with increasing slip rate ($\Delta\dot{u}$). An example of a rate friction law is:

$$\mu(\Delta\dot{u}) = \mu_o + A\ \log(B\frac{d_c}{\Delta\dot{u}} + 1) \tag{2.18}$$

where the value d_c is taken to be characteristic length which scales with roughness. A, B and μ_o are constants with values ranging between 0.01-0.02, 1.0-2.0 and 0.6-0.8 respectively (Dieterich [1979])

Nielsen and Olsen [2000] applied a combination of the two mechanisms (i.e. the slip weakening and rate weakening). This friction law (which we shall abbreviate to RSW law) applies the friction law which produced to

higher stress on the fault for a given time and place (thus producing the lowest possible slip). Their definition of friction F is defined as:

$$F = \sigma_y \, \mathrm{Max}[\frac{1}{1 + \frac{\Delta \dot{u}}{V_c}}, \frac{1}{1 + \frac{\Delta u}{D_c}}] \tag{2.19}$$

where σ_y is the yield stress, $\Delta \dot{u}$ and Δu are the slip rate and slip on the fault respectively whilst D_c and V_c are the characteristic slip and rate weakening parameters. By taking the maximum of the either friction law we shall be taking the stronger of the two friction laws for a given position and time. In practice, this means that we shall expect the slip weakening law to dominate at the initiation of slip, whilst velocity weakening shall take over at larger slips as the slip weakening friction law drops to a low value. Figure 2.2 is a graphical representation of this. Equation 2.19 is one of the friction laws used in the proceeding section.

Rate and State Friction Law

Based on experimental evidence, Ruina [1983] introduced the state variable, θ, to Dietrich's rate friction law with idea to accommodate interactions on the fault (e.g. temperature, pressure, chemical environment, evolution of contact asperities) that would evolve with certain fault parameters (i.e. rise time, slip, slip rate etc.). Therefore the state variable represents the weakening of the fault plain as rupture time increases.

The rate of the state variable (i.e. $\dot{\theta}$) can depend on a number of different variables (i.e. normal stress, slip rate, etc.). Madariaga and Olsen [2002] define a general state law as:

$$\dot{\theta} = \frac{V_c}{L} G(\dot{D}, \theta) \tag{2.20}$$

where V_c is a characteristic slip rate and L is a "weakening distance" which defines a slip distance after which friction reaches a steady state. $G(\dot{D}, \theta)$ is

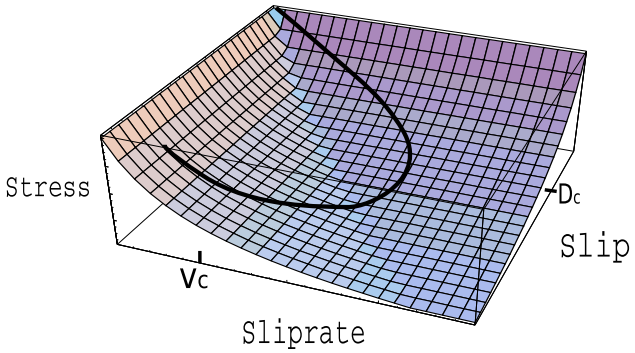

Figure 2.2: This is graphic representation of the slip and rate weakening friction law. The surface represents equation 2.19 whilst the black line denotes the variation in stress at a given point which initially where by friction is predominantly controlled by the slip weakening friction law. As rupture continues the sliprate decreases making the slip weakening friction law the dominant friction law. This leads the arrest of slip, and so stress begins to increase again due to seismic radiation from other parts of the fault.

some simple function of the slip rate $\dot{D}$ and/or the state variable θ. It should be noted that the state variable is non-diffusive (i.e. the value of the state variable for a given position does not effect its neighbouring points).

Nielsen and Carlson [2000] RS friction law differs from the commonly used RS friction law in that it does not take the logarithm of variables. Their friction law is defined in equations 2.21 and 2.22. θ can vary between 0 and 1 and its rate of change depends on the sliprate, $\Delta\dot{u}$, as well as a predefined characteristic time τ and a characteristic length δ.

$$F = \sigma_y \theta \tag{2.21}$$

$$\dot{\theta} = \frac{1-\theta}{\tau} - \frac{\Delta\dot{u}}{\delta}\,\theta \tag{2.22}$$

The values of τ and δ were chosen in such a way as to create self healing pulses and shall be discussed in more detail in section 2.3.

For the majority of the results presented in this paper the rate and state friction law was used. All figures assume rate and state unless otherwise specified.

2.1.7 Model Boundary Conditions

The boundary conditions on edges of the models can be broken up into three distinct groups: the Dirichlet, Neumann and PML boundary condition. All three types of boundaries shall be used in our dynamic models.

Dirichlet Boundary Condition

A boundary defined using the Dirichlet boundary condition states that the particle displacement on boundary S is defined by $g(\mathbf{x}, t)$ as shown in equation 2.23 below:

$$u(\mathbf{x},t) = g(\mathbf{x},t) \;\; for\, \mathbf{x}\,\epsilon\, S \tag{2.23}$$

$$\tag{2.24}$$

In the case of a rigid boundary $g(\mathbf{x},t)$ is set to 0. This boundary shall act as a solid non.elastic surface which reflects waves but does not absorb them.

Neumann Condition

The Neumann boundary condition defines a value $g(\mathbf{x},t)$ on boundary S for the normal gradient of displacement (which is similar to the traction vector $T(\mathbf{x},t)$):

$$\mathbf{T}(\mathbf{x},t)\,.\,\mathbf{n} = \mathbf{g}(\mathbf{x},t) \;\; for \mathbf{x}\,\epsilon\, S \tag{2.25}$$

$$\sigma_{ij}\, n_j = g_i \tag{2.26}$$

For a free surface boundary conditions the traction is set to zero (i.e. $\mathbf{g}(\mathbf{x},t) = 0$). This shall be used to simulated the earths surface in Chapter 4, where by traction is zero normal to the earth's surface

To cut down on computational time mirror boundaries have been used in the initial simulations of this chapter when the pre-stress has a geometric symmetry. This allows the computational time to be cut to $\frac{1}{8}$ of the original time when three mirror boundaries are used in 3D medium. For a mirror boundary , the traction vector on surface S is usually defined by equation 2.27 below:

$$T(\mathbf{x},t)_{sym} = T(\mathbf{x},t) - 2\,\mathbf{n}\,(T(\mathbf{x},t)\,.\,\mathbf{n}) \tag{2.27}$$

where $T(\mathbf{x},t)_{sym}$ is the symmetric traction vector on surface S where $\mathbf{n}$ is the unit normal vector to the boundary surface S. However with the presence of a fault in the media, symmetry conditions must obey those seen across a fault plane. Such conditions vary the mirror boundary conditions for those

boundaries which intersect the fault plane, a further discussion on defining mirror boundaries in the presence of a fault plane is provided in appendix 2.A.2.

PML Boundary Condition

In most situations we shall want our model to act as an infinite medium and is thereby unaffected by the model's limited size. For this reason we shall apply Perfectly Matching Layer (PML) boundary (Berenger [1996], Chew and Liu [1996] and Festa and Nielsen [2003]) to the sides of the model from which we do not want waves to reflect off. Instead of taking a surface S a volume V is used, over which elastodynamic perturbations are dampened before reaching surface S where a Dirichlet boundary condition is applied. Dampening is preformed by applying a stretching factor $\mathbf{S}$ to the gradient of the stress tensor in the boundary volume. Chew and Liu [1996] defined $\mathbf{S}$ in the x direction as:

$$S_x = 1 - \frac{i\,\alpha^x(q)}{\omega} \tag{2.28}$$

With ω denoting the frequency and i is imaginary. $\alpha^x(q)$ is a real scalar function dependent on the the distance q from the Dirichlet boundaries which is defined:

$$\alpha(q) = A\frac{c_p}{h\,\delta x}(\frac{q}{h})^n \tag{2.29}$$

where q is the distance in grid points from the interface, c_p is the p-wave velocity, h is the number of nodes that makes the thickness of the absorbing layer. A is a non dimensional constant related to the attenuation with a value of 5 and n can have values of 2, 4 and 5 - all of which give acceptable results (Festa and Nielsen [2003]).

2.2 Numerical Method

As dynamic fracture models have only been solved analytically for limited set of cases (for e.g. Kostrov [1964], Rice et al. [2005],Nielsen and Madariaga [2003] and Dunham [2007]) we shall solve them numerically. The three principle numerical techniques used are finite difference, spectral element and boundary integral method.

Finite difference methods for dynamic rupture (initially proposed by Madariaga [1976]) to calculate the elastodynamic equations for a set of points in a grid. Models using this method are simple and relatively fast. However, its disadvantage is that only limited fault orientations can be accommodated and that grid distribution must be carefully constructed in order to reduce numerical instability.

The spectral element technique (Komatitsch et al. [1999]) discretizes a media into area or volume elements (depending on whether a 2D or 3D system is being simulated). The numerical integration inside each element (i.e. solving the elastodynamic equation) is calculated using the tensor product of the Gauss Lobatto Legendre integral. The solution of which is expanded to encompass whole element using Lagrange interpolation. Whilst it is more accurate than finite difference modelling however it is also a more computationally expensive method and grid construction can be a very time consuming process.

The boundary Integral method initially developed by Das and Aki [1977] whereby slip on the fault is computed by means of integration on the causality cone for shear and Rayleigh waves. This integration is preformed by means of a 4th order spatial interpolation. This method was subsequently modified by numerous authors (Quin and Das [1989] ,Fukuyama and Madariaga [1995], Tada et al. [2000]) who removed the hyper singularities that were present near the rupture front as well as extend the technique to 3D. A disadvantage

of the technique is that it cannot deal with heterogeneous media layers.

As we shall be running numerous simple dynamic models a rapid numerical method is preferential which would point to using finite difference over spectral element. Given that we shall be examining deterministic features of rupture and not fault geometry we are unconcerned about being limited to a planar fault, thus making finite difference a better choice to the spectral element technique.

As finite difference provides the best compromise between accuracy (in terms of the simple type of rupture model that we are examining) and computational time required for each simulation, we shall use it for our dynamic numerical investigation. The application of finite difference to dynamic rupture is discussed in detail in the appendices of this chapter (i.e. section 2.A.1).

2.3 Crack Vs Pulse Rupture Models

As was mentioned in the previous section, the choice of friction law determines the nature of the fracture that is produced. There are two principal modes for dynamic fracture propagation: crack-like and pulse-like. Crack-like ruptures are created when friction remains permanently low on the fault after failure occurs. Pulse-like ruptures, on the other hand are formed by some mechanism of dynamic frictional strengthening.

A cracks friction law is commonly defined by slip weakening (equation 2.17) although many different types of friction laws can be used to create them (e.g. Coulomb, Rate and State etc. - see Zheng and Rice [1998] and Nielsen and Carlson [2000] for a more detailed discussion).Whilst crack rupture can be solved analytically for simple cases (e.g. Kostrov [1964] for a self similar crack) their healing conditions depend on the presence of fault boundaries. Therefore healing and arresting waves are only generated at

the edges of the fault meaning that rupture heals from the edge of the fault inwards.

This outside-in healing condition observed with cracks means that earthquakes created using crack conditions shall have large rise times. Heaton [1990], however, observed that rupture is seldom larger than 10% of the final rupture size. Heaton [1990] proposed that dynamic rupture could be characterised by a "narrow self-healing pulse of slip"; a model initially suggested by Haskell [1964] in order to explain the frequency spectra of earthquakes. This gives rise to the second type of rupture – the pulse.

For a rupture pulse a healing front trails the rupture front. A healing front is generate by assuming for example rate-weakening friction, allowing friction to re-strengthen rapidly after failure (Nielsen and Carlson [2000]) Since the healing front is trailing the rupture, this means that pulses heal in the opposite sense to cracks - i.e. from the centre of the fault outwards. An example of slip weakening being used to create a crack has been highlighted in figure 2.3a whose healing mechanism is independent of the critical distance D_c. A pulse on the other hand (as depicted in figure 2.3b) naturally creates a healing front when the slip rate naturally falls below the predefined V_c. If, however, the characteristic velocity is decreased the pulse's length increases until if finally becomes a crack (Nielsen and Carlson [2000]).

In terms of EW, we are investigating whether in some models, fracture size may be determined by the initial part of rupture history. As stated previously, crack-like fracture requires the interaction of barriers in order to start healing, a feature which is dependent on final rupture dimensions of an earthquake. This is supported by Ripperger et al. [2006] whose numerical study of cracks in a heterogeneous pre-stress found that scaling between final rupture size and initial stress drop exists only for a very limited range. Pulses, on the other hand provide some degree of independence from barriers as healing depends on the slip rate. For this reason we shall use the rate

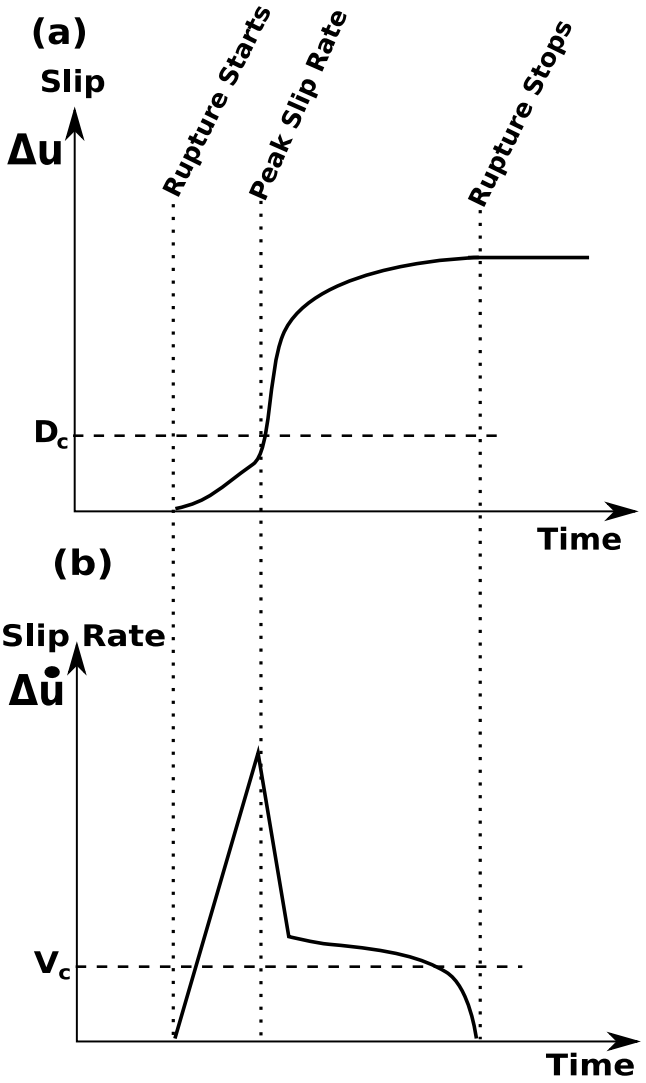

Figure 2.3: A stereotypical schematic of (a) the slip and (b) the slip rate against time for a particle on a fault as the rupture front passes over it. In (a) D_c denotes the critical slip which is used to define the slip weakening frictional law, slip will not drop below D_c once it has passed it. Figure (b) defines V_c the critical velocity used in the rate weakening friction law, given the high variation of the slip rate with time it is possible for healing to occur independently of unbreakable barriers.

weakening friction laws defined by equations 2.19, 2.21 and 2.22 to create self-healing pulses. Rate friction laws can be used to create both crack and pulse modes of rupture with features such as the pre-stress (Zheng and Rice [1998]), frictional parameters and trigger location determining the nature of rupture (Nielsen and Carlson [2000]).

Indeed Nielsen and Carlson [2000] examined how, under a given prestress, variations in the frictional parameters δ and τ used in equations 2.21 and 2.22 lead to three different rupture regimes: self similar cracks, self similar expanding pulses and transient arresting pulses. After constructing a phase diagram based on 400 numerical simulations, they found that the fracture regimes are defined by lines of constant characteristic velocity (i.e. δ/τ – see figure 2.4). Whilst Nielsen and Carlson [2000] phase diagram (figure 2.4) corresponds to a constant pre-stress, it shall aid our choice of values for δ and τ, thus reducing the time required to find a self-similar pulse. As stated previously our interest is to create rupture's with some deterministic features, therefore we shall concentrate on creating the transient arresting pulses seen by Nielsen and Carlson [2000].

2.4 The Asperity Model

Numerous authors (e.g. Ida [1972], Andrews [1976a], Day [1982] and Madariaga and Olsen [2000]) all demonstrated that a critical half crack length (L_c) is required in order to propagate into an surrounding area with a given pre-stress. Ida [1972] originally defined the critical length in order that rupture propagate using a slip weakening friction law for antiplane case:

$$L_c = \frac{\mu\, D_c}{\pi} \frac{\sigma_y}{\sigma_{ext}^2} \tag{2.30}$$

where μ the shear modulus,σ_y is the yield stress of the medium and the pre-stress of the asperity, σ_{ext} is the pre-stress of the surround area outside length

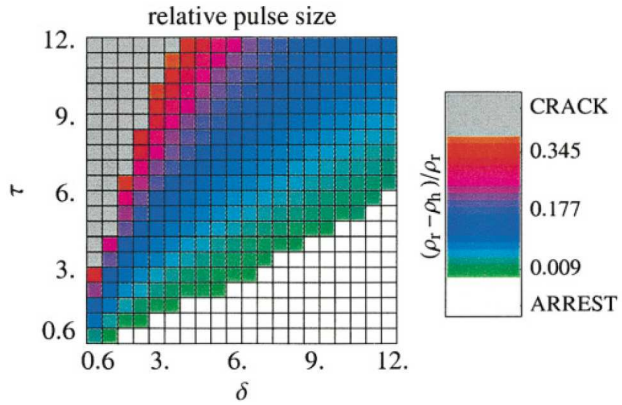

Figure 2.4: This phase diagram highlights the different types of rupture (denoted by different colours) produced for different values of τ and δ, the frictional parameters in equation 2.22. Grey represents crack-like rupture, red to green rupture pulse which decrease in pulse length going from red to green. Finally white signifies models where rupture is very small or non-existent. The change in the nature of rupture is defined along lines of δ/τ.The diagram is based on the results of 400 dynamic simulations. From Nielsen and Carlson [2000]

L_c. Finally D_c is the critical slip. Subsequently, Andrews [1976a] defined a similar length scale for the in-plane critical length defined as:

$$L_c = \frac{1}{\pi\,(1-v)}\frac{\sigma_y\,\mu}{\sigma_{ext}^2}\,D_c \tag{2.31}$$

where v is Poisson's ratio. For both equations 2.30 and 2.31 we assume that residual stress after rupture is zero and that the stress distribution is that due to a static crack. For dynamic rupture, equations 2.30 and 2.31 are influenced by the rupture velocity, At present no similar equation is available for pulse-like rupture. In essence equations 2.30 and 2.31 highlight that a minimum balance between crack dimensions and prestress is required in order for rupture to propagate. This is somewhat analogous to the situation in our dynamic models. However, for our numerical simulations rupture shall not be initiated with on open crack (or pulse), put rather with a pre-stress greater than that of the medium. The resulting rupture shall require a stress which is large enough to provide the rupture with enough elastostatic energy (G_e) to continue to propagate. In order to provide such an energy the pre-stress at and near nucleation need be high.

Such a region of high pre-stress shall be defined as "asperity" (Madariaga [1983]). Similar to equations 2.30 and 2.31 the length scale of the asperity, the pre-stress outside it, and, in the particular case of an asperity, the pre-stress inside of the asperity shall all effect rupture propagation. Therefore if the pre-stress inside/outside or the size of the asperity is too small rupture shall not extend outside of the asperity. Essentially it these relationship between asperity features and final rupture size that we shall investigate.

A number of numerical investigations have thus far examined dynamic rupture in asperities. Das and Kostrov [1983] first examined rupture inside an asperity using the boundary integral method. As they wanted to account for pre-slip on the fault plane the pre-stress distribution inside the asperity was defined such that it increases towards the asperities edge. The stress

outside of the asperity was set to zero thus limiting rupture to occur only inside the asperity. This pre-stress distribution forces the rupture front to encircle the centre of the asperity before breaking it. Das and Kostrov [1983] termed this rupture propagation features the "encircling pincer movement".

Fukuyama and Madariaga [2000] also used an asperity model in there investigation on the relationship between rupture velocity and pre-stress used a similar asperity model (i.e. one with a high stress around the edge of the asperity). Whilst also using a 3D BIE method, in this case the resolution of the model was better and the rupture was allowed to occur outside of the asperity. Fukuyama and Madariaga [2000] produced similar rupture propagating features seen by Das and Kostrov [1983] calling the meeting of the two rupture fronts on the far side of the asperity (in relation to the point of nucleation) as "rupture focusing".

More recently Dunham et al. [2003] and Page et al. [2005] investigated the interaction between a mode II crack and a circular barrier. Similar to Fukuyama and Madariaga [2000] and Das and Kostrov [1983] rupture encircles the barrier before breaking it, causing rupture front focusing. Dunham et al. [2003] noted that this feature is not as pronounced of anti-asperity model (i.e the asperity contains a low pre-stress) as the rupture front penetrates them easier.

None of the previously mentioned authors consider self-healing fracture pulses. We argue that pulses are important because their fracture energy and the way they scale with rupture dimension fundamentally differs from that of the classical crack model (Nielsen and Madariaga [2003]).

Finally, we shall not account of the pre-slip on the asperity as we are interested only in the relationship between the asperity, its size and the pre-stress outside of it. Therefore we shall assume that pre-stress variation inside the asperity is insignificant in relation to the difference in stress inside and outside the asperity.

2.5 Model Setup

As we are examining how initial rupture features effect final rupture size we shall take a very simple pre-stress distribution on our fault which we then vary gradually. Nucleation is forced to occur in one specified location by putting the pre-stress at that point greater than the yield stress of the medium. This zone shall be referred to as the "trigger zone". The trigger zone is at least four times smaller than the asperity size so that its effects are insignificant to that of the asperity's. It is important to note that, for simplicity, we have used a rapid nucleation procedure that by-passes the slow nucleation stages. Indeed we are not looking at the quasi-static initial transient but at the dynamic breakaway phase (i.e. the first few seconds of rupture).

In all cases the nucleation zone has been placed inside a high stress circular asperity. The location of the trigger zone inside the asperity as well as the asperities size varies between models. Initially, a homogeneous background pre-stress was applied outside the asperity in order to determine what, if any, are the constraints that nucleation places on the overall rupture. In later models a heterogeneous pre-stress background was added outside the asperity to see how this would effect rupture propagation. In creating a random pre-stress distribution we want to produce rupture on a fault that is somewhat realistic, a more detailed discussion on which is presented in section 2.6.1 Figure(2.5) depicts a schematic cross-section through the pre-stress on our planar fault.

The fault is assumed to be in an infinite medium (i.e. no waves reflect off the model boundaries) as PML boundaries (Festa and Nielsen [2003]) were applied to the edges of the model.

Where possible, the theoretical models have been scaled to make our theoretical models analogous with observational results. For example, abstract fault parameters such as the total moment have been converted into the

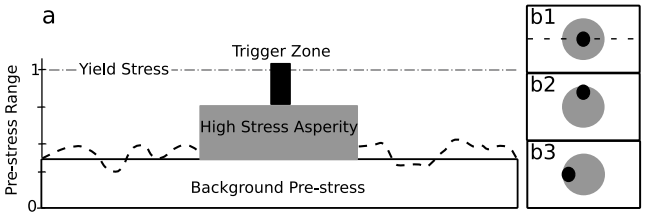

Figure 2.5: Schematic description of fault initial conditions. (a) cross-section of pre-stress distribution on the fault (for a case where trigger is located at the centre of the asperity). The dotted line highlights the fact that for certain models the homogeneous pre-stress outside of the asperity was replaced with a heterogeneous one. (b1-3) planar views of pre-stress distributions on the fault for three different trigger positions (black dots). (b-1) Centre case (trigger in the middle of asperity), (b-2) Antiplane edge: the trigger is on the top edge of the asperity, so that slip is locally tangent to the asperity border. (b-3) Inplane edge: the trigger is on the left side of the asperity, so that slip is locally perpendicular to the asperity border.

more widely used moment magnitude. Another incentive for scaling is that it makes our theoretical models which have slightly pre-stress distributions which differ slightly, comparative. Table 2.4 contains a list of the scaling applied to our theoretical models and the effect this scaling has on asperity size. For this conversion the yield stress, τ_y, is equal to 30MPa whilst the shear stiffness, μ, is set to 30GPa. The exception to this is scaling is figure 2.7, where the graphs units (moment rate and length) have been left in model units.

2.6 Dynamic Results

2.6.1 Quantitative description of pulse rupture

Figure 2.6 is an example of the evolution of a pulse from our asperity model with a homogeneous pre-stress surround it. In general, we observe that rupture is faster in the the in-plane direction (i.e. the direction parallel to the direction of the pre-stress - which in the case of figure 2.7 is in the horizontal direction). This difference in rupture velocity is a common feature of rupture (Madariaga and Olsen [2002], Fukuyama and Madariaga [2000] and Kostrov [1964]) which is due to production of s- and Rayleigh waves in the in-plane direction causing stress fluctuation thus moving the media nearer to rupture faster (Madariaga and Olsen [2002]).

In comparison to earlier studies of numerical models, we do not see the "double pincer" rupture effect (Kostrov [1964]) nor the "rupture focusing" (Fukuyama and Madariaga [2000]). The absence of these features is due to the lack of pre-stress variation inside of the asperity.

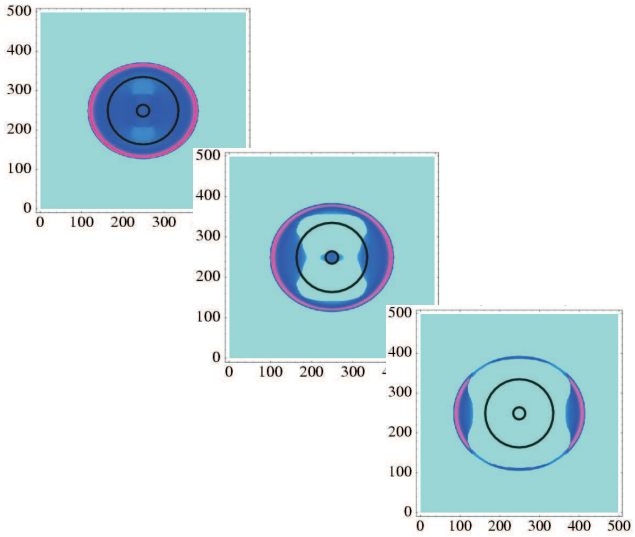

Figure 2.6: The three pictures highlight the evolution of a rupture pulse from a trigger (inner black circle) through the high stress asperity (i.e. outer black circle) into the surrounding low stress medium.

2.6.2 Sensitivity test on parameters that are important to rupture length

As stated in section 1.4, a large initial fracture energy flux (G_e) has a higher probability of creating larger earthquakes. As the energy flux is proportional to the stress drop (i.e. $\Delta\sigma^2$) and active rupture length (i.e. Λ), it can be linked to the moment rate, $\dot{M}_o$ (Nielsen [2007]) . The moment rate in turn, is itself proportional to the particle displacement in the far field and thus the fracture energy flux is indirectly observable on the seismogram (Aki and Richards [2002]). This indirect correlation is highlighted in equation 2.32 below:

$$u(t) \propto \dot{M}_o \propto \Delta\sigma\,\Lambda \tag{2.32}$$

$$G_e \propto \Lambda\Delta\sigma^2 \tag{2.33}$$

Therefore, a large initial amplitude, a feature measured by Zollo et al. [2006], Wu and Zhao [2006],etc, could relate to a large energy flux during the start of rupture. Equation 2.32 and 2.33 demonstrate that by varying the stress drop and the active rupture length we shall vary the moment rate, a function that both influences the energy flux and is seismologically observable. Therefore, by varying the pre-stress on our numerical fault for different models we hope to vary the stress drop and hence the initial elastostatic energy. One means of examining the evolution of the energy flow in our model over time is by measuring the moment rate during the course of rupture. We shall now, initially investigate whether such a scaling holds true by comparing the moment rate created by an asperity with its final rupture length.

Assuming that rupture inside of the asperity is crack-like, we can define the moment for a circularly expanding crack as:

$$M_o(t) = 2\pi\,\mu \int_0^{r(t)} \Delta u(r,t)\, r\, dr \tag{2.34}$$

where μ is the shear modulus, r is the radius of the crack at time t and Δu is the slip at position r and time t Using Leibniz Integral Rule the time derivative of equation 2.34 can be taken, giving the moment rate as:

$$\dot{M}_o = 2\pi\,\mu\{\int_0^{r(t)} r\,\Delta\dot{u}(r,t)\,dr\; + r(t)\,\Delta u(r(t),t)r'(t)\} \tag{2.35}$$

assuming that slip is infinitesimal near the crack tip (i.e. the rise time is not instantaneous) , $\Delta u(r(t),t) = 0$ and therefore the second term in equation 2.35becomes zero. The moment rate for a crack at time t is:

$$\dot{M}_o = A(t)\,\mu\,\overline{\Delta\dot{u}} \tag{2.36}$$

where $\overline{\Delta\dot{u}}$ is the average slip rate inside the crack, and $A(t)$ is the area of the crack at time t (i.e. $A(t) = \pi\,r(t)^2$)

Eshelby [1957] defined the slip for a static circular crack as (which is a resonable approximation for the dynamic crack which Scholz [2003] claims differs by 20%):

$$\Delta u(x,y) = \frac{12\,\Delta\sigma_s}{7\pi\,\mu} L\sqrt{1-\frac{x^2+y^2}{L^2}}$$

where (x,y) is a point on the fault, L is the final radius of the fault, $\Delta\sigma_s$ is the static stress drop. Therefore the average slip on a circular fault can be given in spherical coordinates as:

$$\overline{\Delta u} = \frac{1}{\pi L(t)^2}\frac{12\,\Delta\sigma_s}{7\pi\,\mu}\,L(t)\int_0^{2\pi}\int_0^{L(t)}\sqrt{1-\frac{r(t)^2}{L^2}}r(t)drd\theta$$

whereby the integral evaluates to:

$$\int_0^{2\pi}\int_0^{L(t)}\sqrt{1-\frac{r(t)^2}{r(t)^2}}r(t)\,dr\,d\theta = \frac{2\,\pi\,L(t)^2}{3}$$

giving an average slip of:

$$\overline{\Delta u} = \frac{8}{7\pi}\frac{\Delta\sigma_s}{\mu}L(t) \tag{2.37}$$

By taking the temporal derivative of equation 3.19 and setting the rate of change in the rupture length ($\dot{L}(t)$) equal to the the average rupture velocity ($\overline{v_r}$) we can now define the average sliprate on the fault plane. The average sliprate can now be defined as

$$\overline{\Delta\dot{u}} = \frac{12}{21\pi}\frac{\Delta\sigma_s}{\mu}\overline{v_r} \tag{2.38}$$

Substituting equation 2.38 into 2.36 gives the moment rate in terms of the stress drop:

$$\dot{M}_o = A(t)\,\frac{12}{21\pi}\Delta\sigma_s\overline{v_r} \tag{2.39}$$

By setting the area and stress equal to that of the asperity's and defining the average rupture velocity as:

$$\overline{v_r} = 0.9\,\beta \tag{2.40}$$

, β is the s-wave velocity we can now calculate an estimate for the maximum moment rate created by the asperity. As λ, ρ and μ were all equal to 1 (see table 2.2) this means that $\beta = \sqrt{3}$, and thus $\overline{v_r} = 1.57$ (it should be noted, that for this preliminary model, non-dimensional parameters were used) .

In terms of determining the rupture length (i.e. the distance from the point of nucleation to the place where rupture terminates) an approximation shall be made to the differences in rupture lengths between the in- and anti-plane. Therefore we shall let the average rupture length ($\overline{R_L}$) be equal to the radius derived from the total ruptured area (A_r) assuming this area is circular:

$$\overline{R_L} = \sqrt{\frac{A_r}{\pi}} \tag{2.41}$$

where $\overline{R_L}$ is the average rupture length.

Figure 2.7 plots the maximum moment rate of the asperity (given by equation 2.39) for a variety pre-stress distributions on the fault plane (see table 3.5) against the average rupture distance (defined by equation 2.41). The different symbol represent three different pre-stress regimes. Box (■)

and the triangular (▲) symbols denote where the asperity radius was kept constant with only the pre-stress inside of the asperity increasing. The difference between the box and triangular models being the size of the asperity. The star (★) symbols represent where the asperity size is increased whilst the pre-stresses remain constant.

With both the box and triangular plots, when the asperity generates a low moment rate the the rupture length remains at an initially low plateau. There is then a jump in rupture length denoting the point at which rupture now has enough elastostatic energy to propagate outside of the asperity. This point is similar to the critical length of cracks discussed previously (see Section 2.4) and shows a coincidental dependence on length and pre-stress. This similar interdependency between stress and asperity size can be seen by the sudden jump in rupture length over a small increase in the stress drop inside of the asperity and secondly in the different moment rates required to produce a jump in rupture length between the square and rectangular symbols (whose asperity size differs).

After the jump in rupture length, the maximum moment rate created by the asperity scales linearly with the rupture length. This is true for all three regimes types (i.e. square, triangle and boxes).

In essence figure 2.7 shows a promising linear scaling between the final rupture length and the moment rate of the asperity. This scaling occurs after a characteristic elastostatic energy has been obtained by rupture in the asperity. The scaling occurs for both increasing asperity prestress and asperity size. However on close examination of figure 2.7 it appears that the asperity prestress is important for reaching the critical energy required for rupture outside of the asperity. The asperity's radius, on the other hand provides the largest scaling range outside of the asperity.

Having produced a promising simple scaling between the maximum moment rate and rupture length we shall now look at the different relationships

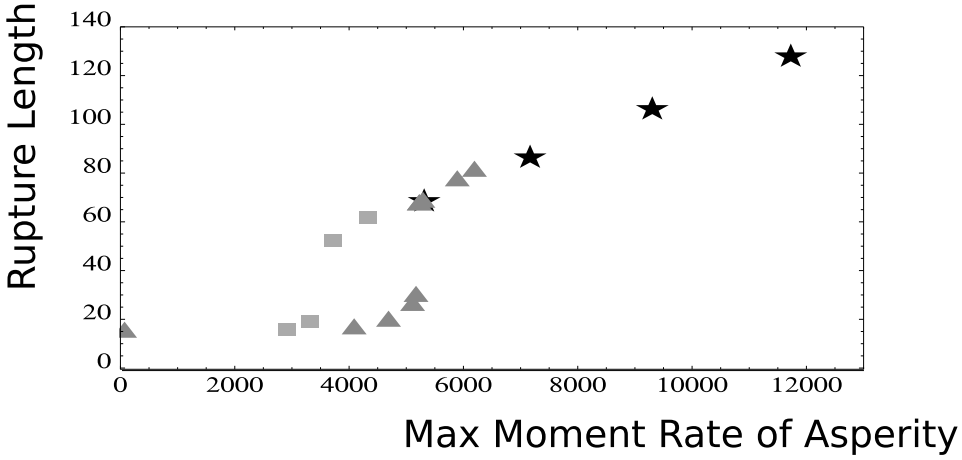

Figure 2.7: This is a plot of the average rupture length against the moment rate created by the asperity. The different symbols denote different pre-stress regimes see table 3.5 in the appendix for stress distributions. In the case of the boxes (■) and the triangles (▲) , the asperity size was kept constant with only the pre-stress being steady increased in both cases. For the stars (★), the radius of the asperity was increased whilst all other parameters were kept constant. Note all units in this case are non-dimensional.

between asperity size, trigger position and final magnitude using the more complex rate and state friction law.

2.6.3 Moving Trigger Location

On viewing the final slip for a variety of asperity models with homogeneous background pre-stress in figure 2.8, it is apparent that the relative position of the trigger patch inside the asperity is important in predefining rupture direction. When the trigger area is on the edge of the asperity, rupture only propagates uni-directionally through the asperity and out the other side (figure 2.8b, c).When the trigger patch is in the centre of the asperity (figure 2.8a) a bi-direction rupture front is produced. A possible reason for this bi-directionality of rupture in the anti-plane direction is difference in the stress intensity for the in-plane and anti-plane directions. In figure 2.8d, the trigger is off centre and as a result slip is primarily in the anti-plane direction, but the rupture front still propagates to a smaller extent in the in-plane direction. In all cases maximum slip occurs at the edge of the asperity and points in the general direction of principle rupture.

Interestingly, where the trigger is at the edge or centre of the asperity (figure 2.8a,b,c), the rupture's width is limited to the diameter of the asperity. This focusing of the rupture front (which we see in figure 2.8) of the rupture front depends heavily on the pre-stress ratio inside and outside the asperity. The greater this ratio is, the greater the focusing effect is, and conversely, the the lower the pre-stress ratio is the less constrained rupture directivity becomes. This would imply for cases where pre-stress outside of an asperity is relatively smooth and insignificant, the width of a pulse could be defined by the time it reaches the edge of the breaking asperity. However the possibility of such a slip distribution occurring naturally are quite low.

The trend we see in figure 2.8 is present over a range of asperity sizes for a

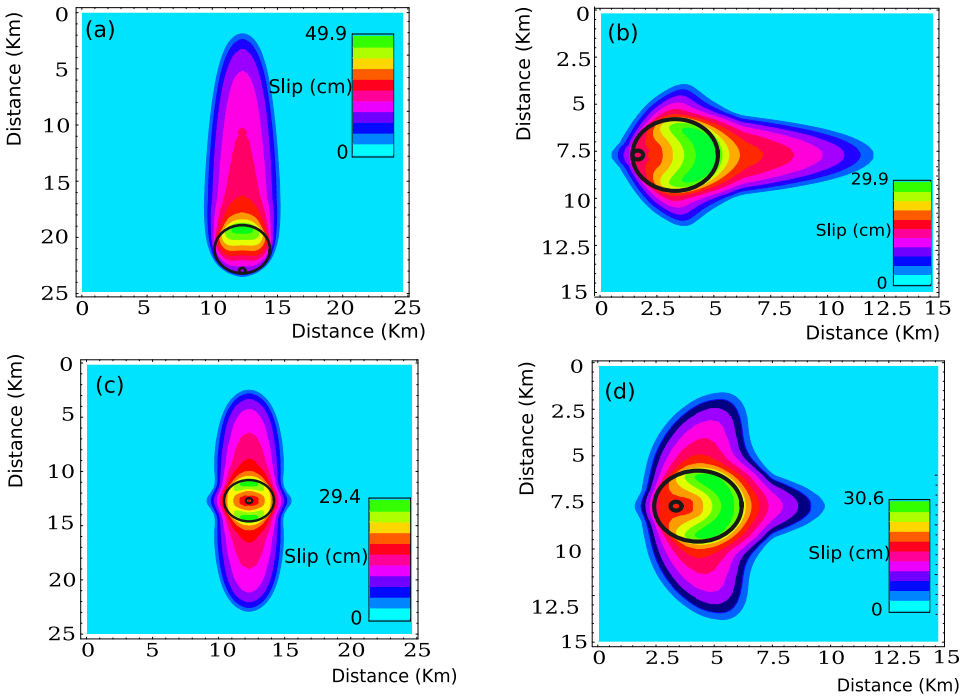

Figure 2.8: The total slip for a variety of dynamic rupture models with whereby the trigger zone is moved around inside of the asperity. In models a,b and c we can see that the asperities size directly influences the overall rupture front.

given trigger position pointing to possible determinism in fracture mechanics. Figure 2.9 shows the the total slip on the fault for a variety of asperity sizes while all other parameters remain constant (i.e pre-stress values) and the trigger patch remains on the bottom side of the asperity. The range in asperity size whereby rupture is controlled primarily by the asperity is limited. In the case of figure 2.9 for example, rupture will not propagate outside of the asperity for asperities with radii small than 1km. There is also an upper limit to the size of an asperity after which the asperity's effect on final rupture diminishes. Figure 2.9(c) is an example of this case in question, whereby the rupture front fans out in size. In fact the rupture was still rupturing when the model stopped. This change in fracture type from a self healing pulse which naturally dies out to one of a stable pulse is dependent on the asperity. In figure 2.9 this occurred at a radius of 2.3km, however this size changes for different pre-stress values.

Turning our attention to the moment rate, a detectable feature on the seismogram, again we see this same saturation of the asperity's influence once it grows bigger than a certain size. Figure 2.10 plots the evolution of the moment rate with time for a variety of asperity sizes using a fixed trigger patch location. The difference between Figures 2.10(a) and (b) is the location of the trigger patch (i.e. the trigger patch is moved from the left edge to the bottom edge of the asperity) as well as slightly different pre-stress outside of the asperity. In both cases the maximum moment rate occurs at the edge of the asperity when a homogeneous pre-stress is applied outside of the asperity (this is also true for trigger patches in the centre of the asperity). In both sets of results the peak moment increases with asperity size before decreasing slowly. When the asperity reaches a size of $\approx$2.3km the moment rate decreases just outside the asperity but then increases again as it becomes unstoppable. Clearly there is maximum size over which the fracture front gains enough elastodynamic energy to rupture indefinitely.

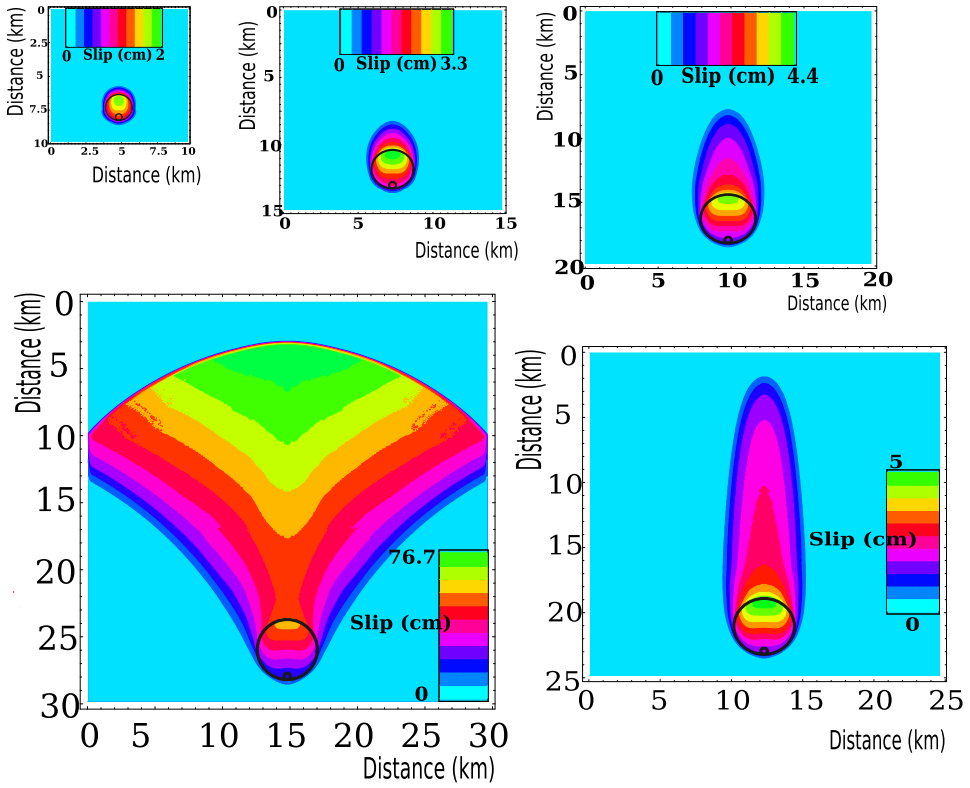

Figure 2.9: A selection final slip distribution results whereby the only parameter that varies between models is the asperity size. The radius of the asperity increases from 1.5km to 2.5km going form model a to e. In all cases rupture stop naturally inside the model space except for model (e) which was still rupturing up until the model stopped running.

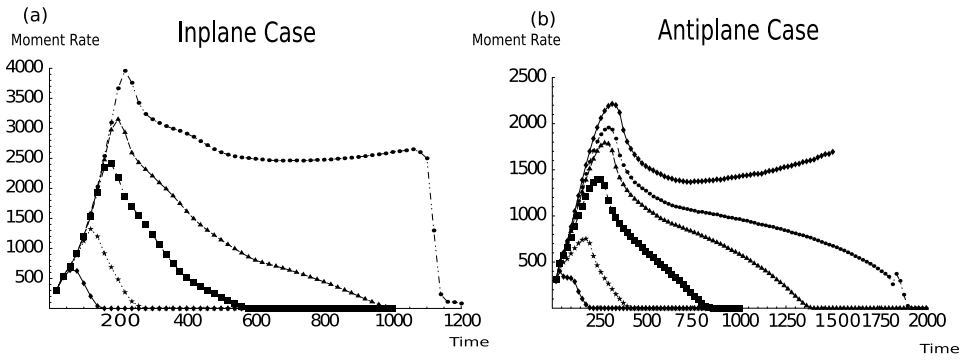

Figure 2.10: The evolution of the moment rate with time. The difference between the two graphs is that rupture nucleated on the left edge of the asperity in graph (a) and on the bottom edge in graph (b). The different curves in each graph are due to the changing size of the asperity, for both sets of graphs the asperity size is increased up to the point where rupture does not terminate inside of the asperity (the highest line in each case). The shaded area in both plots highlights the technique used to calculate the total moment of earthquake - i.e. the area under the graph. Note all units in this case are non-dimensional.

Interestingly, these moment rate functions have a similar appearance to those produced using the Sato-Hirasawa kinematic model (i.e. comparing figure 2.10 with 2.11. This model has been used as a possible explanation for why early magnitude estimation is possible (Kanamori [2005]). However, in the case our dynamic modelling, it is possible that such a kinematic model is valid over a limited range (i.e. 1.5M – see figure 2.12 and future discussions).

In figure 2.12 we plot the log of the maximum moment rate inside the asperity against the final magnitude outside of the asperity. Data points from large asperities which exhibit saturation effects have been excluded as the final magnitude for these models is proportional to run time of the model.

However, we have hypothetically extrapolated the best fit curves (denoted by dashed lines) to show the saturation effect whereby the best fit curves move to an asymptotic maximum moment rate as the final moment becomes infinite.

The data points in figure 2.12 have been split up into three groups which relate to the trigger position. Circles denote results for when the trigger is in the centre of the asperity, for squares the trigger is on the top edge the asperity, and for stars the trigger is on the left edge of the asperity.

For all three cases there exists a linear trend between the base 10 logarithm of the maximum moment rate and final magnitude outside of the asperity. However this scaling is limited in magnitude range (i.e. $\approx 1.3 M_L$) due to the change in the nature of the fracture (i.e. from self healing pulse to stable pulse). As this is a theoretical model we can vary the nodal distance in our model to increase the asperity size and thus the final magnitude produced (see Table 2.4) but this does not change the range of the linear relationship seen in figure 2.12.

Examining figure 2.12 we can see that the linear scaling for the three different trigger locations are very similar to each other. There is some small variation between the linear trends with the slip of the best fit line varying between 0.49 and 0.63 (see Table 2.1). This difference which is due to the different trigger locations and pre-stress distributions. An analogous comparison could be the variety of stress regimes that earthquakes are found under (e.g. interplate or intraplate earthquakes). This could be a possible explanation for a small portion of the larger scatter seen observationally (e.g. Olson and Allen [2005] and Zollo et al. [2006]). However as our linear scaling holds over a small magnitude range this would point to rupture being deterministic only over a short period.

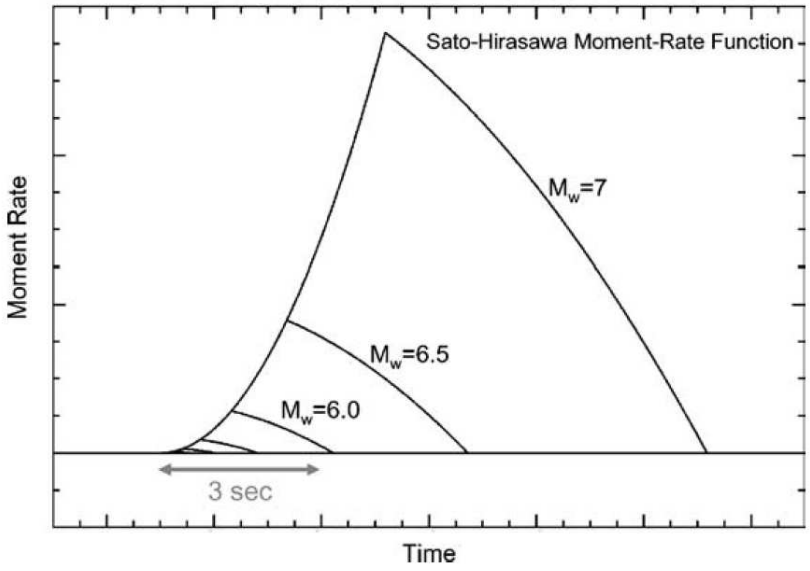

Figure 2.11: The application of the Sato-Hirasawa kinematic model (REF) in calculating the moment rate for a given station at a polar angel of 90^o. Source variables used are: p-wave speed 6km/s, s-wave speed 3.5 km/s, density=2.7 g/cm^3, rupture velocity 2.5km/s and applied shear stress 30bars. Taken from Kanamori [2005]

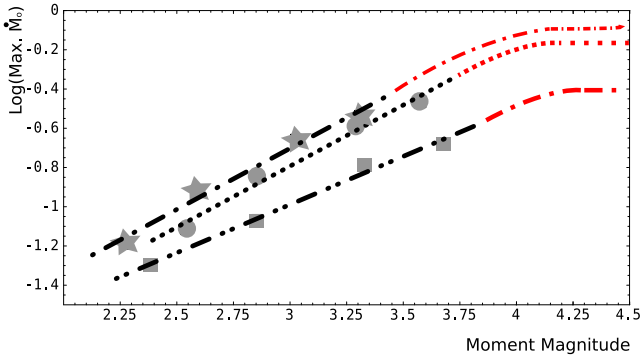

Figure 2.12: Plotting the maximum magnitude rate against the final moment magnitude. The results for three different trigger locations are plotted, the circles refer to when the trigger is on the left side of the asperity, the squares for the trigger being at the top edge of the asperity and the stars for when the trigger is at the centre of the asperity. For each set of results only the outer size of the asperity was increased. In the case where the trigger is at the centre of the asperity the slip and rate weakening friction law was applied.

Table 2.1: List of parameters for fitting a best linear line to function data-points in figure 2.12. Best fit curve is defined as $\log_{10}(\dot{M}_o)$ =mM_L+c, where m is the slope and c is the y-intercept.

	m	c
Antiplane Case	0.49	-2.46
Inplane Case	0.62	-2.66
Centre Case	0.62	-2.57

2.6.4 Random Pre-stress outside of the Asperity

Power Law Distribution

Next we shall place the high stress asperity used in the previous dynamic models into a fault with a heterogeneous pre-stress distribution. In creating a random pre-stress distribution we want to produce rupture on a fault that is somewhat realistic.

Andrews [1980] noted that by assuming that the amplitude spectra radiated by an earthquake is a self similar power law function (as observed by Aki [1967]), a stochastic slip and static stress drop distribution for a fault plane can be defined in the frequency domain. Assuming that the average stress drop is independent of the earthquake's size, the scaling between stress drop and wavenumber has a power law of -1.Subsequently Herrero and Bernard [1994] noted that the stress drop spectrum on a fault plane can be defined as a function of the radial wave number k:

$$\Delta\sigma_L(k) = \overline{\Delta\sigma}\frac{L}{k} \tag{2.42}$$

where $\overline{\Delta\sigma}$ is the average stress drop and L is the ruptured length. Equation 2.42 applies only for $k > 1/L$, for wavenumbers below this (i.e. $k < 1/L$) the stress drop spectrum is proportional to k thus the average stress is zero for $k = 0$. Figure 2.13 denotes the stress drop spectrum of a generic fault in the wavenumber domain.

Therefore by predefining a wavenumber range, a rupture length and an average stress drop equation 2.42 can generate a random pre-stress spectra. $\overline{\Delta\sigma}(k)$ can then be converted into the time domain by Fourier transform in order to generate a stochastic pre-stress distribution for a fault plane. For the heterogeneous prestress distribution used in figure 2.14 a wave number range of 0-0.2m^{-1} was used, where by L was defined by the grid size (i.e. 400 nodes).

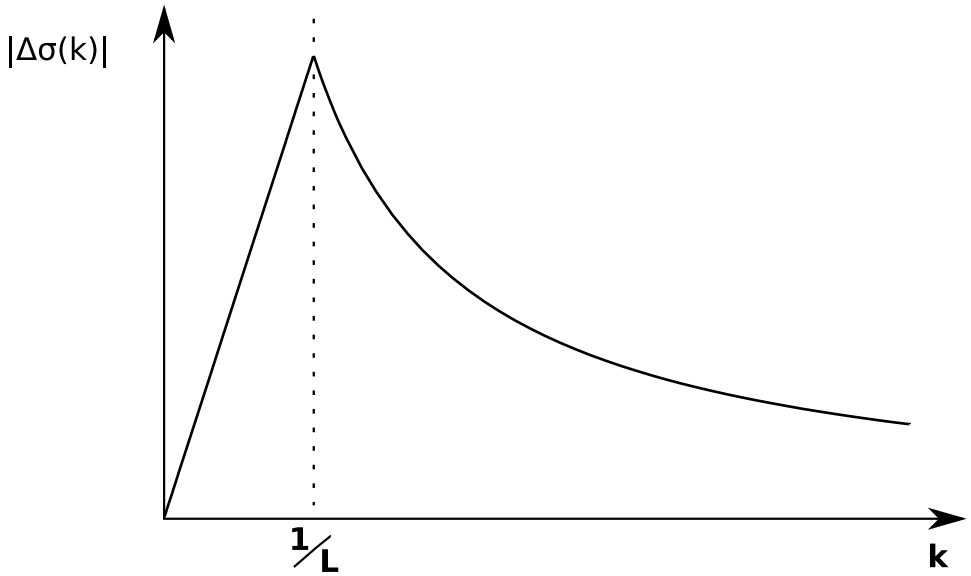

Figure 2.13: This is a schematic representation of of the stress drop (i.e. $\Delta\sigma$) in the wavenumber domain as proposed by Herrero and Bernard [1994].For $k <$ Ł-1, where L is the length of the fault and k the wavenumber, the stress drop scales with the wavenumber, while for $k > L^{-1}$ the stress drop is define by equation 2.42

Inhomogeneous background stress

In figure 2.14 we now introduce a heterogeneous pre-stress outside of the asperity. The trigger patch is placed at the edge of the asperity as it produced a very distinctive constraint on rupture propagation (as seen in figure 2.9). The initial directivity imposed by the nucleation's location can still be seen, however this has now been mixed with constraints imposed by pre-stress features outside of the asperity. Noticeably, the lateral edges of the asperity are sensitive to local pre-stress levels contracting and expanding depending on whether the pre-stress is his high or low in these regions. This feature is heavily dependant on the pre-stress range, with larger fluctuations occurring when a larger pre-stress range is used.

Indeed, rupture termination is also heavily effected by the pre-stress outside of the asperity. Figure 2.14 shows two models both using the same initial parameters with the only difference between the two being that the pre-stress outside of the asperity is the inverse of the other (i.e. areas of high stress become low stress as we look from one model to the other, and vica versa). In figure 2.14(a) rupture terminates just outside of the asperity due to a patch of low pre-stress, while in figure 2.14(b) rupture continues to propagate indefinitely (in fact rupture was still propagating when the model stopped). As the size and pre-stress inside of the asperity remains constant between the two models we can say that the initial elastodynamic energy is the same and therefore rupture termination is cascade in nature.

2.7 Remarks on the dynamic results

Interestingly, the offset of large slip from the hypo-centre position seen in figure 2.9 is a feature that has been observed in kinematic models too (Mai Mai et al. [2005]). In our models we can explain this offset due to edge of

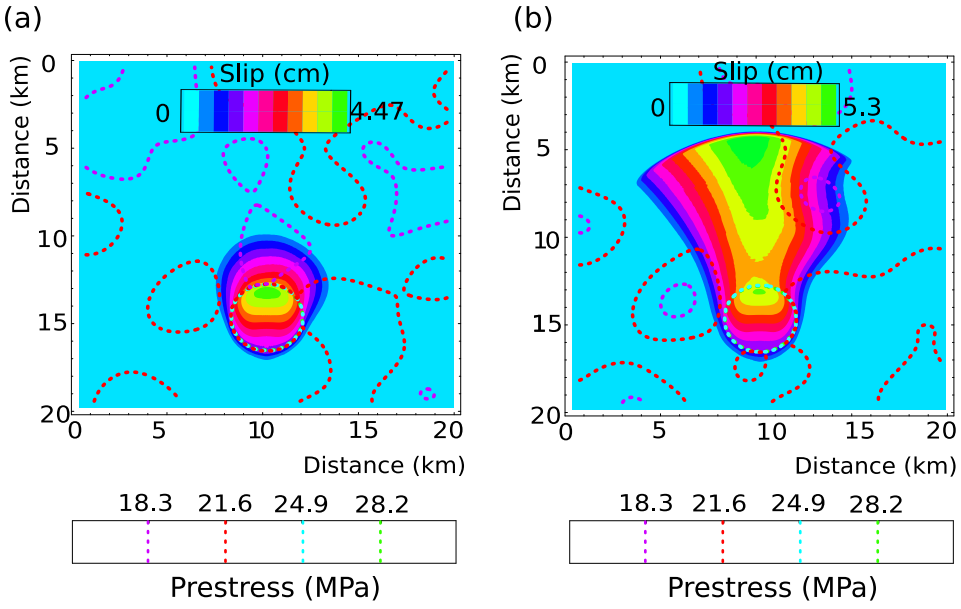

Figure 2.14: For model (a) and (b) an asperity is surrounded by a randomly distributed pre-stress. For both figures the asperity size and location of the trigger patch is identical. However, the background pre-stress varies between the two figures, but both have the same pre-stress range and mean value. Therefore while our breakout phase is constant between the two models the results vary greatly with model (a) stopping just outside of the asperity while in model (b) rupture is continuing to rupture at the end of the dynamic model run time. This points to the view that, while the breakout phase does impose some deterministic characteristics (i.e. note that rupture direction is the same in both models) the termination of fracture is predominantly cascade nature. Asperity has a radius of 2km whilst the wavenumber range used to create the background pre-stress was 0-0.2m^{-1}

the high stress asperity. Inside of the asperity the energy flux is constantly increasing and with it the slip. Outside of the asperity the pre-stress is lower and so the energy flux decreases and so too does the amount of slip. This correlation between dynamic and kinematic models could imply that hypocentres are naturally found in or very near high stress asperities. Indeed Andrews [1976b] critical length for cracks would support this point of view.

However, while a rupture pulse requires a certain size asperity in order to rupture meaningful distances, we have shown by figure 2.14 that their termination is heavily dependent on local conditions on the fault. By using a rate friction law to create a manageable fracture pulses we aimed to create a rupture with some deterministic features. These features proved to exist over a limited magnitude range under specific conditions. The exception to this is rupture directivity which is heavily dependent on trigger location inside the asperity. Even with a random pre-stress distribution surrounding an asperity (figure 2.14) this is still an overall feature of rupture. Indeed, relative position of nucleation to high stress asperities could be an explanation for the observed predominance of uni-directional rupture propagation in large earthquake (McGuire et al. [2002]).

Whilst rupture directivity provides rupture nucleation with some control of overall rupture direction, it does not influence termination and hence, deterministic scaling is limited to a small magnitude range for pulse ruptures. Other friction laws may also provide similar scaling results but probably over shorter ranges. The widely used crack model has also been shown to demonstrate scaling features between stress drop and final rupture size (Ripperger et al. [2006]) but again over a short range of values.

Therefore there may exist a deterministic scaling, however it is limited to a short magnitude range and cannot properly explain the seismological observations of Allen and Kanamori [2003], Olson and Allen [2005] , Wu and Zhao [2006] or Zollo et al. [2006]. Given the limitations that our deterministic

hypothesis has provided we will now look at our kinematic one.

2.A Appendix

2.A.1 FD technique and theory

Elastodynamic Equations

Whilst the second order partial differential elastodynamic equation (equation 2.14) determines the evolution of displacement for a given stress field it does provide some inherent problems when evalutated numerically. Madariaga [1976] noted that as the slip rate is required in the calculation of the rate friction law and is used in calculating far field particle displacment, it would be the more natural variable to solve the elastodynamic equations for. By using the displacement (see equation 2.14) requires the calculation of it's derivative in order to define the slip rate – a procedure that increases the model run time but more importantly decreases model accuracy.

Secondly, Madariaga [1976] split the three 2^{nd} order partial differential equations into the more practical set of nine first order hyperbolic partial differential equations (three velocity and six stress equations). Therefore the elastodynamic equations of motion can be re-written as:

$$\rho \dot{v}_i = \sigma_{ij,j} \tag{2.43}$$

$$\dot{\sigma}_{ij} = \lambda v_{k,k} \delta_{ij} + \mu (v_{i,j} + v_{j,i}) \tag{2.44}$$

where v is the sliprate, dots denote time derivatives and commas partial derivatives and σ is the stress. Einstein summation is assumed. This method removes the unnecessary calculation of the displacement derivative on the fault thus increasing the accuracy of any numerical methods that are applied. However, as there are now two sets of coupled partial differential equations with both both stress and velocity are interdependent. This requires that finite difference grid must be modified somewhat to accommodate the coupled equations. Therefore the grid is staggered whereby the nodes that define the

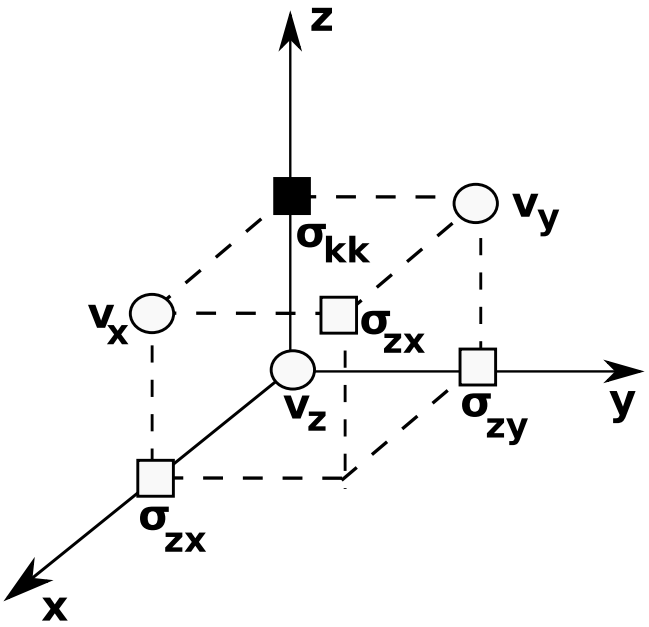

Figure 2.15: A schematic depicting the positioning of the staggered stress (denoted by σ_{ij}, where i, j indicate tensor component) and velocity (i.e. v_i, which is the particle velocity in the i^{th} direction) nodes for a 3 dimensional grid as defined by Madariaga et al. [1998]

velocity and stress are separated by half a grid space thus providing a pseudo independence. As both temporal and spatial partial derivatives are present in equation 2.43 the grid is staggered in time as well as space. Madariaga [1976] first applied this staggered grid system in 2D, it was later extended to 3D (Virieux and Madariaga [1982], Madariaga et al. [1998]) as computational resources increased (figure 2.15 highlights the separation of elastodynamic variables in a 3 dimensional grid).

FD Theory

A finite difference technique can now be used to evaluate the our new elastodynamic equations (equation 2.43). Finite difference method discretises the model medium spatially and temporally by means of Taylors series expansion. The finite difference method uses the following two expansions of a function to calculate both spatial and temporal derivatives:

$$f(x+h) = f(x) + hf'(x) + \frac{h^2}{2!}f''(x) + \frac{h^3}{3!}f'''(x) + O(h^4) \quad (2.45)$$

$$f(x-h) = f(x) - hf'(x) + \frac{h^2}{2!}f''(x) - \frac{h^3}{3!}f'''(x) + O(h^4) \quad (2.46)$$

Where h is the step size (be it spatial or temporal) and f is the function being evaluated, f' is the derivative of $f(x)$ and $O(h^4)$ denotes an error of the 4^{th} order (i.e. the error is a function of h^4).

For the spatial derivative we shall use the central difference approach whereby taking one equation away from the other in equation 2.45 givens the spatial derivative for $f(x)$ as:

$$f'(x) = \frac{9}{16h}\{f(x+h) - f(x-h)\} - \frac{1}{48h}\{f(x+3h) - f(x-3h)\} \quad (2.47)$$

h is the step size between nodal points and contains a 4th order error based on the step size. For the time derivative in the elastodynamic equations 2.43 the backward difference technique is applied:

$$f'(t) = \frac{f(t) - f(t-h)}{h} \quad (2.48)$$

This provides an error in the region of the 2^{nd} order of the time step (i.e. $O(h^2)$).

Finite Difference Applied to Elastodynamic Equations

Equations 2.48 and 2.47 can now be subsituted in to equation 2.43 thus converting the elastodynamic equations into a discrete system.

Equation 2.48 can be re-written in terms of $\mathbf{V}^n_{k,l,m}$, a three component vector (i.e.$\mathbf{V} = (v_x, v_y, v_z)$), which defines the discrete slip rate at time n and grid position $(k\,l\,m)$:

$$D_t \mathbf{V}^n_{k,l,m} = \frac{\mathbf{V}^n_{k,l,m} - \mathbf{V}^{n-1}_{k,l,m}}{\Delta t} \tag{2.49}$$

Δt is the time step. Likewise the $f(x)$ in equation 2.47 can be replaced by the discrete stress vector, $\mathbf{\Sigma}^n_{k,l,m}$, which defines the stress for grid position $(k\,l\,m)$ and time n and contains six components (i.e. $\mathbf{\Sigma} = (\sigma_{xx}, \sigma_{yy}, \sigma_{zz}, \sigma_{xy}, \sigma_{xz}, \sigma_{yz})$). We can now re-write the nine elastodynamic equations (equation 2.43) as:

$$\begin{aligned}
D_x \mathbf{\Sigma}^n_{k,l,m} &= \frac{9}{16\,\Delta x}(\mathbf{\Sigma}^n_{k+1,l,m} - \mathbf{\Sigma}^n_{k-1,l,m}) + \frac{1}{48\,\Delta x}(\mathbf{\Sigma}^n_{k+3,l,m} - \mathbf{\Sigma}^n_{k-3,l,m}) \\
D_y \mathbf{\Sigma}^n_{k,l,m} &= \frac{9}{16\,\Delta y}(\mathbf{\Sigma}^n_{k,l+1,m} - \mathbf{\Sigma}^n_{k,l-1,m}) + \frac{1}{48\,\Delta z}(\mathbf{\Sigma}^n_{k,l+3,m} - \mathbf{\Sigma}^n_{k,l-3,m}) \\
D_z \mathbf{\Sigma}^n_{k,l,m} &= \frac{9}{16\,\Delta z}(\mathbf{\Sigma}^n_{k,l,m+1} - \mathbf{\Sigma}^n_{k,l,m-1}) + \frac{1}{48\,\Delta x}(\mathbf{\Sigma}^n_{k,l,m+3} - \mathbf{\Sigma}^n_{k,l,m-3})
\end{aligned} \tag{2.50}$$

where $\Delta x, \Delta y, \Delta z$ are the nodal spacing in the x, y, and z directions repectively in our discrete model. Σ is the discrete value of stress of an unspecified conpoment at time n and position (k, l, m).

Therefore equation 2.43 can now be rewritten in terms of discrete opera-

tors:

$$\begin{aligned}
\rho D_t v_x &= D_x\sigma_{xx} + D_y\sigma_{xy} + D_z\sigma_{xz} \\
\rho D_t v_y &= D_x\sigma_{yx} + D_y\sigma_{yy} + D_z\sigma_{yz} \\
\rho D_t v_z &= D_x\sigma_{zx} + D_y\sigma_{zz} + D_z\sigma_{zz} \\
D_t\sigma_{xx} &= (\lambda + 2\mu)D_x\, v_x + \lambda\,(D_y\, v_y + D_z\, v_z) \\
D_t\sigma_{yy} &= (\lambda + 2\mu)D_y\, v_y + \lambda\,(D_x\, v_x + D_z\, v_z) \\
D_t\sigma_{zz} &= (\lambda + 2\mu)D_z\, v_z + \lambda\,(D_y\, v_y + D_x\, v_x) \\
D_t\sigma_{xy} &= \mu\,(D_y\, v_x + D_x\, v_y) \\
D_t\sigma_{yz} &= \mu\,(D_z\, v_y + D_y\, v_z) \\
D_t\sigma_{xz} &= \mu\,(D_z\, v_x + D_x\, v_z)
\end{aligned} \tag{2.51}$$

where $x\,y\,z$ relate to the component of the stress tensor or slip rate and not the relative position in the grid. The separation of both time and space derivatives in equations 2.43 means that these derivative can be calculated at separate grid positions leading to the use of a staggered finite difference grid in both time and space. Defining Δt as the the grid spacing, the time grid is defined with sliprate positioned at every $n\Delta t$ and stress placed at $(n + \frac{1}{2})\Delta t$. For the spatial grid, assuming that grid spacing is equal between nodes, we can say:

$$\Delta x = \Delta y = \Delta z = \frac{\Delta h}{2} \tag{2.52}$$

where Δh is the overall grid spacing in the staggered grid, whilst $\Delta x, \Delta y, \Delta z$ denote the the spacing between two nodes of the same parameter in the x,y and z direction respectively.

The grid distribution relative to the fault plane position can be applied in a multitude of ways. Initially Virieux and Madariaga [1982] proposed placing the fault plane on the same nodes as the shear stress components and used symmetry about the fault plane to solve the elastodynamic equations.

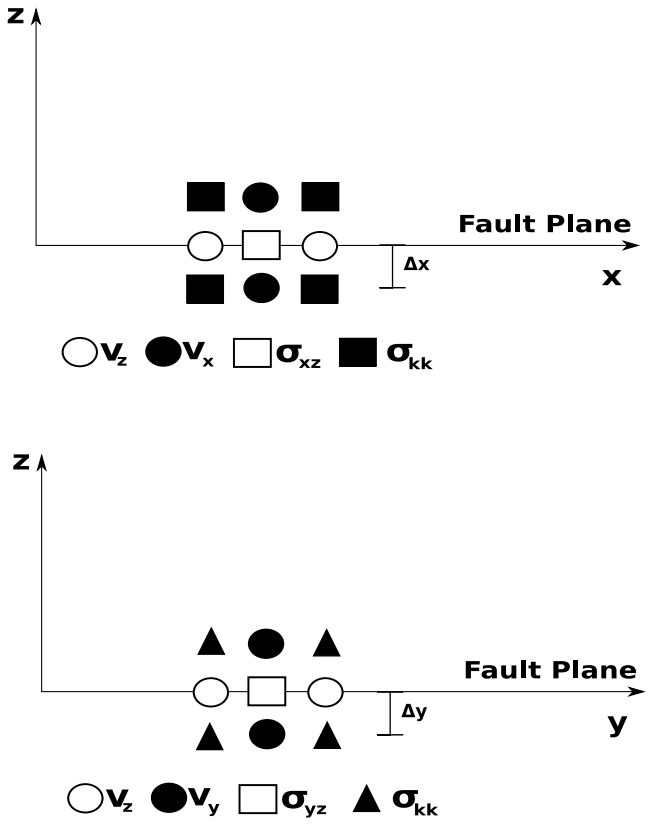

Figure 2.16: A schematic depicting the positioning of the staggered nodes on the fault plane.

However, as noted by Madariaga et al. [1998] this produced numerical inaccuracy near the crack tip, as a consequence Madariaga et al. [1998] defined a two-grid-row "thick" fault zone. This method places the antisymetric variables on the fault zone (i.e. the shear velocity and normal stress) and the symmetric variables one grid node off it (the shear stress relative to the fault plane and normal velocity). However, this technique does not calculate the shear stress on the fault plane but rather one grid space off it (i.e. Δz) whilst the normal stress and shear velocity are calculated two grid positions away from the fault. This leads to a dependence on choice of the critical slip D_c relative to the grid spacing a feature noted by Madariaga et al. [1998]. Our choice of fault position, however shall produce a D_c that is indepentent of the grid spacing.

By placing the fault plane along the shear componets of stress (see figure 2.16) grid scaling problems are removed. The shear stress nodes (e.g. σ_{xz} and σ_{yz} – in the case of figure 2.16) are now now calculated on the fault plane. The slip rate, in the case of a homogeneous medium either side of the fault (i.e. in chapter 2) is calculated as:

$$\dot{\mathbf{D}}(x, y, nzf) = 2\,\mathbf{v}(x, y, nzf + \Delta z) \tag{2.53}$$

whereby the fault plane is defined along the z-axis (see figure 2.16) at position nzf. In the case of bi-material fault surface the slip rate is interpolated across the surface using the equation:

$$\dot{\mathbf{D}}(x, y, nzf) = \mathbf{v}(x, y, nzf + \Delta z) - \mathbf{v}(x, y, nzf - \Delta z) \tag{2.54}$$

The integral of either equations 2.53 or 2.54 shall give the slip. The normal stress nodes (i.e. σ_{zz}) are also defined one half nodal grid space off the fault plane (i.e. $\Delta z/2$) and are thus interpolated like the slip rate using equation 2.54.

As the stress component normal to the fault plane is an odd function we shall assume that its model reference state zero on the fault plane with no

temporal fluctuations (i.e. $\sigma_{zz}^{+} = \sigma_{zz}^{-}$). This assumption is valid when fault material is homogeneous on either side of the fault but untrue for bi-materials (Andrews and Ben-Zion [1997]and Ben-Zion and Andrews [1998]). This grid layout reduces computational error and time as the shear stress is computed on the fault plane and thus requires no interpolation.

Model Constraints

In order that the finite difference technique is stable the ratio of grid spacing to time step must be greater than the Courant-Friedrics-Levy (CFL) Constant. Virieux [1986] defined the CFL constant for a homogeneous staggered grid system as:

$$\alpha < \frac{\Delta x}{\Delta t \sqrt{n}} \tag{2.55}$$

where n is the number of dimensions in the model (which shall be set to 3 of 3D rupture simulations), Δt is the time step, Δx is the spacing between the nodes and (α) is the maximum (in the case of a hetergeneous media) p-wave velocity generated in the model. As the p-wave velocity is defined as:

$$\alpha = \sqrt{\frac{\lambda + 2\mu}{\rho}} \tag{2.56}$$

with λ and μ representing the Lame constants of the media and ρ denoting the density of the medium.

Another constraint on nodal spacing is wave dispersion. A general rule of thumb (Virieux [1986]) is that:

$$\Lambda_{min} > 10\, dx \tag{2.57}$$

where Λ_{min} is the minimum wavelength visible in the model below which wavelengths are generally undistinguishable from numerical noise. As the s-wave have larger wavelengths than p-waves, it will be the restrictive wave type in determining this condition.

2.A.2 Applying mirror boundaries to fault planes

In order to apply a mirror boundary condition to a fault plane the symmetry in the stress components of the stress tensor and the particle velocities must be maintained. In a 3D media, two boundaries shall border the fault plane whilst the third shall constitute the lower half of the fault plane. The assumption being that the elasto-dynamic parameters (i.e. the Lame Constants, pre-stress) are identical either side of the fault and the fault plane is planar. Fault symmetry dictates that the shear stress components for the traction vector for a given surface are even functions. The normal stress components and the shear stress component perpendicular to a defined surface on the other hand are odd functions. This variation in symmetry conditions for different surfaces relative to the fault plane means that each mirror boundary must be individually defined.

Assuming that the fault plane is along the z-axis, the three mirror boundaries can be defined using both the Dirichlet and Neumann boundary conditions as follows. With the superscript m denotes the stress component that is in the mirror boundary the x-z mirror boundary is defined as:

$$\begin{aligned} \sigma_{xx} &= \sigma^m_{xx} \quad \sigma_{xy} = -\sigma^m_{xy} \\ \sigma_{yy} &= \sigma^m_{yy} \quad \sigma_{yz} = \sigma^m_{yz} \\ \sigma_{zz} &= \sigma^m_{zz} \quad \sigma_{xz} = -\sigma^m_{xz} \end{aligned}$$

with the velocity components defined as:

$$\begin{aligned} v_x &= v^m_x \\ v_y &= -v^m_y \\ v_z &= v^m_z \end{aligned}$$

On the y-z mirror boundary is denoted by:

$$\begin{aligned} \sigma_{xx} &= -\sigma^m_{xx} \quad \sigma_{xy} = \sigma^m_{xy} \\ \sigma_{yy} &= -\sigma^m_{yy} \quad \sigma_{yz} = -\sigma^m_{yz} \\ \sigma_{zz} &= -\sigma^m_{zz} \quad \sigma_{xz} = \sigma^m_{xz} \end{aligned}$$

$$\begin{aligned} v_x &= v^m_x \\ v_y &= -v^m_y \\ v_z &= -v^m_z \end{aligned}$$

Finally, the mirror boundary for one side of the fault plane (i.e. the x-y plane) is:

$$\begin{aligned} \sigma_{xx} &= -\sigma^m_{xx} \quad \sigma_{xy} = -\sigma^m_{xy} \\ \sigma_{yy} &= -\sigma^m_{yy} \quad \sigma_{yz} = \sigma^m_{yz} \\ \sigma_{zz} &= -\sigma^m_{zz} \quad \sigma_{xz} = \sigma^m_{xz} \end{aligned}$$

$$\begin{aligned} v_x &= -v^m_x \\ v_y &= -v^m_y \\ v_z &= v^m_z \end{aligned}$$

In order to view the displacment for example, on the full fault plane where there are mirror boundaries present, the displacement matrix needs to be manipulated. Therefore assuming that A is the n x m displacement matrix mirror images can be created using the following matrix operations:

$$A_I : A_{i,j} \rightarrow A_{i,m-j}$$
$$A_{II} : A_{i,j} \rightarrow A_{n-i,j}$$
$$A_{III} : A_{i,j} \rightarrow A_{n-i,m-j}$$

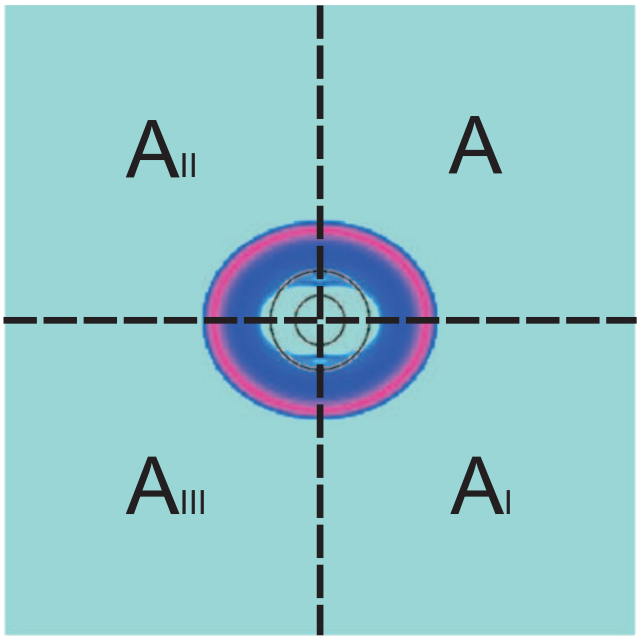

Figure 2.17: For this figure the model space only consisted of the top righthand quadrant with the black dotted line bordering the top right quadrant representing mirror boundaries. It should be noted that this can not be used when trigger patch is moved from the centre of the asperity as pre-stress symmetry breaks down.

where A_I is the slip matrix when i^{th} is the mirror plane, and A_{II} where j^{th} denotes the mirror axis. A_{III} is symmetric representation of matrix A through the origin. i and j are matrix elements and n and m being the largest element of the matrix. Figure 2.17 depicts the different slip matrices for the different quadrants of the image.

2.A.3 Parameter Tables used in Numerical Models

Table 2.2: Variables used in numerical modelling whose results are defined in figures 2.8, 2.9, 2.10, 2.12 and 2.14. Fracture parameters as well as material variables have been define

Model Parameters	
Characteristic Length:δ	3
Characteristic Velocity:v_m	0.025
Static Friction: μ_s	0.3
Dynamic Friction: μ_d	0.1
Spatial Step: dx	0.4
Time step: dt	0.1
Yield Stress: τ_y	1
Density: ρ	1
Shear Modulus: μ	1
Bulk Modulus: λ	1

Table 2.3: Pre-stress distribution used for points making up graph 2.7. In all cases the yield stress is set at 1, and the pre-stress in the trigger patch is 1.2. The pre-stress outside of the asperity (i.e σ_B) is set to 0.3 in all cases. Note all units in this case are non-dimensional.

Symbol: ★	r_A: 60		r_T: 15	
σ_A:	0.6	0.7	0.8	0.9

Symbol: ♦	r_T: 16		σ_A: 0.8	
r_A:	60	70	80	90

Symbol: ■	r_A: 60				r_T: 15					
σ_A:	0.3	0.5	0.6	0.7	0.77	0.78	0.789	0.79	0.9	0.95

Table 2.4: Scaling of the theoretical models. Dx is the arbitrary discrete step between grid nodes, Λ refers to the resulting radius of the high-stress asperity and M_L is the scaled magnitude from the simulation outcome. Anti-plane edge, In-plane edge and Center refer to the position of trigger inside the high-stress asperity (see figure 2.5 for a definition of the three cases). The background pre-stress levels were 19.5 MPa and 22.5 MPa for the antiplane and inplane fault models respectively. In both cases the pre-stress inside the asperity was set to 28.5 MPa. For the case where the trigger is located in the centre of the asperity, the background pre-stress was set to 9 MPa and asperity's pre-stress was set to 24 MPa. For the hetergeneous pre-stress, the apserity has a stress of 28.5 MPa , whilst the random pre-stress was spread over a stress range of 15 - 27 MPa afterwhich the stress distribution was truncated for stresses greater than 24 MPa. Yield stress is 30 MPa and shear stiffness is 1 GPa for all cases.

		Dx (m)		
Trigger:		10	20	50
Antiplane edge	Λ(Km)	0.75-1.10	1.50-2.30	4.10-6.10
	M_L	1.78-3.07	2.38-3.68	3.18-4-47
Inplane edge	Λ(Km)	0.75-1.10	1.5-2.30	4.10-6.10
	M_L	1.94-2.97	2.54-3.57	3.34-4-37
Center	Λ(Km)	1.50-2.25	3.00-4.50	7.50-11.25
	M_L	1.67-2.70	2.28-3.30	3.07-4-10

Chapter 3

Kinematic Modelling

3.1 Introduction

Dynamic modelling, discussed in Chapter 2 involves the study of earthquake rupture based on the stresses, frictional and geometrical properties of the fault plane, thus providing a complete vision of the physical processes in the near field. Kinematic modelling on the other hand, provides a simpler and more efficient method capable of determining radiation at an arbitrary position for a prescribed history of slip on the fault plane and defined velocity profile in the surrounding medium. In order to investigate the rupture process for a given earthquake, broad assumptions are made about the fault (e.g. – fault size, focal mechanism) and the surrounding media (i.e. seismic velocity profile).

Generally it is the dislocation theorem or representation theorem that is used in kinematic modelling. Equation 3.1 is an example of a simplified dislocation theorem (defined by Madariaga and Olsen [2002]) whereby particle displacement recorded at time t and location $\mathbf{x}$ is:

$$u(\mathbf{x},t) = \int_0^t \int_{S_\xi} \Delta u(\xi,\tau) G(\mathbf{x}-\xi, t-\tau) d\xi d\tau \tag{3.1}$$

The slip Δu is a function of space and time on the fault whilst G represents the Green's tensor for a ray that departed spatial position ξ on the fault at time τ and arrived at position $\mathbf{x}$ at time t. S_ξ defines some surface on the fault plane. Basically, equation 3.1 highlights ground motions dependence on both source features and the velocity profile of the media between the fault and the seismic station.

Normally, in kinematic modelling, the ground motion for a given time and place is known (i.e. $u(\mathbf{x}, t)$) and so equation 3.1 is inverted and solved for the slip history ($\Delta u(\xi, \tau)$). In order to examine variations in slip across the fault, the fault plane is discretized with slip functions defined for each cell on the fault plane. The resultant ground motion is then computed and compared with data recorded at stations in time (Hartzell and Heaton [1983]) or the frequency domain (Cotton and Campillo [1995]). Geodetic data can also been incorporated into the kinematic inversion REFERENCE thus increasing accuracy.

Whilst variations in slip amplitude are linear in equation 3.1, rupture propagation is highly non-linear thus making the inversion problem non-linear (Madariaga and Olsen [2002]). Whilst non-linear inversions are now possible (Emolo and Zollo [2005] and Peyrat and Olsen [2004]) they are very computer intensive techniques. Other solutions to this problem include assuming a constant rupture velocity (Hartzell and Heaton [1983]) or through *linearisation* of the inverse problem (Gubbins [2004]). The advantage of such techniques have over non-linear inversions is that they are computationally quicker although not as accurate.

In terms of the Green's function, a simplified velocity profile is generally assumed and it's effect is determined using finite difference (Graves [1996], Graves and Wald [2004]), discrete wave number modelling (Bouchon [1981]) or ray theory (Brokesova [2006]). The technique used varies on whether low (i.e. finite difference or discrete wave number modelling) or high (ray theory)

frequency ground motion is of interest.

However in our circumstance we do want to invert specific seismic data for a prescribed earthquake but rather look at the effect that kinematic parameters have on to early magnitude estimation. In particular we are interested in looking at the relationship between the first few seconds of ground motion recorded by a group of seismic stations and kinematic features on the fault plane. As with our dynamic rupture modelling, we need to define an examinable kinematic parameter which is relevant to early magnitude detection. The concept of isochrones (proposed by Bernard and Madariaga [1984] and Spudich and Frazer [1984]) provides such a parameter as it links particle motion at given seismic stations to the kinematics of source process on the fault. This simplified kinematic model allows us to estimate the far field motion amplitudes for a large number of simulated sources and random station positions. As a consequence, we can investigate the influence kinematic parameters have on the scaling between far field displacement and source magnitude by producing synthetic catalogues of simulated events.

3.2 Isochrone Concept

In order to estimate the far-field motion $\mathbf{u}(\mathbf{x}_R, t)$ at receiver R, due to P or S wave radiation from an extended fault area S, we start from the representation theorem for a homogeneous, isotropic medium (Aki and Richards [2002], p. 493):

$$\mathbf{u}(\mathbf{x}_R, t) = \iint\limits_{S(t)} d\mathbf{x}' \, \frac{\mu \, \mathbf{R}^c}{4\pi\rho c^3 \mathbf{r}} \Delta\dot{u}(\mathbf{x}', t - \frac{\mathbf{r}}{c}) \tag{3.2}$$

(where $\mathbf{r} = ||\mathbf{x}' - \mathbf{x_R}||$ is the distance between the receiver R located at $\mathbf{x_R}$ and the point $\mathbf{x}'$ on the fault, c is either the P or S wave velocity, ρ is mass density, μ the shear stiffness, $\mathbf{R}^c$ the radiation coefficient and S the

fault surface). $\Delta\dot{u}(\mathbf{x}', t - \frac{\mathbf{r}}{c})$ is the slip rate at point $\mathbf{x}'$ on the fault for a retarded time relating to wave propagation from the fault. Such integration is schematically represented in figure (3.1-b).

If we assume that our receivers are sufficiently far from the source that the distance $\mathbf{r}$ from each point of the surface S does not change significantly (i.e. Frauenhaufer approximation), and neither does the directive radiation coefficient $\mathbf{R}^c$ (Aki and Richards [2002], p. 493). Under such circumstances, all constant terms can be extracted from the integral in expression (3.2) yielding:

$$\mathbf{u}(\mathbf{x}_R, t) = A \iint_S d\mathbf{x}' \, \Delta\dot{u}(\mathbf{x}', t - \frac{\mathbf{r}}{c}) \tag{3.3}$$

where

$$A = \frac{\mu \, \mathbf{R}^c}{4\pi \, \rho \, c^3 \, \mathbf{r}} \tag{3.4}$$

In practice, the amplitude term A depends on a particular combination of source-station geometry. However our aim is to reproduce the scaling observed in catalogues used for early-warning estimates where the significant mean value of A is the peak amplitude in particle motion averaged over a number of randomly distributed station locations. Therefore we can take the mean value making the assumption that the variations of A for a given earthquake will tend to average out over a randomly distributed station network. In addition, the PGD catalogues studied by Zollo et al. [2006] are normalised in order to yield a rescaled amplitude for all stations at a reference distance $\mathbf{r} = 10\,\text{km}$ from the hypocentre. Thus we may neglect variations due to attenuation in A for the construction of our simulated catalogue. One consequence of this simplification is that our synthetic data will be subject to a smaller dispersion of data than that observed in the natural catalogues, from station to station, while the mean value may be expected to reproduce a reasonable scaling with earthquake size.

Depending on the assumptions made on the source rise time with respect

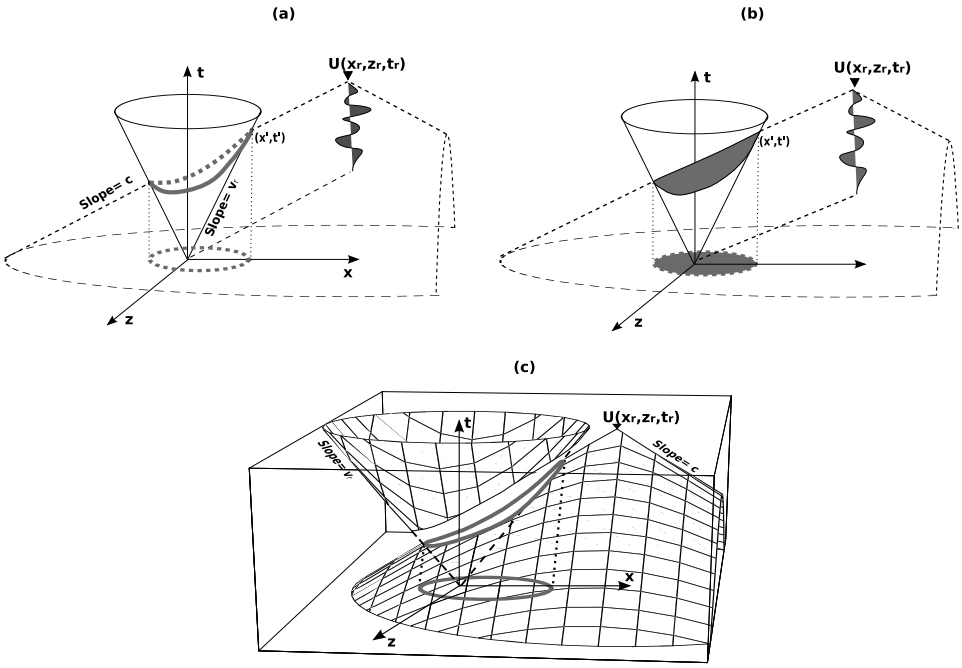

Figure 3.1: The three schematics depict the seismic waves causality cone (for given wave velocity c, receiver position (x_r, z_r) and time t_r) and the rupture front (spreading at constant velocity v_r from the hypocentre at the origin). The (x, z) plane represents the fault surface, while the vertical axis is time (for clarity in this graphic only, we assume that the receiver is along the fault strike, i.e., $y = 0$). The intersection between the two cones represents the *isochrone* (used in kinematic models A, B and C) represented by the saddle-shaped grey curve in (a) (its projection on the x, y plane is also shown for clarity). In (b) the area of the causality cone delimited by the isochrone is shaded in grey, and its projection onto the x, y plane too. The isochrone curve in (a) corresponds to the integration curve $I(t)$ for models A and C, wile the shaded area in (b) corresponds to the integration area $S(t)$ for model B. $U(x_r, z_r, t_r)$ is the recorded ground motion at position at time t_r (motion at previous times is schematically represented as a wiggly curve, whose bottom is located at the time of first arrival). See text for further details.

to the rupture duration and the frequency of the seismogram, we shall define three different models. For simplicity, we shall concentrate on scaling and neglect complexities in the source by assuming a simple rupture model with constant rupture velocity and where the slip function is a ramp in time (these features are those of a classic Haskell fault model, with the exception that the rupture front is expanding circularly). We also neglect high-frequency radiation effects that may originate at fault boundaries or due to complexity in the rupture front advancement, as these are specific to each individual earthquake source as opposed to the mean value from a catalogue.

3.2.1 Model A: short rise-time and the isochrone

If we make the assumption that rise-time is short (pulse-like model) with respect to the duration of rupture propagation–therefore all of the slip occurs at or near the rupture front– the the slip rate may be approximated in terms of a Dirac function $\delta(.)$and the final slip Δu, as denoted by:

$$\Delta\dot{u}(\mathbf{x}', t) = \Delta u(\mathbf{x}')\,\delta(t - t_r(\mathbf{x}')) \tag{3.5}$$

where t_r the rupture time at point $\mathbf{x}'$ (this model corresponds to the schematic representation of figure 3.1-a). In such case, Bernard and Madariaga [1984] and Spudich and Frazer [1984], proposed that equation 3.2 be simplified into the line integral

$$\mathbf{u}(\mathbf{x}, t) = \int\limits_{I(t)} d\mathbf{x}'\, \frac{\mu\, \mathbf{R}^c}{4\pi\, \rho\, c^3\, \mathbf{r}} \Delta u(\mathbf{x}') \tag{3.6}$$

along the contour $I(t)$, or *isochrone*, defined as the group of points on a fault whose radiation arrives simultaneously at a given seismic station (see figure 3.1 for a geometrical interpretation of the isochrone). On the fault the radiation produced by the rupture front is differentially delayed during wave propagation depending on the rupture fronts position relative to the seismic station. Therefore the radiated energy that arrives at a station for a given

time does not necessarily represent an instantaneous snap shot of the rupture front on the fault for a universal rupture time. Instead it represents varying amounts of the rupture history depending on station location relative to the fault plane and hypocentre. The computation of $I(t)$ is briefly recalled in appendix 3.A.1.

Upon making the assumption of equation. (3.3) (i.e the attenuation and radiation terms are averaged-out for a large number of station and that source-receiver distance is normalised), we obtain:

$$\mathbf{u}(\mathbf{x}, t) = A \int_{I(t)} \Delta u \, d\mathbf{x}' \tag{3.7}$$

If we neglect inhomogeneities over the fault we may assume constant Δu across a fault plane but whose value is dependent on the fault dimensions (a feature we shall discuss in more detail later on). Our first catalogue shall be based on model A, i.e., where far-field motion depends merely on isochrone length $I(t)$ as in equation (3.7) and figure (3.1-a), scaled by the mean slip Δu.

3.2.2 Model B: long rise-time

If the rise-time is not short with respect to the duration of rupture propagation (i.e., crack-like model), the integration of equation 3.2 cannot be reduced to the contour of fracture front, but covers the whole actively slipping area instead (as schematically illustrated in figure 3.1-b).

The most simple slip representation is a ramp function (Haskell fault), where slip-rate, assuming fracture continues to grow (i.e. we are assuming there is no healing pulse), may be described by

$$\Delta\dot{u}(\mathbf{x}', t) = \Delta\dot{u}(\mathbf{x}') \, H(t - t_r(\mathbf{x}')) \tag{3.8}$$

where $H(.)$ is the Heaviside function. Upon substituting equations (3.8) and (3.4) into the representation theorem (equation. 3.2) we obtain the far field

radiation in the form of the surface integral:

$$u(\mathbf{x},t) = A \iint_{S(t)} \Delta\dot{u}(\mathbf{x}')\, d\mathbf{x}', \tag{3.9}$$

where $S(t)$ is the fault area delimited by the isochrone $I(t)$.

3.2.3 Model C: short period

Our third and final model assumes that the fracture is crack-like as in model B (long rise-time) but that the period of observation (i.e. passing band of the seismogram) is short with respect to rise-time. If we assume a simple slip such as a ramp function or a Kostrov function (Kostrov [1964]), high-frequency far-field radiation will originate mainly from the fracture front (and eventually a later healing front or complexity in slip time-history which we do not consider here). Moreover, it can be shown that the far field, high-frequency amplitude does not scale with final slip but with slip-rate alone (see appendix 3.A.2). In such a case we obtain an integral contour similar to model A but where the scaling with final slip is replaced by scaling with slip-rate:

$$\mathbf{u}(\mathbf{x},t) = A \int_{I(t)} \Delta\dot{u}\, d\mathbf{x}' \tag{3.10}$$

We note here that under the standard assumption that the stress drop does not depend on the earthquake size, the slip rate $\Delta\dot{u}$, does not scale with earthquake magnitude. In model A, the dependence of far-field amplitude with earthquake size is imposed *a priori* through the scaling with final slip Δu –a somewhat arbitrary feature in the initial phases of rupture– . Such a spurious scaling, which may alter the results of model A, is avoided in both models C and B.

In early magnitude estimation recorded ground motion is initially band-pass filtered removing both very high and low frequencies. This would imply

that early magnitude estimation techniques are measuring neither the rupture front (high frequency) nor the total slip on the fault (i.e. low frequency) but rather the slip that occurs just behind the rupture front over a shortened time. This idea is depicted in figures 3.2 and 3.3, which highlights the different parts of the slip function that radiate energy in different frequency bands.

In figure (3.1-a), the isochrone contour coïncides with the contour integral in both models A and C, where it is assumed that the major radiation originates at the rupture front. However, model B integrates the radiation from the whole area inside the isochrone, as represented by the grey surface in figure (3.1b). Thus the grey contour in (3.1-a) contributes to displacement $U(x_r, z_r, t_r)$ for models A and C, while the grey shaded area in (3.1-b) contributes to $U(x_r, z_r, t_r)$ for model B.

It should be noted that in our isochrone modelling the definition of slip arrest varies between the three models. In the case of models A and C, when a part of the isochrone touches a side of the fault boundary and stops, it equates to switching off slip on this section of the isochrone, since radiation exclusively comes from the propagating rupture front. In the case of model B, where we are assuming a crack model, slip is integrated over the area inside the isochrone even if some part of the front has reached a fault boundary. In terms of comparing models A, B and C with natural earthquakes, models A and C may slightly underestimate ground motion owing to the severity of the arrest condition. Model B on the other hand may overestimate ground motion owing to the lack of representation of stopping phases.

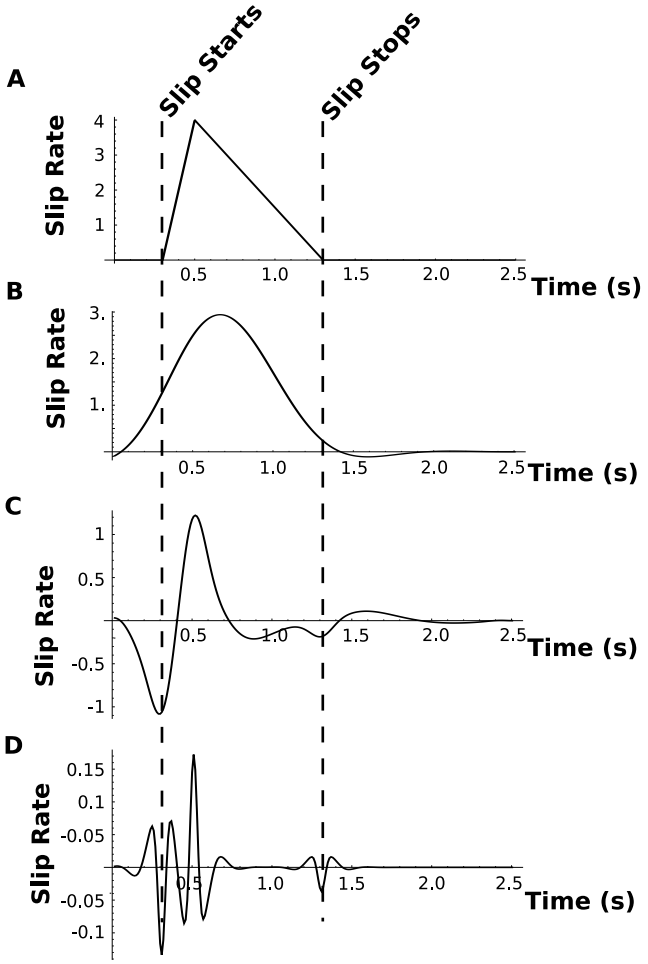

Figure 3.2: This figure highlights the effect that filtering has on information provided by the source. Graph A defines a simple source time function whose slip rate is defined in relation to time. The duration of the function is one second, however, the image of the source time recorded at a seismic station maybe distorted depending on the relative position of the receiver with respect to the fracture propagation direction due to the Doppler effect.Graphs B, C and D are bandpass filtered version of graph A whereby the frequency range was set at 0-1Hz, 1-5Hz and 5-15Hz respectively. Comparing the four graphs we can see that at low frequencies the broad shape of the source time function radiates energy however for higher frequencies the parts of the source time function that is radiating energy moves to the function's edges. It should be noted that the slip rate has not been given any units in this figure as it is a general representation of slip on a fault plane.

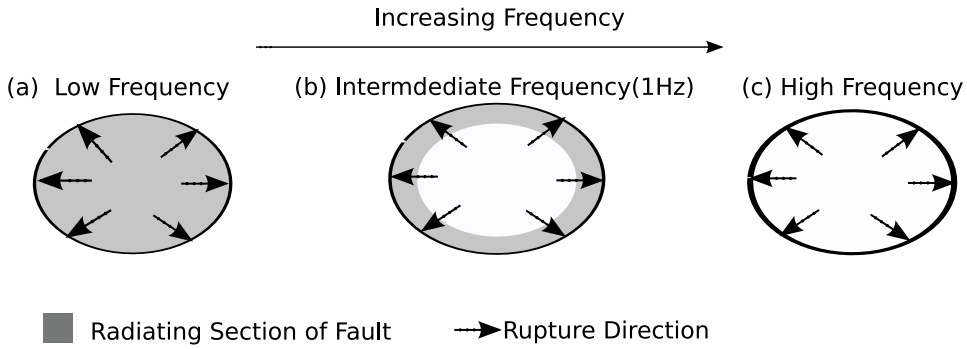

Figure 3.3: Whilst, figure 3.2 depicted the radiation emitted by one point on a fault, this graphic highlights the affect bandpass filtering has on radiated energy from rupturing earthquake. The grey area denotes the section of the fault whose seismic radiation dominates far field particle motion for a rough frequency range. Going from (a) to (c) the area of the fault radiating energy decreases from the total slipping area at low frequencies to just the rupture front at high frequencies. Given that most early warning techniques apply a bandpass filter, it is possible that the case (b) is what is being measuring - i.e. surface area of the rupturing area as well as a small section of the slipping area.

3.3 Some interesting features of isochrone-based models

The difference between the rupture fronts position and the isochrones position after a set period of time has been highlighted in figure 3.4. The black dot representing the hypocentre acts like a focus of an ellipse for the black line which is the isochrone representing a period of two seconds on the seismogram (the station is 10kms away with an azimuth of 70^o). The dashed lines depicts the position of the rupture front from 1 to 4 seconds after the initiation of rupture for a circular rupture front with a constant rupture velocity. In figure 3.4 we can see that the isochrone covers over 4 seconds of rupture history in the direction of the receiver. The amount of rupture history enclosed in the isochrone will depend on station-hypocentre position, rupture velocity, and the seismic wave velocity. As stations are always positioned above hypocentres particle motion naturally contain a more complete rupture history about the area above the hypocentre. From figure 3.4 we see that information on rupture below the hypocentre takes longer to reach seismographs and would therefore be less significant in early warning estimation.

Figure 3.5 is an example of the evolution of the isochrone length for a station 30km from the hypocentre with an azimuth of 45^o. As our square fault occupies a 10km x 10km area this would be equivalent to a magnitude 5 - 6.5 earthquake (depending on the average stress drop). The rupture velocity is set at 2.5km/s while the wave velocity is 4km/s in the media surrounding the fault. The top right and top middle graphic depict the isochrone length and the percentage of the total area of the fault covered respectively. Interestingly we see that by 3 seconds the isochrone has covered over 80% of our fault. Peaks in isochrone length (which are proportional to peak far field displacement) occur just before the isochrone interacts with

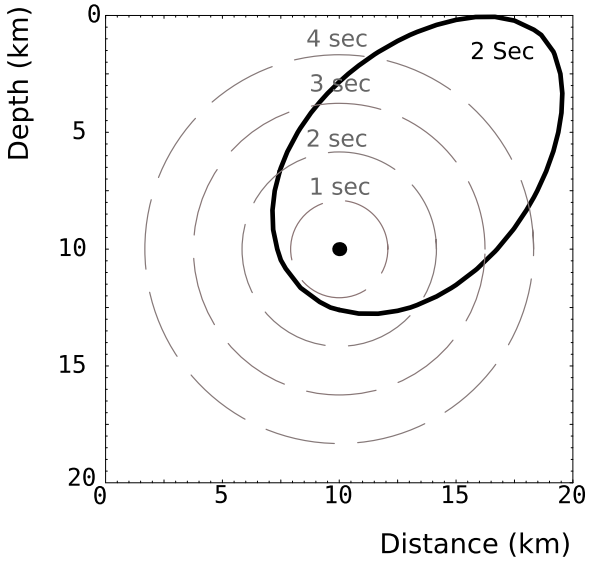

Figure 3.4: An example of an isochrone projection on a fault plane. The black line denotes a s-wave isochrone of 2 seconds duration for a station 10kms away with an azimuth of 70 degrees. The dashed lines give the position of a circular rupture front with a constant rupture velocity of 2.1km/s for 1, 2, 3 and 4 seconds. The s-wave velocity in the medium was set at 2.6km/s. It should be noted that the area encompassed by the 2 second isochrone is much larger than that of the equivalent 2 seconds covered by the rupture front. While such a large discrepancy is not as pronounced for p-waves. In general an isochrone is at least equal to or bigger than the equivalent rupture front .

the fault barrier (graphics a,b,c in figure 3.5 are snap shots of the isochrone on the fault plane when these peaks occur). The first and largest peak in the isochrone length occurs when the isochrone encounter its first barrier which is 1 second after the first arrival of the seismic wave at the receiver.

It is these peak isochrone lengths and the area that they encompass that we shall focus our study on. We have shown the isochrone length and area is proportional to far field displacement, and, by means of our kinematic modes (A, B and C) we can create a parameter that is similar to far field peak displacement. In particular, we are interested in seeing whether this theoretical peak displacement scales with the earthquakes magnitude and at what time period after the initial p-/s-wave arrival.

As the linear magnitude scale that Zollo et al. [2006] and Wu and Zhao [2006] observed was for an average peak displacement for a variety of stations for each magnitude bin we too shall try and mimic their results. Taking multiple stations we compute our simplified peak ground displacement for each station for time periods of 1, 2, 3, and 4 seconds after the p-/s-wave arrival. The magnitude of the earthquake that our seismic stations are measuring is determined by the fault size. The specific details of this kinematic model are discussed in detail in the next section.

3.4 Scaling slip, fault dimension and magnitude

To create a catalogue of varying magnitude we shall create a variety of faults whose dimensions shall scale with magnitude. By making the assumption slip Δu scales with fault length (Scholz [1982]):

$$\Delta u = \frac{C\Delta\sigma}{\mu} L \tag{3.11}$$

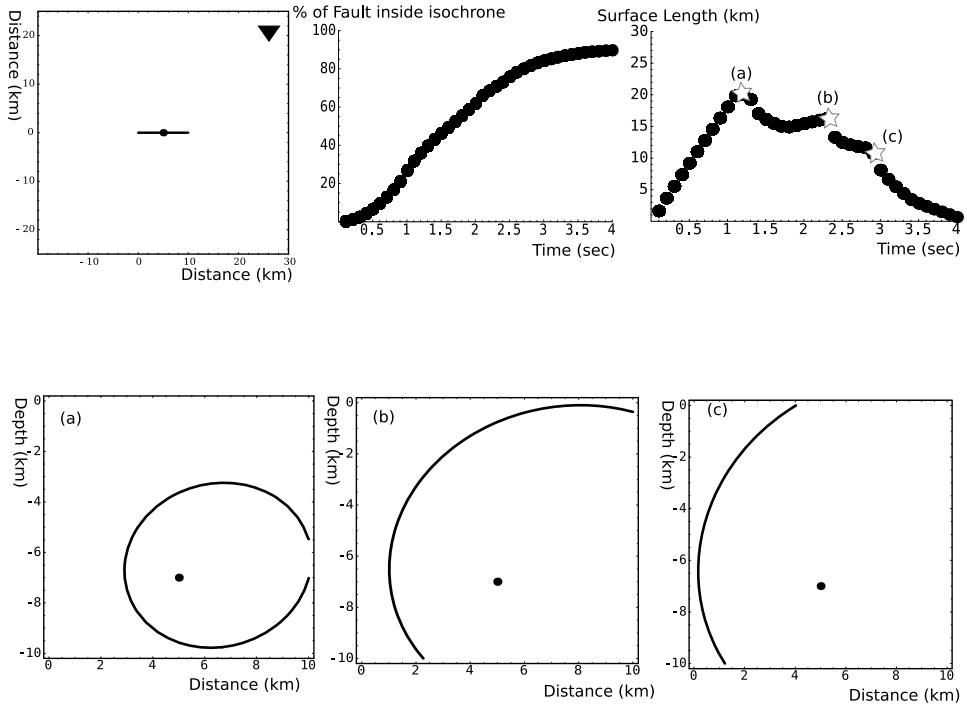

Figure 3.5: This highlights the evolution of the isochrone length and area over time for a given station. The top left diagram is a planar view of the strike of the fault (solid black line), with the black dot denoting the earthquakes epicentre and the triangle the station location. The top centre graphic denotes the percentage of the fault covered by isochrone with time (which is equivalent to model B), while the top right graph shows the evolution of the isochrones surface length with time (which is similar to models A and C). The pictures on the bottom tier show the isochrone on the fault for peak isochrone surface lengths (which are denoted by stars in the top right graph).

where L is fault length, $\Delta\sigma$ is the stress drop (set to 1.5MPa for all our earthquake models) and C is a dimensionless factor of the order of 1 which relates to fault geometry. Taking the standard definition for the moment, $M_o = \mu S_f \Delta u$, where S_f is the area of the fault, the length can now be written in terms of the seismic moment:

$$L = \sqrt[3]{\frac{M_o}{\Delta\sigma}} \tag{3.12}$$

In this case we have assumed our fault is square in shape and thus $S_f = L^2$. This shall be one of the fault models that we shall use and shall be referred to as the Square Fault Model.

The second fault shape changes from a square to a rectangle in an effort to mimic the thickness of the seismogenic layer. For this reason the fault shall be square for small moments, however on reaching the bottom of a predefined seismogenic layer the fault width becomes constrained and so the fault can only expand laterally for large events. Consequently equation 3.12 is re-written for what shall be termed the Rectangular Fault Model:

$$L = \begin{cases} \sqrt[3]{\frac{M_o}{\Delta\sigma}} & L < W \\ \sqrt{\frac{M_o}{W\Delta\sigma}} & L \geq W \end{cases} \tag{3.13}$$

For all rectangular fault models, W is assimilated to a seismogenic thickness of 15km which corresponds to a magnitude 6.3 in our catalogue. Finally, in order to present our catalogues in terms of magnitude, we use the established definition of magnitude-moment Hanks and Kanamori [1979] to define a magnitude M_w in terms of M_o:

$$M_w = \frac{2}{3}(\log_{10} M_o - 9.1) \tag{3.14}$$

We can now define our fault dimensions for our two different fault types (i.e. Square and Rectangle) in terms of a range of magnitudes using equations 3.14,3.13 and 3.12 thus allowing us to construct a catalogue.

In the case of Model A (i.e. short rise time isochrone model) equation 3.11 shall be used for the mean slip in equation 3.7's calculation of the ground displacement.

3.5 Simulated peak ground motion catalogues

Each catalogue consists of a number of earthquakes over a magnitude range of 4 to 7.6. In the catalogue, the earthquakes increase in size by 0.3 M_w with a number of earthquakes making up each bin (i.e. 8 events per bin for 4 - 6.4M_w and 4 events per bin for 6.7 - 7.6M_w).

For all fault shapes and sizes the dip and strike is set to 90 degrees. The hypocentre is constrained to depths of 10kms or more. For this to happen small earthquakes whose width is less than 10km's are forced to occur at depths such that the bottom of the fault is always below 10kms. The location of the hypocentre is randomly distributed inside of the fault.

Station locations are also randomly distributed over a predefined area (which is dependant on the size of the fault). For square shaped faults seismic stations are distributed inside a circular area centred on the centre of the fault with a radius of 50km. The exception to this distribution is for rectangular faults (which range in size from 6.7 M_w to 7.6 M_w). In this scenario random station distribution is contained inside a rectangular area whose boundary is related to that of the faults length (see figure 3.6).

Due to the simplistic nature of the model, the velocity of seismic waves from the fault to the station (i.e. the seismic velocity) is homogeneous. Two different velocity models were used as detailed in table 3.2, in both cases the s-wave velocity and rupture velocity were proportional to the p-wave velocity. For the s-wave the media was assumed to be Poissonian (i.e. $v_s = \frac{v_p}{\sqrt{3}}$) while

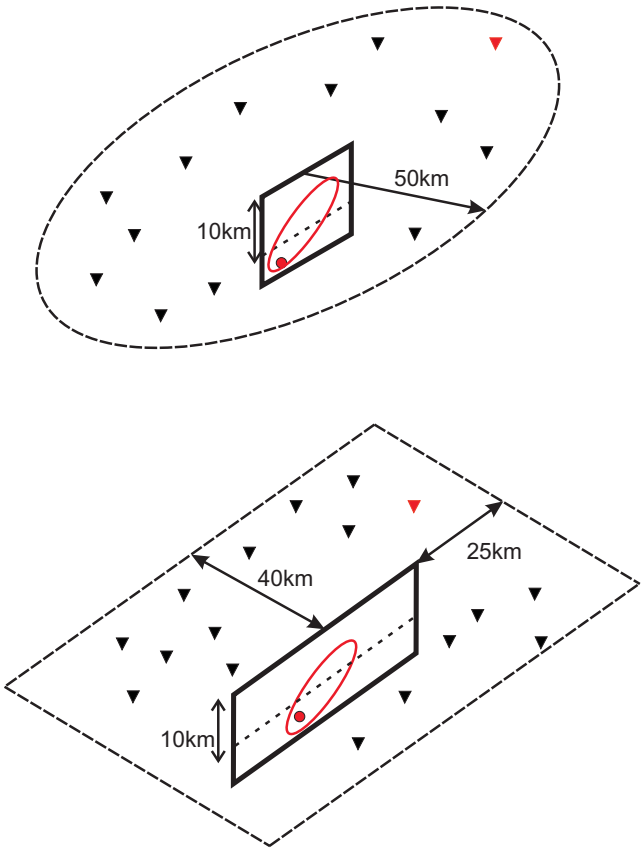

Figure 3.6: This is a planar of view of the two types of station distributions used for isochrone model. Triangles denote randomly distributed seismic stations. The solid black line represents the strike of the fault, while the dashed line denotes the maximum extent for a seismic station to be located. Distribution (a) was used for all square models whereby the maximum extent of station locations is 50km from the centre of the fault. Distribution (b) was used for rectangular fault models whereby the size of the rectangle is a function of the faults width.

the rupture velocity is slightly slower than the Raleigh wave velocity (i.e. $v_r = 0.8v_s$).

In order to calculate the peak ground displacement the average wave propagation constant, A, found in equations 3.7, 3.9 and 3.10 needs to be evaluated. As our wave velocity varies between 5.5 to 2.6km/s we shall take an average value of 4.05km/s with the medium having a shear modulus of $\mu = 30GPa$ and a density of $\rho = 3,300kg/m^3$. The radiation coefficient shall be assumed to be approximately $\mathbf{R}^c \approx 1$ and by taking an equivalent source - receiver distance as that used by Zollo et al. [2006] we set $\mathbf{r} = 10km$. This means that A is of the order of $10^{-9}m^{-2}s^{-1}$ for all model cases.

The ground displacement shall be calculated for Model A using the mean slip as defined by equation 3.11 whereby C is assumed to equal 1. In the case of models B and C we need to calculate the slip rate. By taking the average slip rate on the fault we can say that $\Delta\dot{u}(\mathbf{x}') = \Delta\dot{u}$ in equations 3.9 and 3.10. Using the asymptotic slip rate for the Kostrov crack (Kostrov [1964]), and assuming that the rupture velocity is close to the shear wave velocity we can obtain an approximate scaling of the slip rate:

$$\Delta\dot{u} = \frac{2\beta}{\mu}\Delta\sigma \tag{3.15}$$

where β is the s-wave velocity, μ is the shear modulus and $\Delta\sigma$ is the stress drop. In the case of our models, equation 3.15 becomes 0.318 m/s when the s-wave is 3.18km/s and 0.26m/s when it is 2.6km/s. Since slip rate $\Delta\dot{u}$ does not depend on fault dimensions, models B and C have the advantage of avoiding the bias of magnitude-based slip dependence built into model A. Given the units used in definition values for variables all catalogues the PGD estimates shall be calculated in meters.

3.6 Kinematic Results

For all results (i.e. figures 3.7, 3.8, and 3.11) the base 10 logarithm of the peak ground displacement (PGD) is plotted for each station as grey triangles. The average value for each magnitude bin is represented by black boxes. The dashed black line denotes a linear best fit over a defined magnitude range and the black lines either side of it depict 95% confidence interval of our best fit curve to the data at each magnitude bin. Our analysis of the kinematic results has been divided by fault type - i.e square and rectangular faults. The results discussed and viewed in figures 3.7, 3.8, and 3.11 are based on p-wave velocity profile of 4.5km/s although the same general trends apply for both velocity models (i.e. $v_p = 5.5$km) as well as for s-wave velocities.

In all our kinematic models (i.e. square and rectangular fault shapes, and kinematic models A, B and C) we do see a general trend of magnitude scaling with PGD. The magnitude range of the scaling is dependent on the kinematic model type (figure 3.7) and the observational time window (figure 3.8). The slope of the best fit lines which range between 0.46 and 0.93 in our synthetic catalogue (table 3.4) is in a similar range to that produced by the observational catalogues which used PGD (i.e. 0.51 to 0.81 – see table 1.2). In relation to the amplitude produced by our kinematic models, Model A gives the smallest amplitude, this is to be expected as it only accounts for slip near the rupture front. Model C's amplitude range is between Model's A and B as it corresponds to particle displacement that has been band passed. Model B produces the biggest amplitudes as it represents low frequency particle motion (due to a slip-rate over the whole slipping area on the fault plane) for a crack-like model. Model B's amplitude range is nearest to that seen in Zollo et al. [2006] catalogue. It should be noted, however, that Model's B and C used the asymptotic slip rate which is the slip rate far from the rupture front and therefore lower than the average value, thus making the PGD

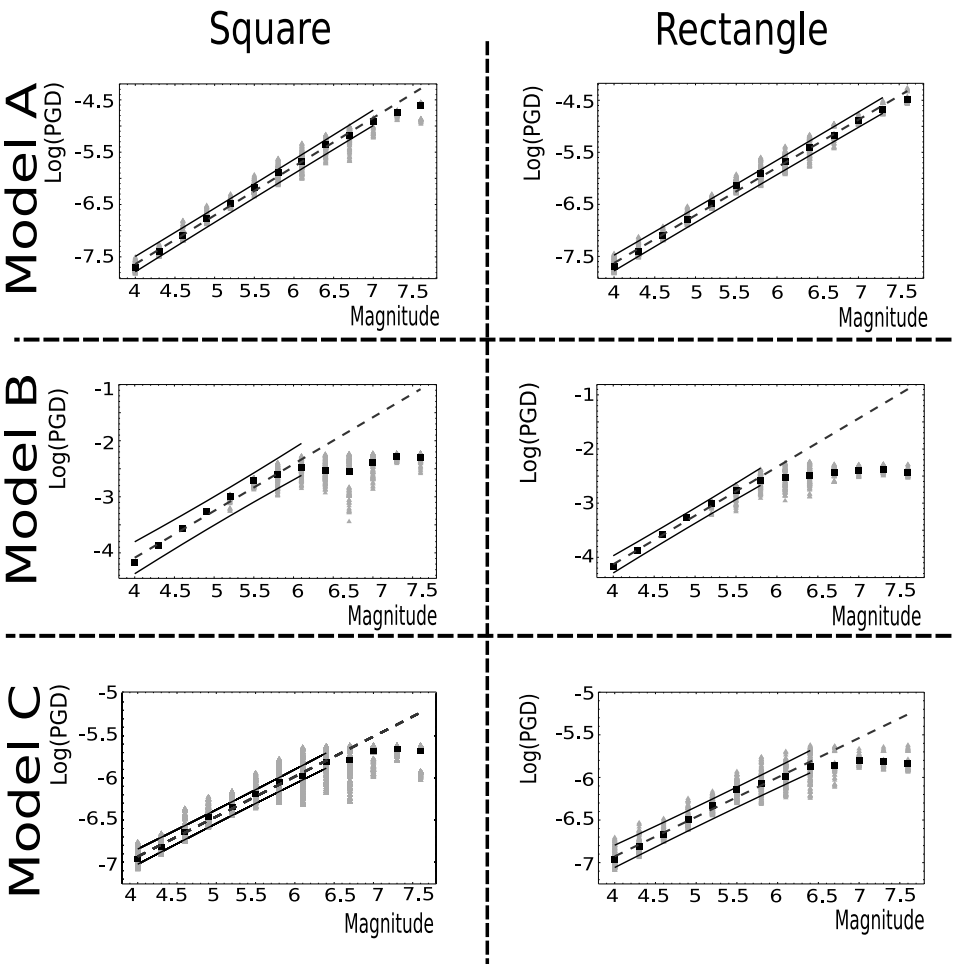

Figure 3.7: Comparing how PGD scales over a magnitude range of 4 to 7.6 for two different fault shapes (i.e. square and rectangle) and three different kinematic model types. Grey triangles represent the PGD at individual stations, whilst the black boxes represent the average PGD values. The black dotted line denotes the linear best fit line, when such a feature is present. The black solid lines denote the 95% confidence values of the best fit lines. This format is maintained for all synthetic catalogues.

smaller than what would be observed in reality. In figure 3.7 the difference in magnitude scaling between a depth constrained fault shape (i.e. rectangle model) and a freely expanding one (square model) is not significant in terms of the magnitude scaling range.

In terms of magnitude scaling in relation to our three kinematic models the range over which the scaling extends varies for the different models. In figure 3.7 we see that the for model A PGD practically scales over the whole magnitude range while models B and C saturate between 5.8-6.4M_w (see figures 3.9 and 3.10 for particular comparisons between models B and C with Zollo et al. [2007] catalogues, see also table 3.4). The saturation of the PGD scaling is a new feature that is seen in some catalogues (Wu et al. [2006], Rydelek et al. [2007], Zollo et al. [2007]) but is not present in all catalogues (Zollo et al. [2006]). The large scaling range seen for model A can be accredited to the *a priori* assumption we make on the scaling of slip with fault size. The saturation that we see for models B and C in figure 3.7 is a common feature of these models.

In the interest of clarity we shall focus on looking at one fault shape and one kinematic model. More examples of catalogues using both fault types and kinematic models have been placed in the appendix 3.A.5. We have chosen the square fault shape, although there were not much difference between the catalogues created using the two different fault shapes.

Model C was chosen from our three kinematic models as we feel this kinematic model best portrays what is being seen in the observational catalogues. Model A was discounted as it is assumes that final slip is reached almost instantly, thus introducing a bias and forcing a scaling with magnitude through slip scaling. We deem this to be unrealistic. Models B and C do not contain this scaling bias, but still show scaling over a more limited magnitude range (figure 3.7) as was previously discussed. Model B assumes that the whole rupture area remains active meaning that the period of observation at each

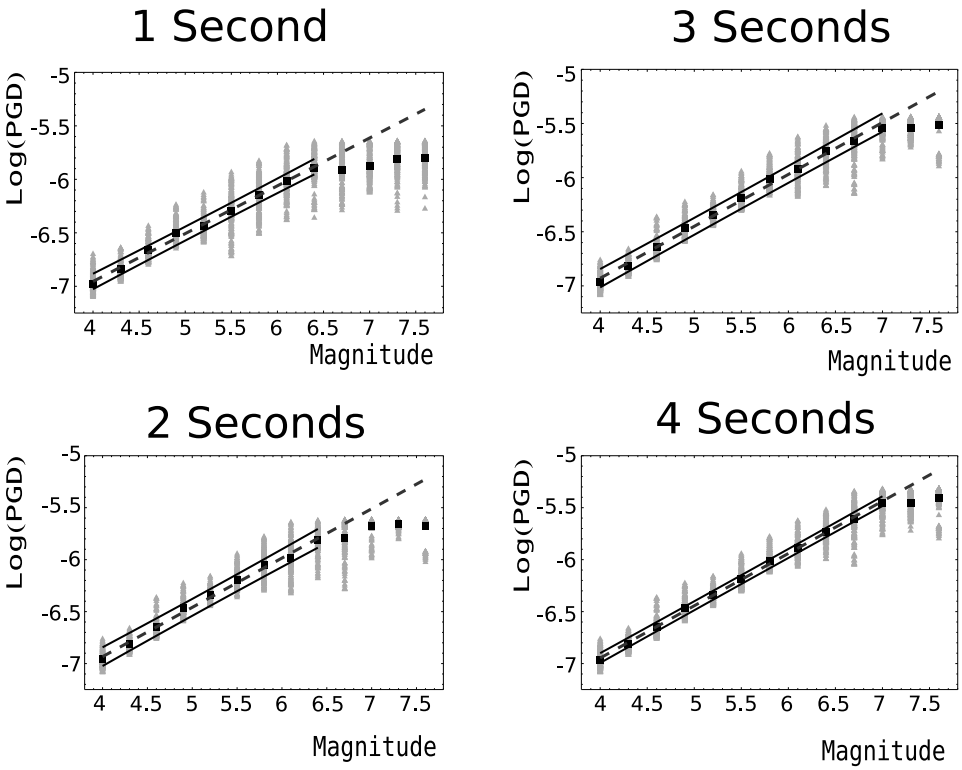

Figure 3.8: Evolution of the scaling between Peak Ground Displacement and Magnitude for ground motion recorded over 1,2,3 and 4 seconds at a variety of randomly distributed stations. In this case the fault is square in shape and the peak ground displacement relates to the p-wave which has a velocity of 4.5km/s. As can be seen the point of saturation migrates to high magnitudes as the amount of time given to recording the ground motion increases.

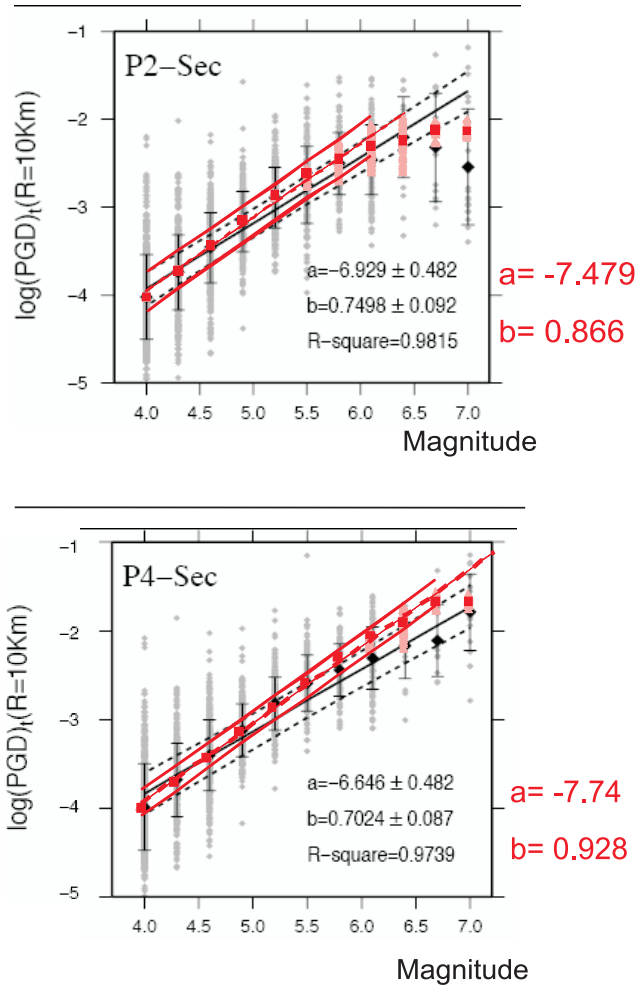

Figure 3.9: Comparison between synthetic (using model B) and observational catalogue (observational catalogue has been taken from Zollo et al. [2007]). Grey and black symbols and lines are observational values whilst the overlaid red and pink are the synthetic results. The top and bottom graphs refer to the PGD recorded in the first 2s and 4s respectively. It should be noted that whilst the best fit slope of the synthetic dataset is true to its original form, a shift has been applied to overall amplitudes of the synthetic dataset so that both datasets can be viewed relative to each other. Such a correction is equivalent to varying the average attenuation value. In comparing the two datasets we see that the slopes of the best fit lines match well, whilst magnitude saturation occurs earlier in synthetic catalogue than in the observational one. The observational catalogues is based on earthquakes from K-Net and Kik-Net arrays in Japan.

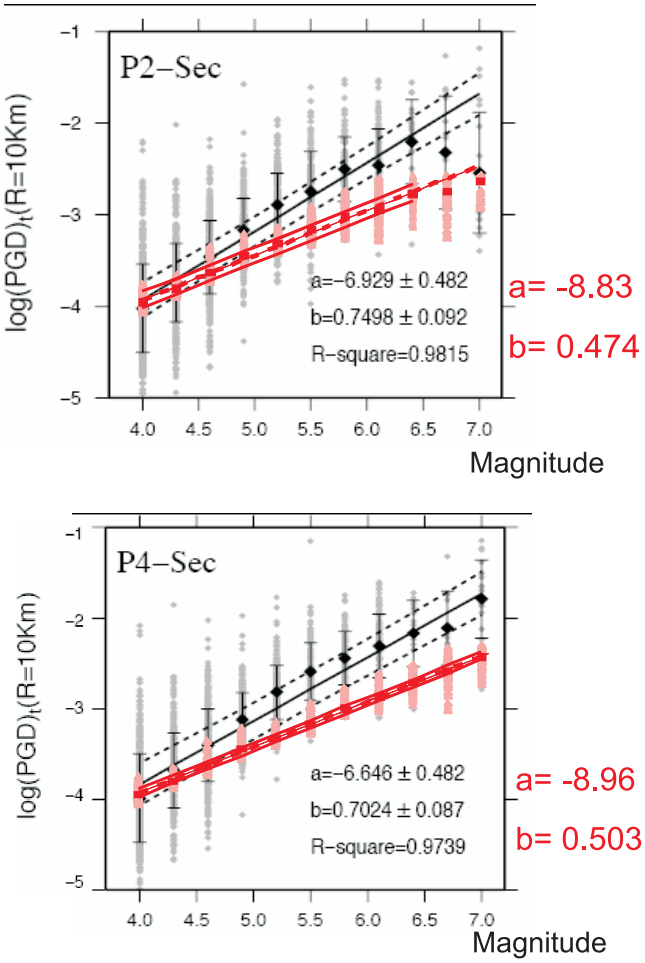

Figure 3.10: Comparison between synthetic (using model C) and observational catalogue (observational catalogue has been taken from Zollo et al. [2007]). Grey and black symbols and lines are observational values whilst the overlaid red and pink are the synthetic results. The top and bottom graphs refer to the PGD recorded in the first 2s and 4s respectively. It should be noted that whilst the best fit slope of the synthetic dataset is true to its original form, a shift has been applied to overall amplitudes of the synthetic dataset so that both datasets can be viewed relative to each other. Such a correction is equivalent to varying the average attenuation value. In comparing the two datasets we see that the slopes of the best fit lines are quiet different, whilst magnitude saturation occurs at the same magnitude seen observationally.The observational catalogues is based on earthquakes from K-Net and Kik-Net arrays in Japan

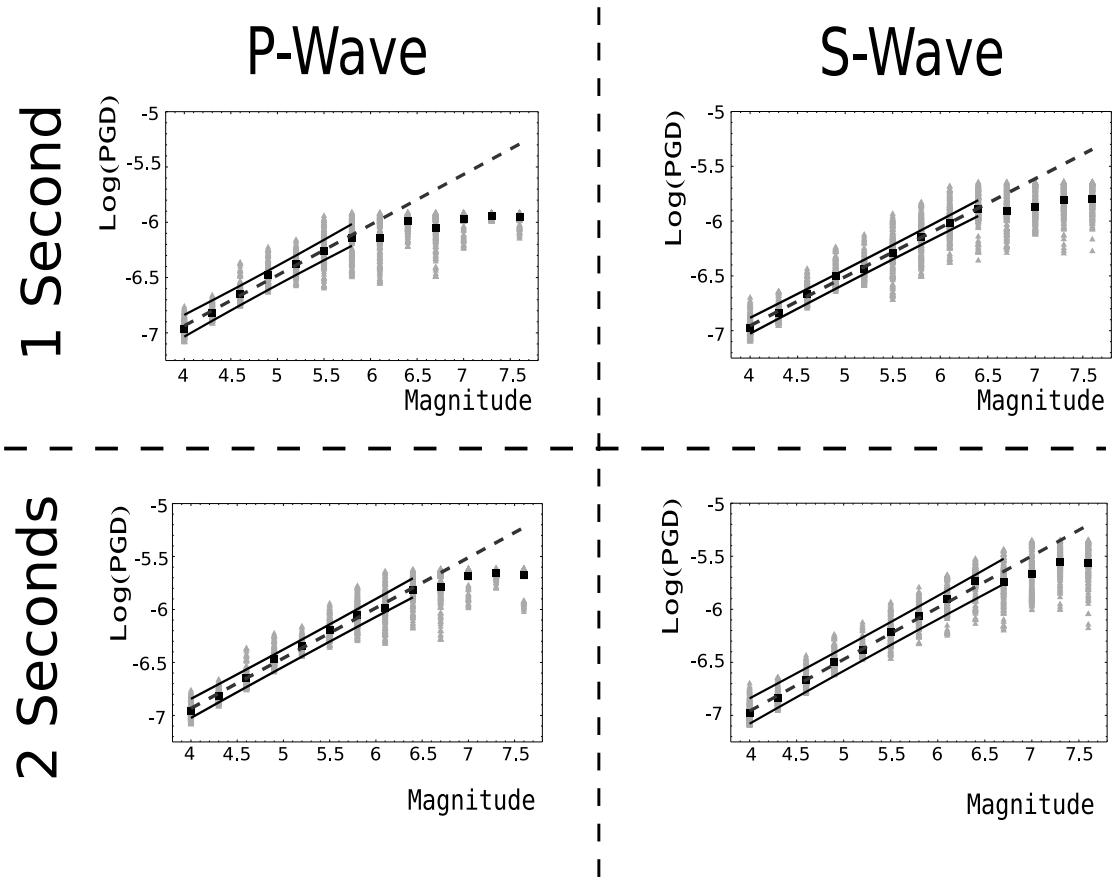

Figure 3.11: Comparison of the scaling of Peak Ground Displacement with magnitude between P- and S-wave catalogues at one and two seconds for a square fault. The p-wave velocity of the medium is 4.5 km/s while the s-wave is 2.6 km/s. The p-wave catalogues saturate earlier than that of the s-waves dues to the relative sizes of the isochrone. The difference in the point of saturation between the two wave types decreases with increasing time period. This is due to the fact that the size of the fault increases logarithmically while the difference between the two isochrone types is constant.

station is of a similar period or longer than the rupture duration. This is more suited to describing scaling seen in smaller earthquakes but would not be as valid for large earthquakes who have large rise times. Model C, however, assumes that the effective radiation originates mainly from the rupture front (i.e. the period of observation is short with respect to the rise time) with no limitations on rupture size. Given that the time window of EW assessment using PGD is limited, the period of observation is also inherently limited. As a consequence the assumptions that we made for Model C may be the most adaptable to the kinematic origins of the scaling we see in the observational catalogues. It is for this reason that we believe that Model C is most realistic kinematic model in relation to EW.

Turning to the evolution of our magnitude scaling with an increasing observation time window we see that the magnitude at which our scaling saturates generally increases too (tables 3.4, 3.5 and 3.6).

Figure 3.8 highlights this evolution for model C using a square fault. The increasing of the magnitude scaling in figure 3.8 can be explained in terms of the position of the rupture front in relation to the observational time window at a far field seismic station.

For small earthquakes the fault size is small and the isochrone covers the total area relatively quickly. Take the example in figure 3.5 where the isochrone had covered over 80% of a M_w5-6 fault in 3 seconds. This means that our peak displacement for small earthquakes is governed by the faults boundary interaction with an isochrone as this controls the maximum isochrone length and area.

When we move to bigger earthquakes the size of the fault is so large that the isochrone does not touch any of the fault edges in the given time period. This means that the maximum isochrone size is no longer determined by the fault edges but by the time period over which the peak displacement is measured and thus we see a break in our magnitude scaling. As the

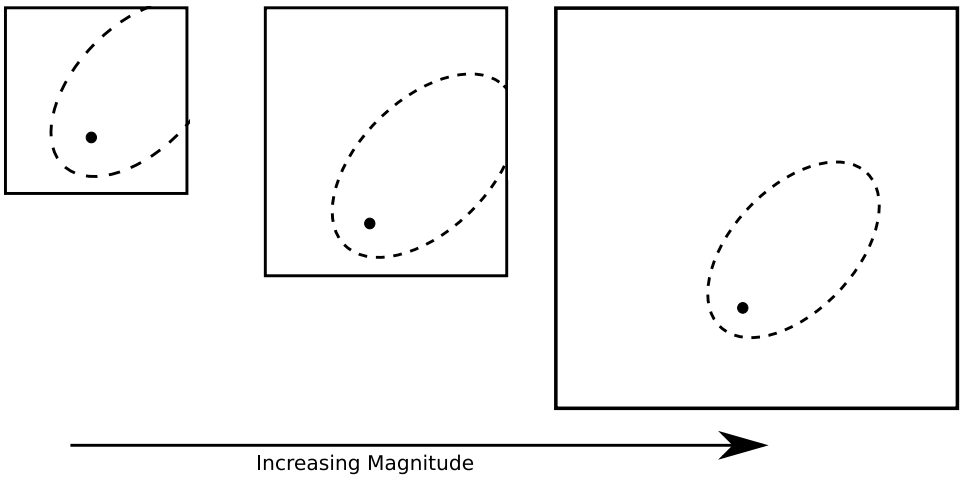

Figure 3.12: In this schematic we view the same isochrone (i.e. the isochrone size remains constant) whilst the fault size (i.e. magnitude increases). Going from left to right, we see that at low magnitudes, when the fault size is small the isochrone is constrained in size by the boundary of the fault. As fault size increases this isochrone-fault interaction decreases as the isochrone size is primarily constrained by the observation time at the station which remains constant. Therefore for very large earthquakes the PGD is grows with increasing isochrone size (i.e. observation window) whilst for smaller earthquakes PGD is determined by the interaction of the isochrone with the fault boundary.

observational time window is increased, the isochrone has a higher probability of reaching its maximum size through fault interaction. This is seen in figure 3.8 where as the time window for observing the peak displacement increases, so too does the magnitude over which a linear scaling can be applied. Indeed the average peak displacements in the saturated magnitude range can be seen to rise as the observation window increases from 1 to 4 seconds.

While the scaling range increases dramatically between 1 and 2 seconds it slows down after this due to the fact that while the isochrones are increasing in size linearly, the fault sizes are growing logarithmically.

3.6.1 P-wave Vs S-wave Catalogues

This difference is also evident when we compare p- and s-wave results in figure 3.11 and table 3.6. As s-waves have a slower velocity than p-waves their isochrones are larger for the equivalent time window (see equation 3.29). Therefore for small observational windows (i.e. 1 and 2 seconds) the magnitude scaling extends over a larger range for s-waves than p-waves. However, for larger time windows (i.e. 3 and 4 seconds) the magnitude scaling range becomes comparable between the p- and s-wave catalogues (see figures 3.13 and 3.22) as the difference between the two types of isochrones become small compared to the fault size.

The difference in the average PGD between the two waves types is more pronounced at low frequencies than at intermediate ones (see figures 3.13 and 3.22 which is in the appendices). This is due to the relative difference in rupturing fault area (model B) covered by the two wave types which is greater than the difference in circumferential distance (model C).

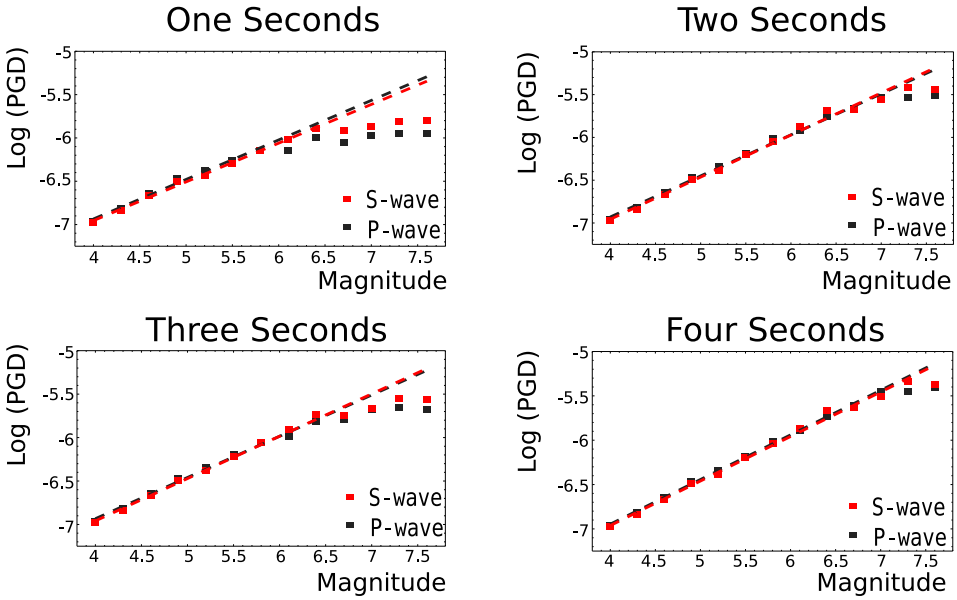

Figure 3.13: For this figure the squares denote the average PGD (i.e. the same values denoted by black squares in earlier plots). Dashed lines are linear best fit lines for the two datasets. Black denotes p-wave values and red s-wave. From the four graphs we can see that s-waves produce larger PGD due to the fact that they cover a larger area of the fault plane. This difference in isochrone size between the two wave types means that the magnitude scaling using s-wave PGD has a slightly larger magnitude range than p-wave PGD. Model C is the kinematic model used for these graphs. P-wave velocity is set at 4.5km/s while the S-wave velocity is 2.6km/s.

3.6.2 Square Vs Rectangular Fault Geometries

In figure 3.14 (and figure 3.21 in the appendices) the difference in the average PGD between square and rectangular faults is highlighted. In figure 3.14 we see that there is a small difference between average PGD between the two fault shapes. This is only apparent at large magnitudes affecting magnitude scaling ranges for observation window of 3 and 4 seconds. This difference in magnitude scaling range between the two fault shapes is quiet small – $0.3M_w$. The difference would probably be a lot more pronounced if the constraining seismogenic depth had been shallower. In figure 3.21 the difference in average PGD between fault shapes using kinematic model B is much smaller than that seen using model C (figure 3.14). This can be attributed to the fact that model B includes the fault boundary in its calculation of the ground motion whilst model C discounts fault boundary contributions thus making it more sensitive to the faults shape.

3.7 Model Limitations

It should be noted that a constant rupture velocity was used, if the rupture velocity was faster our scaling may extend over a larger magnitude range – this would definitely be true for observations over one minute but at 3 and 4 seconds this may not be the case (as the jump in fault area could prove to be too large).

By using a homogeneous velocity profile around the fault we have simplified the influence of off fault features. The addition of a more heterogeneous velocity profile should add more scatter to individual data points in our synthetic catalogues (as seen in actual observations). However the underlying general scaling relationship which is based on the average PGD should still persist.

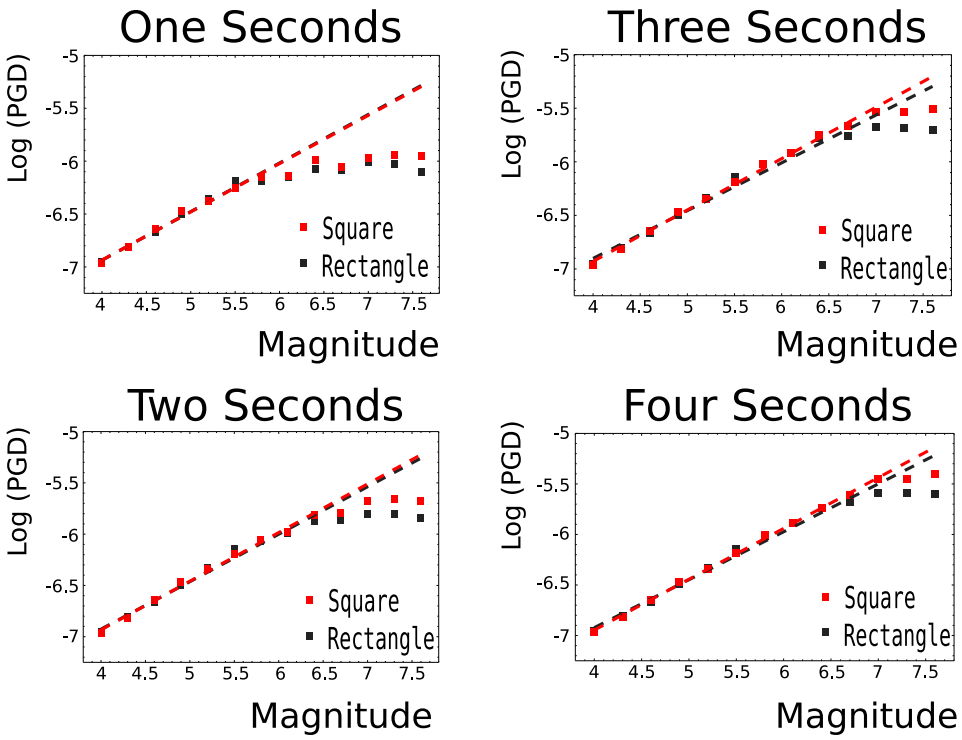

Figure 3.14: This figure depicts the difference between the average peak displacement between square and rectangular faults using Model C for observational time windows of 1 to 4 seconds. P-wave velocity is set at 5.5km/s. Black and red box symbols depict the average PGD for rectangular and square fault types. Black and red dashed lines denote best fit line for magnitude scaling for rectangular and square faults respectively

Finally, another simplification taken was to keep the dip of the fault set at 90^0 in all simulations. A dipping fault plane shall produce a different isochrone to that on a perpendicular fault with the isochrone being elongated for stations on the down dip side of the fault and smaller on the up dip side. This feature becomes more pronounced with the increase in dip. Again the addition of such a feature in our synthetic catalogues shall an some more scatter to individual data points. Fortunately, the average PGD should be greatly effected as increases in PGD seen on the down-dip side of the fault shall be balanced with decreases observed by stations on the up dip side.

3.8 Kinematic Discussion

3.8.1 Applying early magnitude estimation to very large events

As we have already noted in figure 3.8, the point at which magnitude scaling breaks down increases with increasing time window. The saturation magnitude for scaling increases with increasing time window. However the rate of increase is not constant: it grows slower as magnitude increases. This is due to the difference in increasing isochrone size – which is linear, with magnitude –which is logarithmic. As has been previously discussed, an isochrone's interaction with the fault's boundaries defines the PGD that scales with final magnitude. Due to the difference in the evolution of fault and isochrone size, at very large magnitudes (i.e. $M_w > 7$) large amounts of time are required in order to get an isochrone interaction with the fault boundary. Figures 3.15 and 3.16 highlights this problem, whereby for one seismic station the maximum isochrone size for a given time period is compared with properties of the fault size (i.e. its' perimeter – figure 3.15 and area – figure 3.16). The dots in figures 3.15 and 3.16 denote the observational time required for an

isochrone to grow to a dimension comparable to that of the final rupture size. In the case of model C, the PGD usually occurs before this, therefore the time estimates should be viewed as being conservative in relation to the synthetic catalogues of model C (i.e. PGD covers a much larger magnitude range than that actually depicted in figures 3.15). This is not the case in figure 3.16 were PGD is obtained when the isochrone's area is comparable to that of the faults. For small magnitudes (i.e. $M_w < 5.5$) an observational time window of one second is adequate for obtaining a PGD that scales with the earthquakes magnitude. However for very large earthquakes (i.e. $M_w > 7$) the amount of time required to get an isochrone whose size is comparable to that of the faults grows exponentially. Whilst figures 3.15 and 3.16 are only one example for one station, only super-shear rupture velocity offers the possibility of generating PGD's in the first few seconds after the initial p- or s-wave arrival that scale with final magnitude size. This is assuming that PGD scaling with magnitude is due only to kinematic effects. This difference in the rate of increase of isochrone size versus fault size may also explain why we don't observe large differences between p- and s-wave catalogues. Similarly for p- and s-wave catalogues, the difference in size between the two types of isochrones is only observable for a small magnitude range (for e.g. $\approx 1M$ for an observation window of 1 sec – see figure 3.13).

3.8.2 Source Frequency Spectra

Isochrone back-projection offers one kinematic method of examining the relationship between PGD and magnitude. An alternative method can be outlined based on the source. Several authors, starting with Aki [1967] and Geller [1976] proposed a theoretical fit of the frequency spectra of earthquakes based on kinematic source functions, which we shall now examine in the context of PGD magnitude estimation.

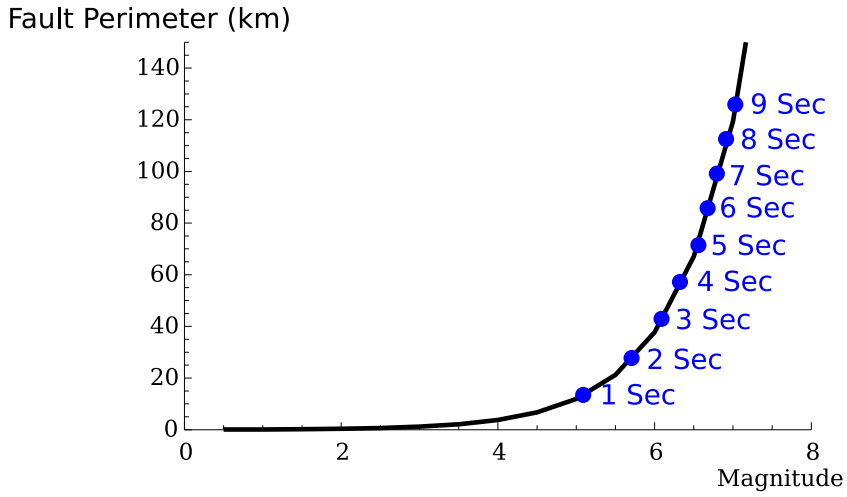

Figure 3.15: Highlighting the difference between the rate of increase in PGD with time for model C and the rate of increase of fault size. The black line represents the increasing fault perimeter with magnitude. The blue dots denote the time need after the s-arrival for an isochrone size to equal that of the faults perimeter for one station. As PGD usually occurs before this, the time estimates should be viewed as being conservative (i.e. PGD covers a much larger magnitude range). However, the important feature of this graph is rate at which the observational time window increases with increasing magnitude. Parameters used are as follows: fault size is determined as stated in section 3.4 with station located at an azimuth of 70^0 and a distance of 10km, with an s-wave velocity of 2.6km/s and v_r=2.1km/s

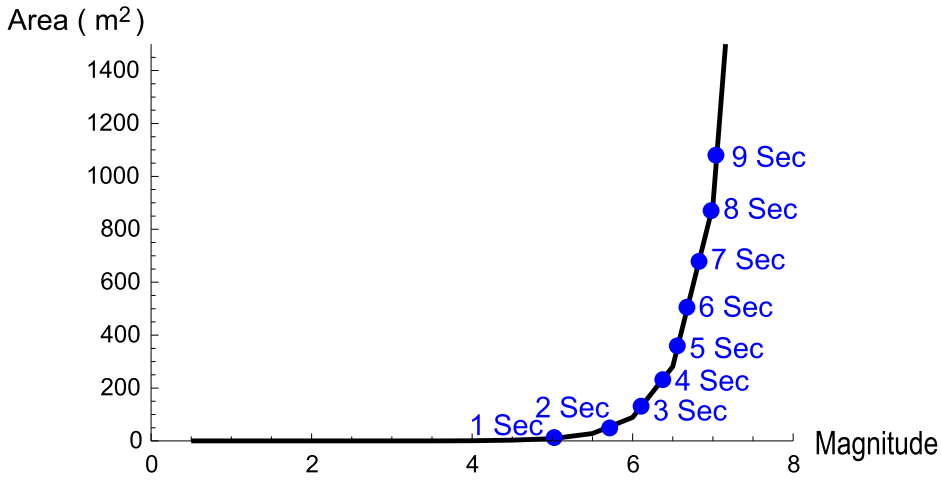

Figure 3.16: Highlighting the difference between the rate of increase in PGD with time for model B and the rate of increase of fault size. The black line represents the increasing fault area with magnitude. The blue dots denote the time need after the s-arrival for an isochrone size to equal that of the faults perimeter for one station. In the case of model B, PGD occurs at the same instant that the isochrone size is equivalent to that of faults therefore the times denoted in the graph are similar to those seen in synthetic catalogues. Again, the important feature of this graph is rate at which the observational time window increases with increasing magnitude. Parameters used are as follows: fault size is determined as stated in section 3.4 with station located at an azimuth of 70^0 and a distance of 10km, with an s-wave velocity of 2.6km/s and v_r=2.1km/s

Amplitude spectrum at low and high frequency

In figures 3.7, 3.8 and 3.11 the equation of the best fit line for magnitude scaling is defined as:

$$\log_{10}|D| = m\,\log_{10}(M_o) + c$$

where D is amplitude of motion and we have assumed that $M_o \approx M_w$. m is the slope of the best fit line used in the scaling and c is the y-intercept constant.

In agreement with Stein and Wysession [2003], we may assume a simple Haskell fault model and approximate the amplitude spectrum in three different frequency domains as:

$$\log(|D(\omega)|) \approx \begin{cases} \log_{10}(M_o) & \omega < \frac{2}{T_R} \\ \log_{10}(\frac{2\,M_o}{\omega T_R}) & \frac{2}{T_R} < \omega < \frac{2}{T_D} \\ \log_{10}(\frac{4\,M_o}{T_D\,T_R\,\omega^2}) & \omega > \frac{2}{T_D} \end{cases} \tag{3.16}$$

In equation 3.16, M_o is the moment, ω is the frequency T_R is the apparent rupture duration and T_D is the rise time of where $T_R > T_D$. The rupture time for a boxcar time function is defined as: $T_R = \frac{2\,L}{v_r} - \frac{2\,L\,\cos(\theta)}{c}$ where L is the radius of the fault, c is the wave velocity, v_r is the rupture velocity and θ is the station-hypocentre azimuth. We shall simplify this expression by assuming $\theta = 90^0$ hence:

$$T_R = \frac{2\,L}{v_r} \tag{3.17}$$

whilst the rise time can be defined as

$$T_D = \frac{\mu\overline{\Delta u}}{\beta\,\Delta\sigma} \tag{3.18}$$

where μ is the shear modulus, $\Delta\sigma$ is the stress drop, $\overline{\Delta u}$ is the average slip on the fault, and β is the shear wave velocity. We shall now rewrite the rupture time and the rise time in terms of the moment.

According to the usual scaling, we can relate average slip to stress drop and seismic moment to average slip as:

$$\overline{\Delta u} = \alpha_a \frac{\Delta\sigma}{\mu} L \tag{3.19}$$

$$M_o = \mu \, \overline{\Delta u} \, \alpha_b \, L^2 \tag{3.20}$$

L is a characteristic fault dimension, $\alpha_b \, L^2$ is fault area. α_a, α_b are dimensionless constants close to 1, depending on fault geometry.

Combining equations (3.17-3.20) and assuming for simplicity $\alpha_a = \alpha_b = 1$, we obtain after some algebra:

$$T_R = \frac{2}{v_R}(\frac{M_o}{\Delta\sigma})^{1/3} \tag{3.21}$$

$$T_D = \frac{1}{\beta}(\frac{M_o}{\Delta\sigma})^{1/3} \tag{3.22}$$

which in turn can be substitute into equation 3.16 and rearranged as follows:

$$\log(|D(\omega,)|) \approx \begin{cases} \log_{10}(M_o) & \omega < \frac{2}{T_R} \\ 2/3\log_{10}(M_o) + \log_{10}(c_1) & \frac{2}{T_R} < \omega < \frac{2}{T_D} \\ 1/3\log_{10}(M_o) + \log_{10}(c_2) & \omega > \frac{2}{T_D} \end{cases} \tag{3.23}$$

where c_1 and c_2 are defined as:

$$c_1 = \frac{v_R}{\omega}\Delta\sigma^{1/3} \tag{3.24}$$

$$c_2 = \frac{2\, v_R\, \beta}{\omega^2}\, \Delta\sigma^{2/3} \tag{3.25}$$

Equation 3.23 proves that magnitude scaling slope seen in figures 3.7,3.8 and 3.11 is dependent on the frequency signal whereby the slope decreases from 1 to 2/3 and finally 1/3 as the frequency increases relative to the corner frequencies.

Equation 3.24 and 3.25 define the y-intercept values for the scaling lines which occurs at $M_o = 1$. Inputting the same values used for table 3.4 from

our kinematic modelling (i.e. $\mu = 30$GPA,$\Delta\sigma$ =1.5MPa, $v_R = 2.1$km/s and $\beta = 2.6$km/s), taking $\omega = 1$ in c_1 and $\omega = 10$ in c_2 and finally multiplying both constants by the average attenuation factor ($A = 10^{-9}$) gives:

$$\begin{aligned} \log_{10}(c_1\, A) &= -6.46 \\ \log_{10}(c_2\, A) &= -6.15 \end{aligned}$$

In comparing this result with table 3.4 we see that both y-intercept value are similar to that seen for the best fit lines in our kinematic models (especially in the case of Model B).

Finally, equation 3.23 refers to particular frequencies relative a generic corner frequency. If however one was to take a frequency between 0.1-1Hz one would expect to cross the corner frequency as the magnitude increased from 1-8M_w (Aki [1967]). In this case one would expect to see a change in the linear scaling slope as magnitude increases, assuming that no saturation has occurred. Whilst the slope shall decrease with increasing magnitude, so too does the y-intercept values (see figure 3.17) whereby setting the observation frequency at $\omega = 1$:

$$\begin{aligned} \log_{10}(A) &= -9 \\ \log_{10}(c_1\, A) &= -6.46 \\ \log_{10}(c_2\, A) &= -4.15 \end{aligned}$$

However, the presence of the intermediate curve is heavily dependent on the difference between the rise-time and rupture duration, features that are often difficult to distinguish. Taking for example the variables used in the isochrone models defined earlier in this chapter (i.e. $\Delta\sigma = 1.5$MPa, $v_r = 2.5$km/s and $\beta = 3.18$km/s) the moment-magnitude equation (i.e. equation 3.14) can be substituted into equations 3.21 and 3.22 to give the magnitude at which the linear scaling changes slope. Therefore assuming that the stress drop and rupture velocity are the same for all earthquakes in our catalogue we find

that the first change in linear trend (i.e. going from a slope of 1 to $\frac{2}{3}$) occurs at a magnitude of $4.8M$ whilst the second change of slope (i.e. from a slope of $\frac{2}{3}$ to $\frac{1}{3}$) occurs at $5.06M$.

On re-examination of the observational catalogues, it is indeed clear that, where most authors have chosen a straight line to represent PGD scaling, a kinked line may also be fitted. The exception to this is Rydelek et al. [2007] whose best fit scaling lines had slopes of 0.93 and 1.06, very similar to those predicted by equation 3.23. Indeed it is possible that Rydelek et al. [2007] underestimated the extent of the magnitude scaling range by discounting linear features after the change in slope. Figure 3.18 highlights this observed kink in catalogues using Zollo et al. [2007] observational catalogue. Whilst the intermediate slope is not visible due to its small magnitude range, the kink in slope occurs between $5.2 - 5.5M$ which is surprisingly similar to our crude estimate in the last paragraph.

Additionally, the magnitude at which this kink in slope occurs in figure 3.18 can be used to estimate the dominant observational frequency range using equations 3.14, 3.21 and 3.22 (a frequency range is taken as the as only one change in slope is clearly visible). Therefore by assuming this kink occurs at a magnitude of $5.3M$ and using the same kinematic values defined earlier (i.e. $\Delta\sigma = 1.5$MPa, $v_r = 2.5$km/s and $\beta = 3.18$km/s), an observational frequency range of 1-1.2Hz is obtained. This is to the lower end of the bandpassed frequency range (i.e. 0.0075-3Hz) used by Zollo et al. [2007] in determining the PGD in figure 3.18. It is natural that the dominant frequency present in defining the PGD scaling is at the lower end of the available frequency range as such frequencies contain larger amplitudes (a case demonstrated by Aki's frequency spectra Aki [1967]). Indeed this influential frequency could be near the lowest observational frequency present in the signal, a feature which is proportional to the length of observational time window (in the case of figure 3.18, this is 4s) and not the frequency filtering range.

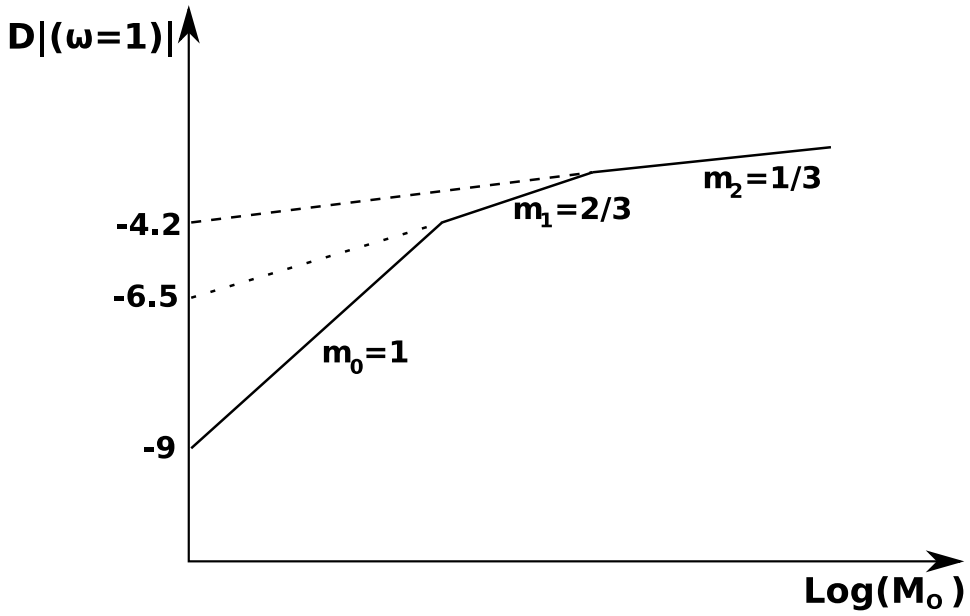

Figure 3.17: This schematic depicts the possible variation of linear scaling for a frequency of 1Hz over a large moment range (which is similar to the magnitude range) assuming that the particle motion is not exhibiting any saturation features (i.e. our observation window is sufficiently large enough). The slope of the best fit lines are defined using equations 3.23,3.24 and 3.25. This schematic assumes that intermediate slope slope is visible, however this is heavily dependent on the value of c_1 relative to A and T_R and secondly to a large difference between rupture and rise time.

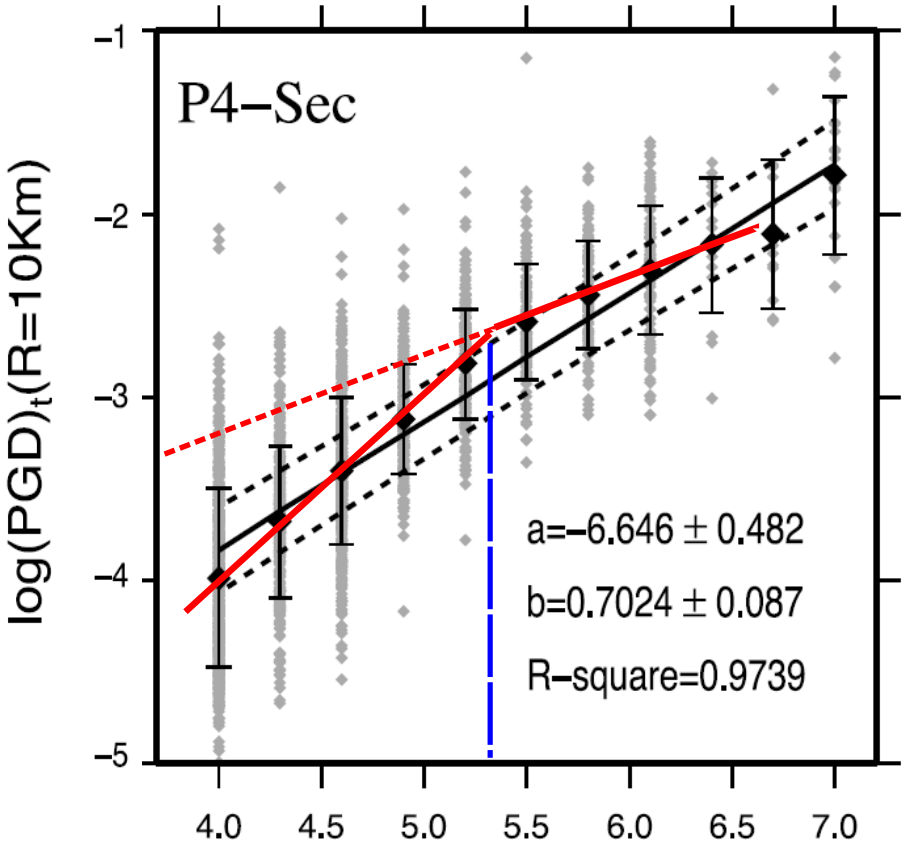

Figure 3.18: Highlighting an alternative scaling relationship for PGD against magnitude. The observational catalogue is that of Zollo et al. [2007] with the grey dots denoting individual PGD values and the black diamonds denoting the average PGD values. The solid black line denotes Zollo et al. [2007] best fit linear trend. The red line depicts an alternative kinked best fit slope, with the blue dotted line highlighting the magnitude at which the change in slope could possibly occur. The observational catalogue is based on earthquakes from K-Net and Kik-Net arrays in Japan.

Magnitude saturation

Geller [1976] noted that both the body and surface wave magnitude scales saturate (i.e. after a certain magnitude the M_s and m_b scalings no longer change). This magnitude is reached when the frequency of the wave being used to determine the magnitude (for example a 1s period p-wave in the case of m_b scale) is very high relative to the corner frequency of the earthquake. The point at where the magnitude scaling saturates was defined by Geller [1976] as being a function of the width of the fault, i.e.

$$\omega > \frac{1}{C_w\, L} \tag{3.26}$$

where ω is the frequency, L is the length of the fault (which can in turn be related to the moment using either equation 3.12 or 3.13). C_w is a factor accounting for the fault width W and is defined as:

$$C_w = \frac{Sin(\delta)}{4\alpha} \tag{3.27}$$

with δ denoting the dip of the fault plane, and α is the p-wave velocity (it can also be the s-wave if we are measuring the amplitude of the s-wave). It should be noted that equation 3.27 assumes that $L = 2\,W$, where W is the width. By making this assumption Geller [1976] stated that real data should have a scatter with a factor of 2 in relation to this theoretical source model. Equation 3.26 can be reorganised by substituting the fault length with the moment using equation 3.12 such that:

$$M_o > \frac{\Delta\sigma_s}{(C_w\,\omega)^3} \tag{3.28}$$

where the moment, M_o, can be converted into the magnitude using equation 3.14. It should be noted that the frequency, ω is in radians per second, not Hertz (i.e. 1Hz =6.28318 rad/s). Again using the parameters defined for our kinematic models (i.e. $\Delta\sigma_s$ = 1.5MPa, α = 5.5km/s, $\delta = 90^0$) we can

Obs Window (s)	Lowest Freq. Limit (Hz)	M_{sat}
1	0.25	6.34
2	0.125	6.94
3	0.08325	7.29
4	0.0625	7.55

Table 3.1: The the amplitude with the lowest observable frequency is equal to $\frac{1}{4\,T_{obs}}$ where T_{obs} is the period of the observational window at each station. The frequencies denoted in the second column are the smallest frequencies whose amplitude is observable for a given time window denoted in the first column. M_{sat} is corresponding magnitude after which the magnitude shall suffer from saturation.

now define the possible magnitude at which we should observe magnitude saturation.

Estimating magnitude using the PGD method, the peak amplitude is calculated in the first 1, 2, 3, and 4 seconds after the p-arrival. Let us assume that the lowest observable frequency is defined by $\omega = \frac{1}{4\,T_{obs}}$ where T_{obs} is the observational time window. Therefore the magnitude after which scaling is saturated (M_{sat}) for time windows of 1, 2, 3, and 4 seconds can now be defined as is shown in table 3.1.

In calculating M_{sat} in table 3.1 we have made a number of assumptions the principle being that it is observation window which constrains the lower end of the observable frequency spectra at a seismic station (i.e. not the dynamic range of the seismogram nor the bandpass filtering). This may not be true, with Zollo et al. [2006] stating that the European strong motion dataset had been filtered between 0.25 and 25Hz. It is this assumption that can probably best explain the difference between the M_{sat} values seen in table

3.1 and those seen observationally (i.e. see table 1.2) and using the isochrone modelling (i.e. table 3.5). The broad similarity between the results, however, is encouraging.

3.A Appendix

3.A.1 Isochrone computation

Taking the earthquake nucleation time as $t = 0$, the time for radiation from a point S on the fault to reach a given receiver at R, is the sum of time taken for a rupture to propagate from the hypocenter $\mathbf{x_H}$ to the radiating point $\mathbf{x_S}$ on the fault, plus the time it takes for a seismic wave to travel from $\mathbf{x_S}$ to a given receiver at $\mathbf{x_R}$. Using the Cartesian equivalent of Bernard & Madariaga's Bernard and Madariaga [1984] equation, we define the elapsed time τ as

$$\tau = \frac{\sqrt{(y_R - y_H)^2 + (z_R - z_H)^2}}{v_r} + \frac{\sqrt{(x_R)^2 + (y_S - y_H)^2 + (z_S - z_R)^2}}{\alpha} \quad (3.29)$$

where v_r is a constant rupture velocity and α the velocity of the seismic waves in the homogeneous medium. We have assumed that the fault is vertical and strikes along $x_S = 0$. It should be noted that we shall only be modelling a circular rupture front (constant rupture velocity) for the models presented in the kinematic section. As we are interested in the time elapsed after the first P or S arrival from the hypocenter, we subtract it to obtain:

$$\tau_{iso} = \tau - \tau_{direct} = \tau - \frac{\sqrt{(x_R - x_H)^2 + (y_R - y_H)^2 + (z_R - z_H)^2}}{\alpha} \quad (3.30)$$

By setting τ_{iso} to 1, 2, 3 and 4 seconds, equations 3.29 and 3.30 are solved to obtain the ensemble of points (y_S, z_S) belonging to the isochrone I and compute its length.

3.A.2 Short period radiation

Taking the Haskell fault model in the high frequency approximation (Stein Stein and Wysession [2003]) yields a far field spectral amplitude:

$$\log A(\omega) = \log M_o - \log(T_r T_d/4) - 2\log\omega.$$

Upon replacing the Moment by $M_o = T_d\,\Delta\dot{u}\,\mu\,T_r\,v_r\,W$ ($T_r v_r W$ being the area of the fault, if W is the width of the fault and v_r rupture velocity, while the slip is $T_d\Delta\dot{u}$, where T_d is rise-time), we obtain

$$\log A(\omega) = \log(4\,\Delta\dot{u}\,\mu\,v_r W) - 2\log\omega,$$

showing in the high frequency approximation the far field amplitude does not depend on final slip, but on the slip rate.

3.A.3 Caculating the area encompassed by an isochrone

As the area contained inside an isochrone shall change shape with time (due to the interaction with the fault edge) therefore we shall use formula for calculating the area of a polygon:

$$A = \frac{1}{2} + \sum_{i=0}^{N-1}(x_i\,y_{i+1} - x_{i+1}\,y_i) \tag{3.31}$$

where x, y are coordinate positions defining a 2D polygon and N is the total number of vertices defining the polygon. Note the position (x_0, y_y) =(x_N, y_N).

3.A.4 Tables

Table 3.2: Velocity model used for isochrone projection.

	v_p (km/s)	v_s (km/s)	v_r (km/s)
Model 1	5.5	3.18	2.5
Model 2	4.5	2.6	2.1

Table 3.3: Fault dimensions for square and rectangular fault shapes used for isochrone modeling

M_L	Square Fault (km)	Rectangular Fault (km)
4.0	0.94 x 0.94	0.94 x 0.94
4.3	1.3 x 1.3	1.3 x 1.3
4.6	1.9 x 1.9	1.9 x 1.9
4.9	2.67 x 2.67	2.67 x 2.67
5.2	3.76 x 3.76	3.76 x 3.76
5.5	5.3 x 5.3	5.3 x 5.3
5.8	7.49 x 7.49	7.49 x7.49
6.1	10.58 x 10.58	10.58 x 10.58
6.4	14.95 x14.95	14.95 x14.95
6.7	21.12 x 21.12	15 x 792
7.	29.83 x 29.83	15 x 1330
7.3	42.13 x 42.13	15 x 2233
7.6	59.5 x 59.5	15 x 3749

Table 3.4: Best fit parameters for the results displayed in figure 3.7. The results are for p-waves where the media has a velocity of 4.5km/s. The best fit curve is defined as: $\log_{10}(PGD) = \mathrm{m}\, M_L + c$ where m is the slope and c being the y-intercept. In all cases the results relate to 2 seconds of recorded ground motion. Std dev is the standard deviation and M_{Sat} is the magnitude at which we see a saturation in our scaling.

Fault Type	Model	m	c	M_{Sat}	Std. Dev.
Rectangle	A	0.918	-11.3	7.3	0.059
	B	0.899	-7.73	5.8	0.05
	C	0.46	-8.78	6.4	0.047
Square	A	0.932	-11.37	7.0	0.057
	B	0.835	-7.43	6.1	0.098
	C	0.47	-8.83	6.4	0.032

Table 3.5: Best fit parameters for a square fault as displayed in figure 3.8. The results are for p-waves where the media has a velocity of 4.5km/s. The best fit curve is defined as: $\log_{10}(PGD)$ =m $M_L + c$ where m is the slope and c being the y-intercept. Std dev is the standard deviation and M_{Sat} is the magnitude at which we see a saturation in our scaling.

Time (sec)	m	c	M_{Sat}	Std. Dev.
1	0.456	-8.76	5.8	0.032
2	0.474	-8.83	6.4	0.032
3	0.479	-8.85	7.0	0.0326
4	0.503	-8.96	7.0	0.018

Table 3.6: Best fit parameters for a square fault as displayed in figure 3.11. The first two rows are for p-waves (with a velocity of 4.5 km/s) whilst the last two rows are for s-waves (with with velocities of 2.6km/s). The best fit curve is defined as: $\log_{10}(PGD)$ =m $M_L + c$ where m is the slope and c being the y-intercept. Std dev is the standard deviation and M_{Sat} is the magnitude at which we see a saturation in our scaling.

Time (sec)	Wave Type	m	c	M_{Sat}	Std. Dev.
1	P	0.456	-8.76	5.8	0.032
2	P	0.474	-8.83	6.4	0.032
1	S	0.447	-8.74	6.4	0.026
2	S	0.487	-8.9	6.7	0.045

3.A.5 Supplementary Figures

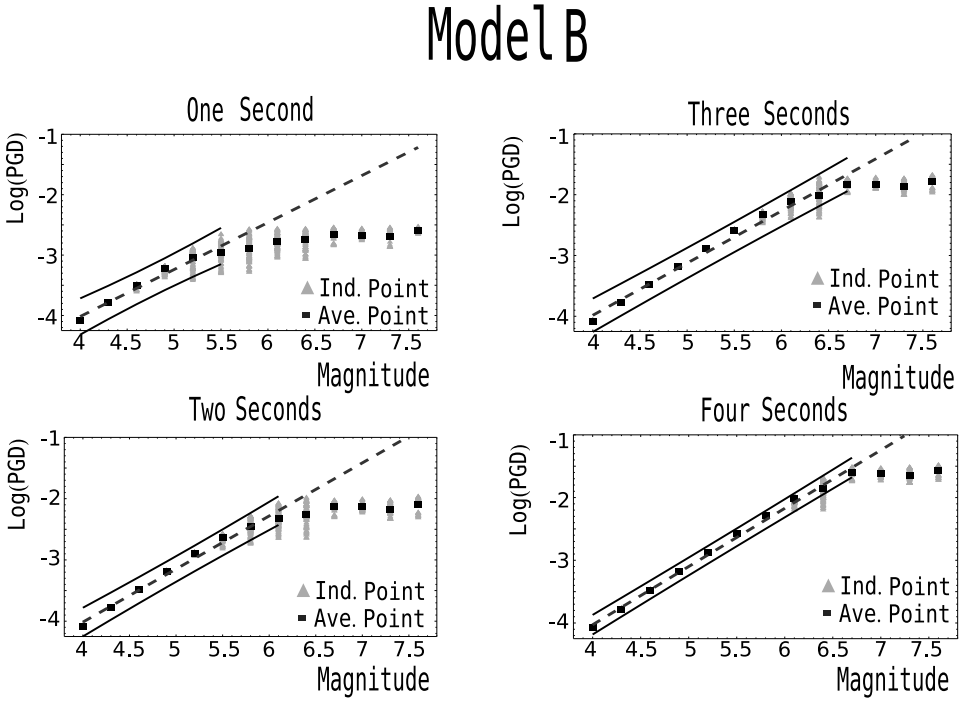

Figure 3.19: This figure depicts the evolution of scaling using model B over one to four seconds and is similar to Figure 3.8 in text. This catalogue is for a rectangular fault with p-wave velocity of 5.5 km/s. Grey triangles represent individual peak ground displacement readings for stations. Black squares depict the average peak ground displacement with the black dashed line representing the best fit curve through the black squares. The thin black lines either side of the best fit lines are 95% confidence curves for the best fit lines based on the average (i.e. square) values.

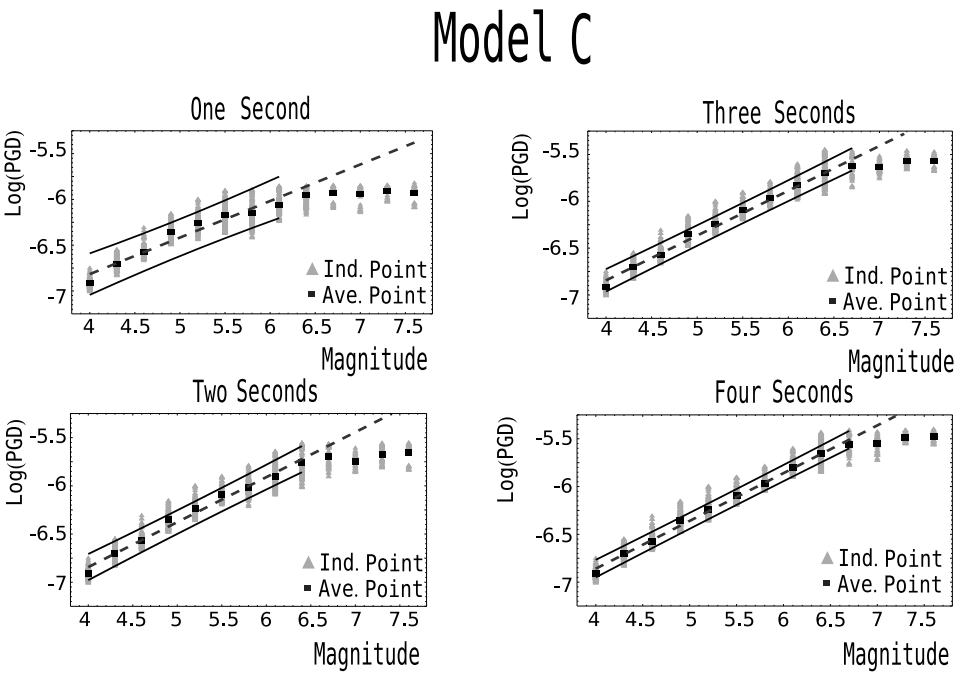

Figure 3.20: This figure depicts the evolution of scaling using model C over one to four seconds and is similar to Figure 3.8 in text. This catalogue is for a rectangular fault with p-wave velocity of 5.5 km/s. Grey triangles represent individual peak ground displacement readings for stations. Black squares depict the average peak ground displacement with the black dashed line representing the best fit curve through the black squares. The thin black lines either side of the best fit lines are 95% confidence curves for the best fit lines based on the average (i.e. square) values.

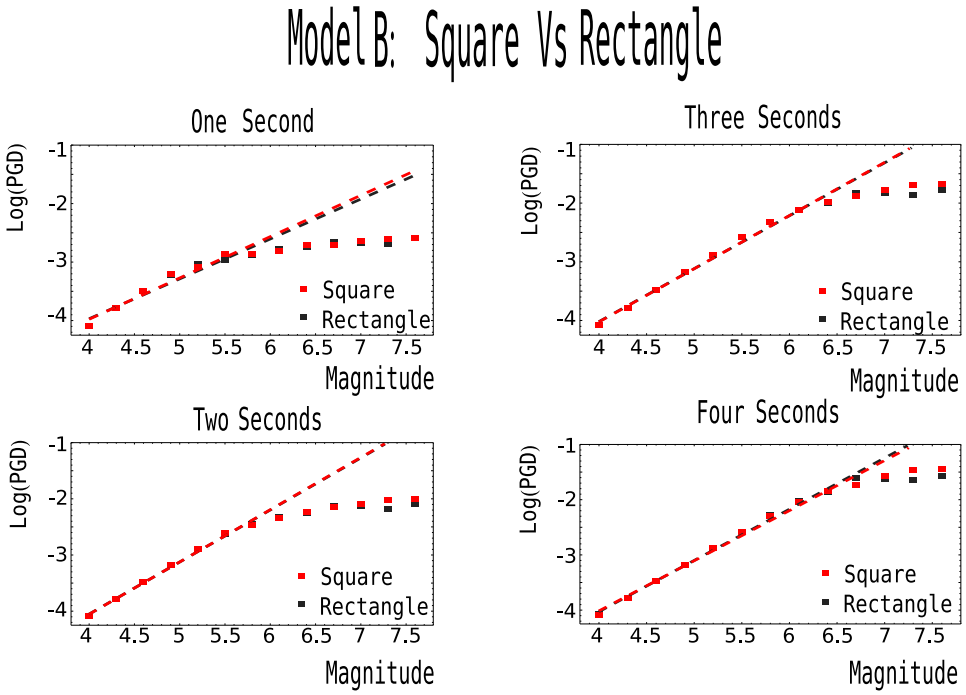

Figure 3.21: This figure depicts the difference between the average peak displacement between square and rectangular faults using Model B for observational time windows of 1 to 4 seconds. P-wave velocity is set at 5.5km/s. Black and red box symbols depict the average PGD for rectangular and square fault types. Black and red dashed lines denote best fit line for magnitude scaling for rectangular and square faults respectively

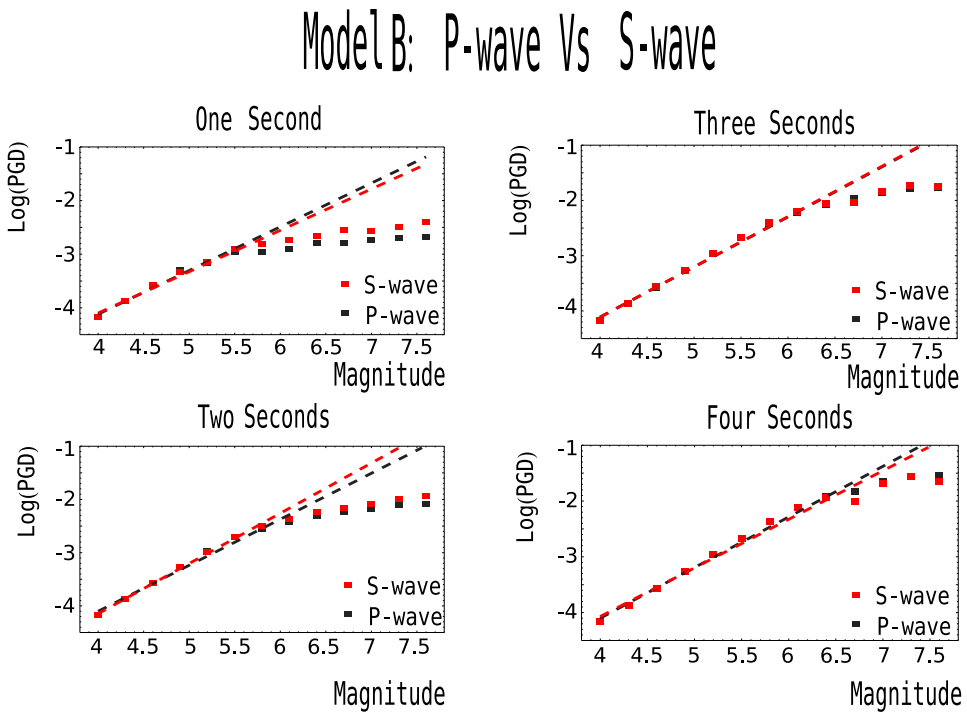

Figure 3.22: For this figure the squares denote the average PGD (i.e. the same values denoted by black squares in earlier plots). Dashed lines are linear best fit lines for the two datasets. Black denotes p-wave values and red s-wave. From the four graphs we can see that s-waves produce larger PGD due to the fact that they cover a larger area of the fault plane. This difference in isochrone size between the two wave types means that the magnitude scaling using s-wave PGD has a slightly larger magnitude range than p-wave PGD. Model B is the kinematic model used for these graphs. P-wave velocity is set at 4.5km/s while the S-wave velocity is 2.6km/s.

Chapter 4

Conclusion

4.1 General Discussion

Initially we proposed two possible explanations for the magnitude scaling with PGD in the initial few seconds of particle motion. The first being that earthquakes contain more deterministic features than had previously been expected, the second being that scaling was a result of radiation from a moving source. Whilst our dynamic modelling discounted the possibility of applying our deterministic hypothesis over a large magnitude range, our kinematic assumptions proved more realistic. Indeed the catalogues produced by our kinematic models provided a similar match, in terms of scaling to the observational ones. The scatter in our catalogues is a lot less than their data derived analogues due to our assumption of homogeneous medium and the implicit averaging in simplified equations (3.7, 3.9,3.10). The introduction of heterogeneous velocity layers, directivity effect, radiation patterns, and site conditions would, we believe, induce a much larger scatter in our synthetic catalogues whilst the underlying kinematic scaling should remain.

It is interesting to remark that in models B and C, the slope of particle displacement versus moment magnitude differs. The difference in slope is

essentially due to the area-scaling of radiation in model B as opposed to the circumference-scaling in model C. We recall that models B and C assume that the frequency of observation is relatively low and high, respectively. By analogy, the different slope may be compared and qualitatively understood also in terms of Aki ω-square model of spectral amplitude Aki [1967], which differs whether the frequency is above or below corner frequency w_o. To rapidly illustrate this, we examine the amplitude spectrum of a Haskell earthquake source in section 3.8.2 from which we produced equation 3.23. Looking at the change in amplitude over a magnitude range for an observational frequency near that of the common corner frequency (i.e. $\omega \approx 1Hz$) we observe this change in scaling slope with increasing magnitude. On re-examining observational catalogues, this change in slope is observable, however most authors ignore it (Zollo et al. [2007]) or mis-interpret it (Rydelek et al. [2007]).

It should be noted that whilst we do not define a corner frequency per se in equation 3.23 it is represented by our piecewise term defined in the interval $\frac{2}{T_R} < \omega < \frac{2}{T_D}$. One principle assumption that is made with equation 3.23 however is that the source features (i.e. stress drop, rupture velocity, etc) is the same over the whole observational catalogue. Whilst this is unlikely, earthquakes in similar geographical regions shall be influenced by similar conditions (e.g. stresses) therefore their corner frequencies should be broadly similar. This would imply that there are subtle differences between observational catalogues from different tectonic regions. Therefore some "tuning" maybe required for different EEW systems if the PGD is to be used in magnitude estimation.

In effect, the PGD method can be viewed as a very efficient calculation of the body wave magnitude (m_b). This is due to the fact that the PGD method takes the average largest amplitude over a range of stations for a limited time window as opposed to the m_b method which waits until the end of the body wave coda and then determines the peak displacement. Hence, like m_b

scaling, PGD suffers from saturation and large magnitudes, a feature seen both observationally and in our isochrone modelling. If magnitude saturation is due to isochrone interaction as is suggested by our synthetic catalogues this would imply that the PGD method becomes insufficient for determining very large earthquakes (i.e. $> 7M$), even with extended time windows (recall the discussion in section 3.8.1)

This is unless there is a deterministic parameter in the PGD which would naturally increase the range seen in our kinematic catalogues (i.e. Models B and C). In chapter 2, our dynamic modelling showed that for a very simple asperity model there is a relationship between the asperity where nucleation occurs and final magnitude. This scaling however is limited to a narrow magnitude range (i.e. $1.5M_w$) after which rupture cessation is dependent on external influences (for e.g. geometric barriers) – recall figures 2.12 and 2.9. An encouraging feature in terms of magnitude estimation is the similarity in slopes between the deterministic scaling and the kinematic ones (compare tables 2.1 and 3.4). Therefore there is the possibility that scaling may be slightly extended from a kinematic to a deterministic pretext. Indeed model A included a deterministic feature as it assumed scaling with slip δu and thus created a synthetic catalogue with a larger scaling range (recall figure 3.7).

This is based on the assumption that earthquake faults are smooth. With the introduction of a heterogeneous pre-stress distribution outside of the asperity we saw the sensitivity of rupture termination to local pre-stress conditions on the fault plane (recall figure 2.14). Therefore the implications for rupture physics would mean that faults are relatively smooth with large heterogeneities more likely to be located at or near the point of nucleation. Lewis and Ben-Zion [2007] hypothesised that this would need to be the case in order to create deterministic faults, however they noted that fracture interaction geometric barriers and the free surface would dramatically affect such scaling. In the case of geometric barriers rupture can be stopped pre-

maturely whilst rupture interaction with the free surface can produce large slip rates (and hence large particle displacements).

If we may account for these features using a probabilistic framework this leaves us with the assumption that earthquakes occur on smooth fault planes (i.e. fault planes where pre-stress heterogeneity is small). This may be the case for small earthquakes which contain at most one asperity (i.e. $< 6M$), however very large earthquakes (i.e. $> 8M$) are more complex containing a number of asperities and/or barriers. Taking the 2004 Great Sumatra-Andaman earthquake the peak moment rate occurred 40-60s after nucleation with the rupturing of a relatively strong patch of the fault, the moment rate beforehand was quite small (Ammon et al. [2005]). In the case of the $8.4M_w$ 2001 Peruvian earthquake a barrier ruptured $\approx 36s$ after initiation (Robinson et al. [2006]), this rupturing of such a strong patch greatly increased the size of the earthquake. In both these examples the moment rate in the first few seconds of rupture could not not predict the subsequent final size of these events as the large injection of elastostatic energy occurred only in the later stages of an earthquake evolution. This would appear to discount the possibility of very large earthquakes being deterministic.

This leaves leaves us with small and intermediate earthquakes. Small earthquakes (i.e. $< 5.5M$), as shown by chapter 3, have already stopped rupture when their magnitude is determined by EEW systems. Therefore the deterministic nature is unimportant for EEW systems. Intermediate earthquakes (i.e. greater than $6M$ but less than $7.5M$) on the other hand may still be rupturing. As intermediate earthquakes involve rupture which does not cause failure in large strong patches on faults they may still be heavily influenced by nucleation conditions. In such a case the previously discussed "smooth fault" criterion for rupture determinism maybe acceptable. Another possible mechanism whereby rupture could show deterministic features is where the pre-stress is distributed in a systematic way. An example of such

a process is the static stress transfer observed from one rupturing fault to neighbouring ones. This process has been observed to cause neighbouring faults to rupture sometime in the future (see Nalbant et al. [2005] and Stein [1999]). Cotton and Coutant [1997] noted that the static stress transferred decreased by a factor between between r^{-2} and r^{-1}, where r is distance from the ruptured fault. Therefore stress transfer automatically creates a grading in the pre-stress distribution over the next unruptured branch of a fault chain. This could be a point for future study as to whether such a pre-stress distribution is meaningful in terms of deciding an intermediate earthquakes size.

4.2 Conclusion

In summary, we can say that the scaling between magnitude and PGD is best explained as a kinematic feature with the possibility of a deterministic influence over this scaling being limited. It should be noted this report has focused on solely on the PGD method for rapid magnitude estimation. Future work in real time magnitude estimation could entail investigating the mechanism behind the τ_p scaling.

In terms of whether earthquakes are deterministic the question is still an open one regarding small and intermediate earthquakes. Whilst our numerical modelling has clarified the situations whereby earthquakes may be deterministic, more work needs be done in this field. For example relating the events for more complete, realistic source models with seismograms in the near, intermediate and far field, with a complex source history and full wavefield radiation.

Bibliography

Rachel E. Abercrombie. Earthquake source scaling relationships from -1 to 5 m_l using seismograms recorded at 2.5-km depth. *Journal of Geophysical Research*, 100(B12):24015–24036, 1995.

K. Aki. Generation and propagation of g waves from the niigata earthquake of june 16, 1964. part2: Estimation of earthquake moment, released energy, and stress-strain drop from the g wave spectrum. *Bull. Earthq. Res. Inst. Tokyo Univ.*, 44:73–88, 1966.

Keiiti Aki. Scaling law of seismic spectrum. *Journal of Geophysical Research*, 72(4):1217–1231, 1967.

Keiiti Aki and Paul G. Richards. *Quantitative Seismology*. University Science Books, 2nd edition, 2002.

Richard Allen. The elarms earthquake early warning methodology and application across california. In P. Gasparini, G. Manfredi, and J. Zschau, editors, *Earthquake Early Warning*, chapter 3, pages 21–43. Springer, 2007.

Richard M. Allen and Hiroo Kanamori. The potential for earthquake early warning in southern california. *Science*, 300:786–789, 2003.

Charles J. Ammon, Chen Ji, Hong-Kie Thio, David Robinson, Sidao Ni, Vala Hjorleifsdottir, Hiroo Kanamori, Thorne Lay, Shamita Das, Don Helmberger, Gene Ichinose, Jascha Polet, and David Wald. Rupture process

of the 2004 sumatra-andaman earthquake. *Science*, 308:1133–1139, 2005. doi: 10.1126/science.1112260.

D. J. Andrews. Rupture velocity of plane strain shear cracks. *J. Geophys. Res.*, 81:5679–5687, 1976a.

D. J. Andrews. A stochastic fault model 1. static case. *Journal of Geophysical Research*, 85(B7):3867–3877, 1980.

D. J. Andrews and Y. Ben-Zion. Wrinkle-like slip pulse on a fault between different materials. *J. Geophys. Res.*, 102, No. B1:553–571, 1997.

D.J. Andrews. Rupture propagation with finite stress in antiplane strain. *J. Geophys. Res.*, 81(20):3575–3582, 1976b.

N. M. Beeler, T.-F. Wong, and S. H. Hickman. Short notes on the expected relationships among apparent stress, static stress drop, effective shear fracture energy, and efficiency. *Bulletin of the Seismological Society of America*, 93:1381–1389, 2003.

Y. Ben-Zion and D. J. Andrews. Properties and implications of dynamic rupture along a material interface. *BSSA*, 88, No. 4:1085–1094, 1998.

Jean-Pierre Berenger. Three-dimensional perfectly matched layer for the absorption of electromagnetic waves. *Journal of Computational Physics*, 127:363–379, 1996.

P. Bernard and R. Madariaga. A new asymptotic method for the modeling of near-field accelerograms. *BSSA*, 74:539–557, 1984.

Gregory C. Beroza and William L. Ellsworth. Properties of the seismic nucleation phase. *Tectonophysics*, 261:209–227, 1996.

Bruce A Bolt. *Earthquakes and geological discovery.* Scientific American Library, 1993.

Michel Bouchon. A simple method to calculate green's functions for elastic layered media. *BSSA*, 71(4):959–971, 1981.

Johana Brokesova. *Asymptotic ray method in seismology: a tutorial.* Matfyz Press, 2006.

W. Chew and Q. H. Liu. Perfectly matched layers for elastodynamics: a new absorbing boundary condition. *JCA*, 4:341–359, 1996. PML boundary conditions.

F. Cotton and M. Campillo. Frequency domain inversion of strong motions: Application to the 1992 landers earthquake. *Journal of Geophysical Research*, 100(B3):3961–3975, 1995.

Fabrice Cotton and Olivier Coutant. Dynamic stress variations due to shear faults in a plane-layered medium. *Geophys. J. Int.*, 128:676–688, 1997.

Georgia Cua and Thomas Heaton. The virtual seismologist (vs) method: a bayesian approach to earthuake early warning. In Paolo Gasparini, Gaetano Manfredi, and Jochen Zschau, editors, *Earthquake Early Warning Systems*, chapter 7, pages 97–132. Springer, 2007.

S. Das and B. V. Kostrov. Breaking of a single asperity: Rupture process and seismic radiation. *Journal of Geophysical Research*, 88(B5):4277–4288, 1983.

Shamita Das and Keiiti Aki. A numerical study of two-dimensional spontaneous rupture propagation. *Geophys. J. R. astr. Soc*, 50:643–668, 1977.

Steven M. Day. Three-dimensional simulation of spontaneous rupture: the effect of nonuniform prestress. *Bulletin of the Seismological Society of America*, 72(6):1881–1902, 1982.

James H. Dieterich. Modeling of rock friciton: 1. experimental results and constituive equations. *Journal of Geophysical Research*, 84(B5):2161–2168, 1979. Have a hard copy of this First proposition of velocity weakening friction law.

Douglas Dreger and Anastasia Kaverina. Seismic remote sensing for the earthquake source process and near-source strong shaking: A case study of the october 16, 1999 hector mine earthquake. *Geophyical Research Letters*, 27(27):1941–1944, 2000.

Eric M. Dunham. Conditions governing the occurrence of supershear ruptures under slip-weakening friction. *Journal of Geophysical Research*, 112 (B07302), 2007. doi: 10.1029/2006JB004717.

Eric M. Dunham, Pascal Favreau, and J. M. Carlson. A supershear transition mechanism for cracks. *Science*, 299:1557–1559, 2003. doi: 10.1126/science.1080650.

A. M. Dziewonski, T. A. Chou, and J. H. Woodhouse. Determination of earthquake source parameters from waveform data for studies of global and regional seismicity. *Journal of Geophysical Research*, 86:2825–2852, 1981.

G. Ekstrom. Rapid earthquake analysis utilizes the internet. *Computers in Physics*, 8:632–638, 1994.

W. L. Ellsworth and G. C. Beroza. Seismic evidence for an earthquake nucleation phase. *Science*, 268:851–855, 1995.

Antonio Emolo and Aldo Zollo. Kinematic source parameters for the 1989 loma prieta earthquake from the nonlinear inversion of accelerograms. *BSSA*, 95(3):981–994, 2005. doi: 10.1785/0120030193.

J. Eshelby. The determination of the elastic field of an ellipsoidal inclusion and related problems. *Proc. Roy. Soc. London, Series A*, 241:376–396, 1957.

G. Festa and S. Nielsen. Pml absorbing boundaries. *BSSA*, 93:891–903, 2003.

Eiichi Fukuyama and Raul Madariaga. Integral equation method for plane crack with artbitrary shape in 3d elastic medium. *BSSA*, 85, No. 2:614–628, 1995.

Eiichi Fukuyama and Raul Madariaga. Dynamic propagation and interaction of rupture front on a planar fault. *Pure Applied Geophysics*, 157:1959–1979, 2000.

Eric L. Geist, Vasily V. Titov, Diego Arcas, Fred F. Pollitz, and Susan L. Bilek. Implications of the 26 december 2004 sumatra-andamn earthquake on tsunami forecast and assessment models for great subduction-zone earthquakes. *BSSA*, 97(1A):S249–S270, 2007.

Robert J Geller. Scaling relations for earhquake source parameters and magnitudes. *BSSA*, 66(5):1501–1532, 1976.

Domenico Giardini, Gottfried Grunthal, Kaye M. Shedlock, and Peizhen Zhang. The gshap global seismic hazard map. *Annali di Geofisica*, 42 (6):1225–1230, 1999.

Veronica F. Grasso, James L. Beck, and Gaetano Manfredi. Seismic early warning systems: procedure for automated deciscion making. In P. Gasparini, G. Manfredi, and j. Zschau, editors, *Earthquake Early Warning Systems*, chapter 10. Springer, 2007.

Robert W. Graves. Simulating wave propagation in 3d elastic media using staggered-grid finite differences. *Bulletin of the Seismological Society of America*, 86(4):1091–1106, 1996.

Robert W. Graves and David J. Wald. Observed and simulated ground motions in the san bernardino basin region for the hector mine, california, earthquake. *Bulletin of the Seismological Society of America*, 94(1):131–146, 2004.

David Gubbins. *Time series analysis and inverse theory for geophysicists*. Cambridge University Press, 2004.

T. C. Hanks and H. Kanamori. A moment-magnitude scale. *Journal of Geophysical Research*, 84:2348–2352, 1979.

Stephen H. Hartzell and Thomas H. Heaton. Inversion of strong ground motion and teleseismic waveform data for the fault rupture history of the 1979 imperial valley, california, earthquake. *BSSA*, 73(6):1553–1583, 1983.

N. A. Haskell. Total energy and energy spectral density of elastic wave radiation from propagating faults. *BSSA*, 54(6):1811–1841, 1964.

Thomas H. Heaton. Evidence for and implications of self-healing pulses of slip in earthquake rupture. *Physics of the Earth and Planetary Interiors*, 64:1–20, 1990. URL `http://heaton.caltech.edu/`.

A. Herrero and P. Bernard. A kinematic self-similar rupture process for earthquakes. *Bulletin of the Seismological Society of America*, 84 (No. 4): 1216–1228, 1994.

G. Hillers, P. M. Mai, Y. Ben-Zion, and J.-P. Ampuero. Statistical properties of seismicity of fault zones at different evolutionary stages. *Geophysical Journal International*, 169:515–533, 2007. doi: 10.1111/j.1365-246X.2006.03275.

Shigeki Horiuchi, Hiroaki Negishi, Kana Abe, Aya Kamimura, and Yukio Fujinawa. An automatic processing system for broadcasting earthquake alarms. *Bulletin of the Seismological Society of America*, 95:708–718, 2005. doi: 10.1785/0120030133.

Yoshiaki Ida. Cohesive force across the tip of a longitudinal-shear crack and griffith's specific surface energy. *J. Geophys. Res.*, 77(20):3796–3805, 1972.

Iunio Iervolino, Vincenzo Convertito, Massimiliano Giorgio, Gaetano Manfredi, and Aldo Zollo. The crywolf issue in earthquake early warning applications for the campania region. In P. Gasparini, G. Manfredi, and J. Zschau, editors, *Earthquake Early Warning Systems*, chapter 11. Springer, 2007.

Yoshihisa Iio. Observations of the slow initial phase generated by microearthquakes: Implications for earthquake nucleation and propagation. *Journal of Geophysical Research*, 100(B8):15333–15349, 1995.

H. Jeffreys and B. S. Jeffreys. *Methods of Mathematical Physics*. Cambridge University Press, 3rd edition, 1972.

H. Kanamori. The energy release in great earthquakes. *Journal of Geophysical Research*, 82:2981–2987, 1977.

Hiroo Kanamori. Real-time seismology and earthquake damage mitigation. *Annu. Rev. Earth Planet Sci.-214*, 33:195, 2005. doi: 10.1146/annurev.earth.33.092203.122626.

Hiroo Kanamori and Luis Rivera. Static and dynamic scaling relations for earthquakes and their implications for rupture speed and stress drop. *BSSA*, 94, No. 1:314 –319, 2004.

Richard A Kerr. Earthquake forcast endorsed. *Science*, 228:311, 1985.

Richard A. Kerr. Seismologists issue a no-win earthquake warning. *Science*, 258:742–743, 1992a.

Richard A. Kerr. Good forcast, but missed prediction. *Science*, 258:743, 1992b.

D. Kilb and J. Gomberg. The initial subevent of the 1994 norhridge, california earthquake: Is earthquake size predictable? *Journal of Seismology*, 3:409–420, 1999.

Dimitri Komatitsch, Jean-Pierre Vilotte, Rossana Vai, Jose M. Castillo-Covarrubias, and Francisco J. Sanchez-Sesma. The spectral element method for elastic wave equations - application to 2-d and 3-d seismic problems. *International Journal for Numerical Methods in Engineering*, 45:1139–1164, 1999.

B. V. Kostrov. Self-similar problems of propagation of shear cracks. *J. Appl. Math. Mech.*, 28:1077–1087, 1964.

Thorne Lay and Terry C. Wallace. *Modern Global Seismology*, volume 58 of *International Geophysics Series*. Academic Press, 1995.

M. A. Lewis and Y. Ben-Zion. Examination of scaling between proposed early signals in p waveforms and earthquake magntiude. *Geophys. J. Int.*, 171:1258–1268, 2007. doi: 10.1111/j.1365-246X.2007.03591.x.

Ta liang Teng, Ludan Wu, Tzay-Chyn Shin, Yi-Ben Tsai, and William H. K. Lee. One minute after: Strong-motion map, effective epicenter, and effective magnitude. *Bulletin of the Seismological Society of America*, 87(5): 1209–1219, 1997.

R. Madariaga and K. B. Olsen. Theoretical seismology. In *International Handbook of Seismology and Physics of the Earth's Interior, Part A*, pages 175–194. Academic Press, 2002.

R. Madariaga, K. Olsen, and R. Archuleta. Modeling dynamic rupture in a 3d earthquake fault model. *Bulletin of the Seismological Society of America*, 88(5):1182–1197, 1998.

Raul Madariaga. Dynamics of an expanding circular fault. *Bulletin of the Seismological Society of America*, 66(3):639–666, 1976.

Raul Madariaga. High frequency radiation from dynamic earthquake fault models. *Annales Geophysicae*, 1(1):17–23, 1983.

Raul Madariaga and Kim B. Olsen. Criticality of rupture dynamics in 3d. *Pure and Applied Geophysics*, 157:1981–2001, 2000. doi: 10.1007/PL00001071.

P. Martin Mai, P. Spudich, and J. Boatwright. Hypocenter locations in finite-source rupture models. *BSSA*, 95:965–980, 2005. doi: 10.1785/0120040111.

Jeffrey J. McGuire, Li Zhao, and Thomas H. Jordan. Predominance of unilateral rupture for a global catalog of large earthquakes. *BSSA*, 92:3309–3317, 2002.

Jim Mori and Hiroo Kanamori. Initial rupture of earthquakes in the 1995 ridgecrest, california sequence. *Geophysical Resarch Letters*, 23:2437–2440, 1996.

Y. Nakamura. On the urgent earthquake detection and alarm system (uredas). In *Proceedure of the 9th World Conference on Earthquake Engineering*, 1988.

Yutaka Nakamura and Jun Saita. Uredas, the earthquake warning system: Today and tomorrow. In Paolo Gasparini, Gaetano Manfredi, and Jochen Zschau, editors, *Earthquake Early Warning Systems*, chapter 13, pages 249–282. Springer, 2007.

Suleyman S. Nalbant, Sandy Steacy, Kerry Sieh, Danny Natawidjaja, and John McCloskey. Earthquake risk on the sunda trench. *Nature*, 434:756–757, 2005. doi: 10.1038/nature435756a.

S. Nielsen and R. Madariaga. On the self-healing fracture model. *BSSA*, 93 (6):2375–2388, 2003.

Stefan Nielsen. Can earthquake size be controlled by the initial seconds of rupture? In Paolo Gasparini, Gaetano Manfredi, and Jochen Zschau, editors, *Earthquake Early Warning Systems*, chapter 2, pages 9–20. Springer, 2007.

Stefan B. Nielsen and J. M. Carlson. Rupture pulse characterization: Self-healing, self-similar, expanding solutions in a continuum model of fault dynamic. *BSSA*, 90, No. 6:1480–1497, 2000.

Stefan B. Nielsen and Kim B. Olsen. Constraints on stress and friction from dynamic rupture models of the 1994 northridge, california earthquake. *Pure and Applied Geophysicss*, 157:2029–2046, 2000.

Dennis Normile. Some countries are bettig that a few seconds can save lives. *Science*, 306(5704):2178–2179, 2004. doi: 10.1126/science.306.5704.2178.

Erik L. Olson and Richard M. Allen. The deterministic nature of earthquake rupture. *Nature*, 438:212–215, 2005. doi: 10.1038/nature04214.

Morgan T. Page, Eric M. Dunham, and J. M. Carlson. Distinguishing barriers and asperities in near-source ground motion. *Journal of Geophysical Research*, 110, 2005. doi: 10.1029/2005JB003736.

S. Peyrat and K. B. Olsen. Nonlinear dynamic rupture inversion of the 2000 western tottori, japan, earthquake. *Geophysical Research Letters*, 31 (L05604), 2004. doi: 10.1029/2003GL019058.

H.r Quin and Shamita X. Das. A hybrid boundary integral equation method for the computation of source time functions for 3-d rupture propagation. *Geophysical Journal*, 96:163–177, 1989.

Leon Reiter. *Earthquake hazard analysis*. Columbia University Press, 1991.

James R. Rice, Charles G. Sammis, and Robert Parsons. Off-fault secondary failure induced by a dynamic slip pulse. *BSSA*, 95, No. 1:100–134, 2005. doi: 10.1785/0120030166.

Charles F. Richter. An instrumental earthquake magnitude scale. *BSSA*, 25 (1):1–32, 1935.

J. Ripperger, J.-P. Ampuero, P. M. Mai, and D. Giardini. Earthquake source characteristics from dynamic rupture with constrained stochastic fault stress. *Journal of Geophysical Research*, 112(B04311), 2006. doi: 10.1029/2006JB004515.

D. P. Robinson, S. Das, and A. B. Watts. Earthquake rupture stalled by a subducting fracture zone. *Science*, 312:1203–1205, 2006. doi: 10.1126/science.1125771.

Andy Ruina. Slip instablity and state variable friction law. *Journal of Geophysical Research*, 88(B12):10359–10370, 1983. Have a hard copy Introduces rate and state friction law.

P. Rydelek and S. Horiuchi. Is earthquake rupture deterministic? *Nature*, 442, 2006. doi: 10.1038/nature04963.

Paul Rydelek and Jose Pujol. Real-time seismic warning with a two-station subarray. *Bulletin of the Seismological Society of America*, 94(4):1546–1550, 2004.

Paul Rydelek, Changjiang Wu, and Shigeki Horiuchi. Comment on "earthquake magntiude estimation from peak amplitudes of very early seismic signals on strong motion records" by aldo zollo, maria lancieri, and stefan nielsen. *Geophysical Research Letters*, 34(L20302), 2007. doi: 10.1029/2007GL029387.

Tamao Sato and Hiroo Kanamori. Beginning of earthquakes modeled with the griffith's fracture criterion. *Bulletin of the Seismological Society of America*, 89(1):80–93, 1999.

Claudio Satriano, Anthony Lomax, and Aldo Zollo. Optimal, real-time earhquake location for early warning. In P. Gasparini, G. Manfredi, and J. Zschau, editors, *Earthquake Early Warning Systems*. Springer, 2007.

Frank Scherbaum and Marie-Paule Bouin. Fir filter effects and nucleation phases. *Geophys. J. Int.*, 130:661–668, 1997.

C. H. Scholz. Scaling relationships for strong ground motion in large earthquakes. *BSSA*, 72(6):1903–1909, 1982.

Christopher H. Scholz. *The Mechanics of Earthquakes and Faulting*. Cambridge, 2 edition, 2003.

Dario Slejko, Laura Perussa, and Alessandro Rebez. Seismic hazard maps of italy. *Annali di Geofisica*, 41(2):183–214, 1998.

Paul Spudich and L. Neil Frazer. Use of ray theory to calculate high-frequency radiation from earthquake sources having spatially variable rupture velocity and stress drop. *BSSA*, 74:2061–2082, 1984.

Sandra J. Steacy and John McCloskey. What controls an earthquakes size? results from a heterogeneous cellular automaton. *Geophys. J. Int.*, 133: F11–F14, 1998.

Ross S. Stein. The role of stress transfer in earthquake occurence. *Nature*, 402:605–609, 1999.

Seth Stein and Micheal Wysession. *An introduction to seismology, earthquakes, and earth structure*. Blackwell Publishing, 2003.

T. Tada, E. Fukuyama, and R. Madariaga. Non-hypersingular boundary integral equations for 3-d non-planar crack dynamics. *Computational Mechanics*, pages 613–626, 2000.

Louisa L. H. Tsang, Richard M. Allen, and Gilead Wurman. Magnitude scaling relations from p-waves in southern california. *Geophysical Research Letters*, 34(L19304), 2007. doi: 10.1029/2007GL031077.

Seiji Tsuboi. Application of m_{wp} to tsunami earthquake. *Geophysical Research Letters*, 27(19):3105–3108, 2000.

Jean Virieux. P-sv wave propagation in heterogeneous media: Velocity-stress finite-difference methdo. *Geophysics*, 51(4):886–901, 1986.

Jean Virieux and Raul Madariaga. Dynamic faulting studied by a finite difference method. *Bulletin of the Seismological Society of America*, 72(2): 345–369, 1982.

D. J. Wald, V. Quitoriano, T. H. Heaton, and H. Kanamori. Trinet "shakemaps": rapid generation of peak ground motion and intensity maps for earthquakes in southern california. *Earthquake Spectra*, 15:537–55, 1999a.

David J. Wald, Vincent Quitoriano, Thomas H. Heaton, and Hiroo Kanamori. Relationships betweent peak ground acceleration, peak ground velocity, and modified mercalli intensity in california. *Earthquake Spectra*, 15(3):557–564, 1999b.

Kelin Wang, Qi-Fu Chen, Shihong Sun, and Anong Wang. Predicting the 1975 haicheng earthquake. *BSSA*, 96(3):757–795, 2006. doi: 10.1785/0120050191.

Emanuel Weber, Giovanni Iannaccone, Aldo Zollo, Antonella Bobbio, Luciana Cantore, Margherita Corciulo, Vincenzo Convertito, Martino Di Crosta, Luca Elia, Antonio Emolo, Claudio Martino, Annalisa Romeo, and Claudio Satriano. Development and testing of an advanced monitoring infrastructure (isnet) for seismic early-warning applications in the campania region of southern italy. In Paolo Gasparini, Gaetano Manfredi, and Jochen Zschau, editors, *Earthquake Early Warning System*, chapter 16, pages 325–342. Springer, 2007.

Steven G. Wesnousky. Predicting the endpoints of earthquake ruptures. *Nature*, 444, 2006. doi: 10.1038/nature05275.

Martin Wieland, Lothar Griesser, and Christoph Kuendig. Seismic early warning system for a nuclear power plant. In *12 Word Conference on Earthquake Engineering*, 2000.

Yih-Min Wu and Hiroo Kanamori. Experiment on an onsite early warning method for the taiwan early warning system. *BSSA*, 95(1):347–353, 2005.

Yih-Min Wu and Li Zhao. Magnitude estimation using the first three seconds p-wave amplitude in earthquake early warning. *Geophysical Research Letters*, 33, 2006. doi: 10.1029/2006GL026871.

Yih-Min Wu, Hsin-Yi Yen, Li Zhao, Bor-Shouh Huang, and Wen-Tzong Liang. Magnitude determination using initial p waves: A single-station approach. *Geophysical Research Letters*, 33, 2006. doi: 10.1029/2005GL025395.

Gilead Wurman, Richard M. Allen, and Peter Lombard. Toward earthquake early warning in northern california. *Journal of Geophysical Research*, 112 (B08311), 2007. doi: 10.1029/2006JB004830.

Gutuan Zheng and James R. Rice. Conditions under which velocity-weakening friction allows a self-healing versus a cracklike mode of rupture. *BSSA*, 88, No. 6:1466–1483, 1998.

Aldo Zollo and Maria Lancieri. Real-time estimation of earthquake magnitude for seismic early warning. In P. Gasparini, G. Manfredi, and J. Zschau, editors, *Earthquake early warning systems*, chapter 4, pages 45–83. Springer, 2007.

Aldo Zollo, Maria Lancieri, and Stefan Nielsen. Earthquake magnitude estimation from peak amplitudes of very early seismic signals on strong motion records. *Geophysical Research Letters*, 33, 2006. doi: 10.1029/2006GL027795.

Aldo Zollo, Maria Lancieri, and Stefan Nielsen. Reply to comment by p.reydelek et al on "earthquake magnitude estimation from peak amplitudes of very early seismic signals on strong motion records". *Geophysical Research Letters*, 34(L20303), 2007. doi: 10.1029/2007GL030560.